


---

**COPPER GRAPHITE  
COMPOSITE MATERIALS**  
A NOVEL WAY TO ENGINEER THERMAL  
CONDUCTIVITY AND EXPANSION

The seal of the Free University of Berlin is a circular emblem. It features a central shield with a bear holding a torch. Above the shield is a star. The shield is flanked by two smaller shields, each containing a star. The entire emblem is surrounded by a circular border with the Latin text 'VERITAS LIBERTAS' at the top and 'FREIE UNIVERSITÄT BERLIN' at the bottom, separated by stars.

Im Fachbereich Physik  
der Freien Universität Berlin

eingereichte

**Dissertation**

von

**André Boden**

Berlin, im September 2015

---



**Erstgutachter:** Prof. Dr. Stephanie Reich  
**Zweitgutachter:** Prof. Dr. Eric Anglaret

**Tag der Abgabe:** 01. September 2015

**Tag der Disputation:** 07. Oktober 2015



## *Abstract*

---

The aim of this work is the development of a material with improved thermal conductivity and tailored thermal expansion. Such materials are important for the thermal management of electronic devices. One of the most commonly used materials for thermal management applications is copper, an excellent heat conductor ( $400 \text{ Wm}^{-1}\text{K}^{-1}$ ). Its high thermal expansion ( $17 \text{ ppmK}^{-1}$ ), however, is problematic for thermal management of semiconductor devices. The large thermal expansion mismatch generates thermal stress leading to malfunctions and defects.

Here we demonstrate that by reinforcing copper with graphite platelets the thermal conductivity is improved ( $500 \text{ Wm}^{-1}\text{K}^{-1}$ , 140% of copper) and the thermal expansion is significantly lowered ( $2 \text{ ppmK}^{-1}$ , matching silicon). This is in great parts caused by aligning the anisotropic particles within the copper matrix, which is realized by spark plasma sintering. The influence of the platelet lateral size on the degree of alignment is investigated by polarization-dependent Raman spectroscopy. The ordered orientation of the particles transfers the anisotropic nature graphite to the copper/graphite composite. Thus, the thermal conductivity along the platelet alignment is up to one order of magnitude higher than perpendicular to it. From effective medium approximation the thermal interface resistance ( $10^{-9} \text{ m}^2\text{KW}^{-1}$ ) is extracted. We show that such a thermal resistance is not a limiting factor to obtain increased thermal conductivities in the copper/graphite systems.

The dramatic drop of the thermal expansion perpendicular to the platelet alignment is explained by elasticity theory. We show that the anisotropic structure of graphite in combination with residual thermal stress within the composite is suppressing the thermal expansion of the graphite particles perpendicular to the basal planes. Engineering the strain opens ways to tailor the thermal expansion of metal matrix composites.

The fact that the directions of high thermal conductivity and low thermal expansion in

this copper/graphite composite are perpendicular to each other promises great potential for heat sink application. The technological relevance of our low-expansion material is qualitatively assessed by micro-Raman studies of phonon vibration in silicon attached to copper/graphite composite and traditional heat sink materials. The experiment clearly highlights the excellent thermal expansion compatibility between silicon and our material in sharp contrast to copper or aluminum heat sinks, which induce large thermal stress in silicon. As for superior heat transfer capability, the reduced operating temperature in high power light emitting diodes emphasizes the advantage of directional heat transport in copper/graphite composites and its applicability for thermal management applications.

Taken together, this novel composite material opens ways to increase the performance, mobility and efficiency of thermal management of electronics. Ultimately this will help to improve the reliability and extend the lifetime of electronic devices.

## *Zusammenfassung*

---

Ziel dieser Arbeit ist die Entwicklung eines neuen Materials mit verbesserter thermischer Leitfähigkeit und maßgeschneiderter thermischer Ausdehnung. Derartige Materialien sind wichtig für das Wärmemanagement von elektronischen Geräten. Eines der am häufigsten verwendeten Materialien für Wärmemanagement-Anwendungen ist Kupfer, ein Metall mit herausragenden Wärmeleiteigenschaften ( $400 \text{ Wm}^{-1}\text{K}^{-1}$ ). Jedoch ist die hohe thermische Ausdehnung von Kupfer ( $17 \text{ ppmK}^{-1}$ ) problematisch für das Wärmemanagement von Halbleitern, da sich diese deutlich weniger stark thermisch ausdehnen. Diese große Differenz hat mechanische Verspannungen zur Folge, welche zu Fehlfunktionen und Defekten führen.

Hier zeigen wir, dass die Verstärkung von Kupfer durch Graphit-Plättchen die thermische Leitfähigkeit verbessert ( $500 \text{ Wm}^{-1}\text{K}^{-1}$ , 40% höher als Kupfer) und die thermische Ausdehnung deutlich verringert ( $2 \text{ ppmK}^{-1}$ , übereinstimmend mit Silizium). Die Hauptursache dafür ist die geordnete Ausrichtung der Graphit-Partikel innerhalb der Kupfer-Matrix, was durch Spark Plasma Sintering realisiert wird. Die anisotrope Natur des Graphits wird durch diese Ausrichtung der Partikel auf das Kupfer/Graphit Verbundmaterial übertragen. Auf Grund dessen ist die thermische Leitfähigkeit entlang der Ausrichtung bis zu zehnmal höher als senkrecht zu dieser Richtung. Mit Hilfe der Effective Medium Approximation wurde der thermische Grenzflächenwiderstand ( $10^{-9} \text{ m}^2\text{KW}^{-1}$ ) bestimmt. Wir zeigen, dass ein derartiger thermischer Widerstand keinen negativen Einfluss auf die Verbesserung der thermischen Leitfähigkeit in Kupfer/Graphit Systemen hat.

Der deutliche Abfall der thermischen Ausdehnung senkrecht zur Partikelausrichtung wird mit Hilfe der Elastizitätstheorie erklärt. Die anisotrope Struktur von Graphit zusammen mit mechanischen Verspannungen innerhalb des Verbundmaterials unterdrücken die intrinsische thermische Ausdehnung von Graphit senkrecht zu den Basalebene.

Der gezielte Einsatz von Materialverspannungen innerhalb eines Materials eröffnet neue Möglichkeiten die thermische Ausdehnung von Metallverbundstoffen maßzuschneidern.

Da in diesen Kupfer/Graphit Verbundmaterialien die Richtungen von hoher thermischer Leitfähigkeit und geringer thermischer Ausdehnung senkrecht zueinander stehen, ist die Anwendung dieser Materialien für Wärmemanagement vielversprechend. Die technologische Bedeutung dieses Verbundstoffes wird qualitativ mit Mikro-Raman-Spektroskopie von Gitterschwingungen in Silizium beurteilt, welches mit einem Kühlkörpern aus Kupfer/Graphit Verbundmaterial sowie mit traditionellen Kühlkörpern verbunden ist. Die Untersuchungen zeigen deutlich die hervorragende Kompatibilität der thermischen Ausdehnung zwischen Silizium und dem Verbundmaterial im deutlichen Gegensatz zu Kupfer- und Aluminium-Kühlkörpern. Dank des verbesserten Wärmetransports wird die Betriebstemperatur von Hochleistungsleuchtdioden verringert. Dies unterstreicht den Vorteil eines gerichteten Wärmetransports für die Anwendung im Wärmemanagement von elektronischen Geräten.

Dieses neuartige Verbundmaterial eröffnet neue Möglichkeiten die Leistung, Mobilität und Effizienz des Wärmemanagements von elektronischen Geräten zu verbessern, um die Zuverlässigkeit und die Lebensdauer dieser zu erhöhen.



## *List of Abbreviations and Symbols*

---

<i>a</i>	thermal diffusivity
<i>Al</i>	aluminum
<i>CNTs</i>	carbon nanotubes
<i>c<sub>p</sub></i>	specific heat capacity (constant pressure)
<i>CPU</i>	central processing unit
<i>CTE</i>	coefficient of thermal expansion
<i>Cu</i>	copper
<i>EMA</i>	effective medium approximation
<i>GmP</i>	graphite microplatelet
<i>GnP</i>	graphite nanoplatelet
<i>Gr</i>	graphite
<i>HOPG</i>	highly oriented pyrolytic graphite
<i>k</i>	thermal conductivity
<i>LED</i>	light emitting diode
<i>MMC</i>	metal matrix composite
<i>ρ</i>	mass density
<i>R<sub>k</sub></i>	Kapitza resistance
<i>ROM</i>	rule of mixture

<i>SEM</i>	scanning electron spectroscopy
<i>Si</i>	silicon
<i>SPS</i>	spark plasma sintering
<i>SuCoLEx</i>	Superior Conductivity Low Expansion - name for copper/G300 composite with 50 vol% graphite concentration
<i>TCE</i>	thermal conductivity enhancement
<i>TIM</i>	thermal interface material

---

## *Table of Contents*

---

<b>Chapter 1</b>	
<b>Introduction</b>	<b>1</b>
References .....	5
<b>Chapter 2</b>	
<b>Theoretical Background</b>	<b>7</b>
<b>2.1 About heat conduction</b> .....	<b>8</b>
2.1.1 Heat conduction by electrons .....	8
2.1.2 Heat conduction in carbon .....	10
<b>2.2 Modulation of thermal conductivity in composite materials</b> .....	<b>12</b>
<b>2.3 Measurement of thermal diffusivity and conductivity</b> .....	<b>14</b>
2.3.1 Flash method .....	15
<b>2.4 Thermal expansion in solid materials</b> .....	<b>20</b>
2.4.1 Thermal expansion of carbon materials .....	23
2.4.2 Thermal expansion of composite materials .....	24
<b>2.5 Raman scattering</b> .....	<b>26</b>
2.5.1 Raman spectroscopy of graphite .....	26
2.5.2 Selection rules for the G line .....	27
2.5.3 Phonons under strain in silicon .....	30

---

References .....	32
<b>Chapter 3</b>	
<b>Materials and Methods</b>	<b>37</b>
3.1 Components of the composite materials.....	37
3.2 Composite fabrication .....	38
3.3 Thermal diffusivity measurements.....	40
3.4 Thermal expansion measurements .....	42
3.5 Structural characterization .....	43
3.6 Raman spectroscopy.....	43
3.7 LED heat sink setup and thermographic images.....	44
References .....	45
<b>Chapter 4</b>	
<b>Results and Discussion</b>	<b>47</b>
4.1 Structure and morphology.....	48
4.1.1 Copper powder and graphite platelets .....	48
4.1.2 Consolidated materials.....	49
4.2 Quantification of graphite alignment.....	52
4.3 Thermal transport in copper/graphite composites .....	56
4.3.1 Composites containing graphite nanoplatelets.....	58
4.3.2 Composites containing graphite microplatelets.....	59
4.3.3 Effective medium approximation for copper/graphite composites ...	60
4.4 Thermal expansion of copper/graphite composites.....	67
4.4.1 Elasticity theory for CTE of graphite under strain.....	71
4.4.2 Theoretic predictions for the thermal expansion .....	74
4.5 Strain induced in silicon in different heat sink assemblies.....	75
4.5.1 Free standing silicon .....	75
4.5.2 Silicon attached to aluminum, copper, and SuCoLEx.....	76

---

<b>4.6 SuCoLEx as heat sink for high power LEDs .....</b>	<b>79</b>
<b>References .....</b>	<b>81</b>
<b>Chapter 5</b>	
<b>Summary and Outlook</b>	<b>83</b>



*I'm an experimental physicist. You know, one of those guys who examines the building blocks of creation and says, "Hello maker of the universe. I see what you did there. Good one!"*

Leonard Hofstadter, The Big Bang Theory







*to Klara and Erich...*





Metals like copper (Cu) and aluminum (Al) are the most common heat sink materials. To maximize the surface area of the heat sink that is in contact to the flowing air fins are often incorporated in its design. The typical size of a CPU is around  $2 \text{ cm}^2$ . For high power computation the required heat flux might be too high for the thermal management packaging. Incorporating a heat spreader between the heat sink and the CPU increases the size of the cooled area and reduces the required heat flux, as indicated in Figure 1.1. However, this also introduces additional interfaces, which increase the thermal resistance of the thermal management packaging.

A general problem in thermal management is that metals like Cu or Al cannot be in direct contact with a computer chip that is made of silicon (Si). The huge difference in thermal expansion creates high thermal stresses at the Si/metal interface, which may eventually lead to malfunction and permanent damage to the CPU [5]. As a consequence thermal interface materials (TIM), usually a grease or paste containing epoxy or silicone matrix with thermally conductive fillers, are required to protect the Si chip from thermal stress caused by the much higher thermal expansion of the metal. The second important function of a TIM is to improve the thermal contact between adjacent surfaces by closing air voids and gaps. The thermal conductivity, however, is usually one or two orders of magnitude lower compared to metals. The ideal configuration for chip cooling would be a heat sink material with high thermal conductivity, preferably exceeding Cu, and a thermal expansion similar to Si. In this case the heat sink might be soldered directly on the chip to avoid additional thermal interfaces, usually the bottleneck for the heat transport capabilities of the thermal management packaging.

Over the last years the increased heat generation became a difficult to overcome barrier in the development of improved integrated circuits [6]. Figure 1.2 shows the development of heat flux in computer chips. With the beginning of the 1980's the heat flux increased dramatically which posed new challenges for the thermal management of electronic devices. To improve the cooling performance one mainly has to overcome the limitations in heat transfer capability of the heat sink material and to improve the design of the thermal packaging. The demand for highly mobile, small, and lightweight electronic devices calls for small heat sinks with low densities.

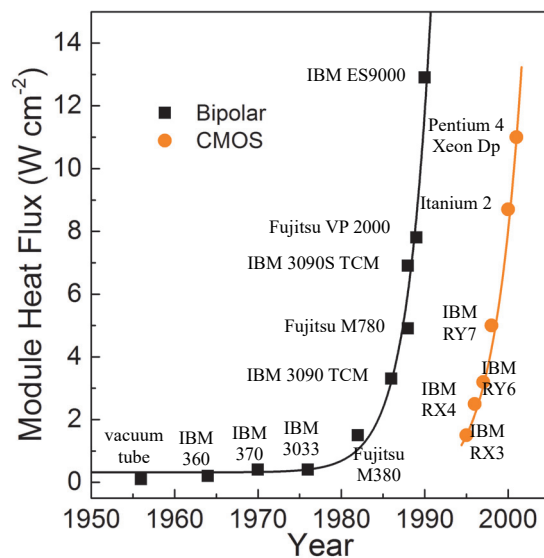


**Figure 1.2** Evolution of heat flux in high-end computers. Data taken from Reference [7] and [8].

In recent years research focused on the development of novel composite materials that combine the physical properties of their components. Prime candidate to meet the increased demand of thermal performance of heat sink materials are metal matrix composites (MMC) where metals are combined with nano- and micro-sized fillers. Due to their excellent thermophysical properties and low volumetric mass density carbon materials are expected to take over the role of the filling material in such MMCs [9]. The combination of extraordinary high thermal conductivity and ultra low thermal expansion of graphite (nano)platelets [10,11], graphene [12-14], carbon nanotubes [15-17], and nanodiamonds [18,19] is unrivaled. These carbon materials have proven to enhance the thermal properties in polymer matrix composites [20-24]. For filling materials with anisotropic thermal properties, e.g., graphite, graphene, and carbon nanotubes, filler alignment is crucial for an effective enhancement of the thermal properties [21,25].

Compared to polymer matrix composites the incorporation of carbon fillers into a metal matrix is more challenging, due to the large density mismatch that leads to poor dispersibility. Early studies of metal/carbon composites showed that random filler alignment and filler agglomeration reduce the thermal conductivity of the composite compared to the pure metal [25-28]. The different mechanisms of heat conduction (via electrons in metals and via phonons in carbon) result in a thermal resistance at the interface of the composite components that decreases the thermal conductivity of the MMC. To use MMCs as heat sink materials they need to be fabricated in bulk quantities. Several approaches to synthesize metal/carbon composites, however, create MMC films [29-31]. Recent studies successfully managed to fabricate bulk quantities of MMC with anisotropic thermal properties, where the thermal conductivity was not reduced by adding carbon fillers [32-34]. However, the combination of increased thermal conductivity (i.e., beyond the value of Cu) and tailoring the thermal expansion to match the value of Si remains challenging. Crucial for a heat sink material is that the direction with maximum thermal conductivity is perpendicular to the direction of low thermal expansion.

In this thesis the fabrication of a novel MMC is introduced where a copper matrix is reinforced with graphite platelets. The advantage of graphite platelets over graphene or carbon nanotubes is that they are inexpensive, easy to process, and commercially available in large quantities and morphologies. It will be shown that for the suitable filler size and concentration this copper/graphite composite poses significantly improved thermal transport properties in combination with silicon-like thermal expansion perpendicular to the direction of high thermal conductivity, as desired for a heat sink material. This combination was achieved by aligning the graphite particles within the copper matrix by spark plasma sintering, a technique that creates bulk quantities and can be scaled up to an industrial scale. Within the copper matrix the graphite particles are subjected to thermal strain. It will be shown that this strain is reversing the thermal expansion behavior of graphite perpendicular to its layers from strongly expanding to strong contracting. This contraction entails the silicon-like expansion of the copper/graphite composite.

Besides the detailed analysis of the structure and the thermophysical properties of the composites this novel material is tested as a heat sink material. In two different assemblies it will be demonstrated that the copper/graphite composite significantly reduces thermal stress in silicon and outperforms the cooling capabilities of pure copper. This composite material has the potential to form a heat sink that is directly attached to a computer chip. Thus, the number of interfaces is reduced to a minimum and the cooling performance is maximized.

## References

- [1] Bardeen J, Brattain WH. The Transistor, A Semi-Conductor Triode. *Physical Review* 1948, **74**(2): 230-231.
- [2] Kilby JS. Miniaturized electronic circuits. US Patent US3138743 A; 1964.
- [3] Moore GE. Cramming more components onto integrated circuits. *Electronics*, 38 (8): 114-117. 1965.
- [4] International Technology Roadmap for Semiconductors. 2013 Edition. [www.itrs.net](http://www.itrs.net)
- [5] Lasance CJM. Advances In High-Performance Cooling For Electronics. *Electronics Cooling Magazine*; 2005.
- [6] Stevens M. The Implications of Moore's Law for Computing. *Future Led*; 2015.
- [7] Chu RC, Simons RE, Ellsworth MJ, Schmidt RR, Cozzolino V. Review of cooling technologies for computer products. *Device and Materials Reliability, IEEE Transactions on* 2004, **4**(4): 568-585.
- [8] Ellsworth MJ. High Powered Chip Cooling — Air and Beyond. *Electronics Cooling* August 2005.
- [9] Balandin AA. Thermal properties of graphene and nanostructured carbon materials. *Nature materials* 2011, **10**(8): 569-581.
- [10] Klemens PG, Pedraza DF. Thermal conductivity of graphite in the basal plane. *Carbon* 1994, **32**(4): 735-741.
- [11] Nelson JB, Riley DP. The thermal expansion of graphite from 15°C. to 800°C.: part I. Experimental. *Proc Phys Soc* 1945, **57**(6).
- [12] Balandin AA, Ghosh S, Bao W, Calizo I, Teweldebrhan D, Miao F, *et al.* Superior Thermal Conductivity of Single-Layer Graphene. *Nano Letters* 2008, **8**(3): 902-907.
- [13] Ghosh S, Calizo I, Teweldebrhan D, Pokatilov EP, Nika DL, Balandin AA, *et al.* Extremely high thermal conductivity of graphene: Prospects for thermal management applications in nanoelectronic circuits. *Applied Physics Letters* 2008, **92**(15).
- [14] Yoon D, Son Y-W, Cheong H. Negative Thermal Expansion Coefficient of Graphene Measured by Raman Spectroscopy. *Nano Letters* 2011, **11**(8): 3227-3231.
- [15] Berber S, Kwon Y-K, Tománek D. Unusually High Thermal Conductivity of Carbon Nanotubes. *Physical Review Letters* 2000, **84**(20): 4613-4616.
- [16] Cao J, Yan X, Xiao Y, Ding J. Thermal conductivity of zigzag single-walled carbon nanotubes: Role of the umklapp process. *Physical Review B* 2004, **69**(7).
- [17] Yosida Y. High-temperature shrinkage of single-walled carbon nanotube bundles up to 1600 K. *Journal of Applied Physics* 2000, **87**(7): 3338-3341.
- [18] Olson JR, Pohl RO, Vandersande JW, Zoltan A, Anthony TR, Banholzer WF. Thermal conductivity of diamond between 170 and 1200 K and the isotope effect. *Physical Review B* 1993, **47**(22): 14850-14856.
- [19] Krishnan RS. Thermal Expansion of Diamond. *Nature* 1944, **154**: 486-487.
- [20] Gharagozloo-Hubmann K, Boden A, Czempiel GJF, Firkowska I, Reich S. Filler geometry and interface resistance of carbon nanofibres: Key parameters in thermally conductive polymer composites. *Applied Physics Letters* 2013, **102**(21).
- [21] Marconnet AM, Yamamoto N, Panzer MA, Wardle BL, Goodson KE. Thermal Conduction in Aligned Carbon Nanotube–Polymer Nanocomposites with High Packing Density. *ACS Nano* 2011, **5**(6): 4818-4825.
- [22] Yu A, Ramesh P, Itkis ME, Bekyarova E, Haddon RC. Graphite Nanoplatelet-Epoxy Composite Thermal Interface Materials. *Journal of Physical Chemistry C* 2007, **111**(21): 7565-7569.
- [23] Shahil KMF, Balandin AA. Graphene–Multilayer Graphene Nanocomposites as

- Highly Efficient Thermal Interface Materials. *Nano Letters* 2012, **12**(2): 861-867.
- [24] Tian X, Itkis ME, Bekyarova EB, Haddon RC. Anisotropic Thermal and Electrical Properties of Thin Thermal Interface Layers of Graphite Nanoplatelet-Based Composites. *Sci Rep* 2013, **3**.
- [25] Khaleghi E, Torikachvili M, Meyers MA, Olevsky EA. Magnetic enhancement of thermal conductivity in copper–carbon nanotube composites produced by electroless plating, freeze drying, and spark plasma sintering. *Materials Letters* 2012, **79**: 256-258.
- [26] Nie J-h, Jia C-c, Jia X, Li Y, Zhang Y-f, Liang X-b. Fabrication and thermal conductivity of copper matrix composites reinforced by tungsten-coated carbon nanotubes. *Int J Miner Metall Mater* 2012, **19**(5): 446-452.
- [27] Boden A. Thermal properties of Carbon Nanotube Reinforced Metal Composites. *Diploma Thesis FU Berlin*, Berlin 2010 (unpublished)
- [28] Firkowska I, Boden A, Vogt A-M, Reich S. Effect of carbon nanotube surface modification on thermal properties of copper–CNT composites. *Journal of Materials Chemistry* 2011, **21**(43).
- [29] Goli P, Ning H, Li X, Lu CY, Novoselov KS, Balandin AA. Thermal Properties of Graphene–Copper–Graphene Heterogeneous Films. *Nano Letters* 2014, **14**(3): 1497-1503.
- [30] Amini S, Garay J, Liu G, Balandin AA, Abbaschian R. Growth of large-area graphene films from metal-carbon melts. *Journal of Applied Physics* 2010, **108**(9): 094321.
- [31] Jagannadham K. Thermal Conductivity of Copper-Graphene Composite Films Synthesized by Electrochemical Deposition with Exfoliated Graphene Platelets. *Metallurgical and Materials Transactions B* 2011, **43**(2): 316-324.
- [32] Subramaniam C, Yasuda Y, Takeya S, Ata S, Nishizawa A, Futaba D, *et al.* Carbon nanotube-copper exhibiting metal-like thermal conductivity and silicon-like thermal expansion for efficient cooling of electronics. *Nanoscale* 2014, **6**(5): 2669-2674.
- [33] Zhang C, He X, Liu Q, Ren S, Qu X. Fabrication and thermo-physical properties of graphite flake/copper composites. *Journal of Composite Materials* 2014.
- [34] Chen JK, Huang IS. Thermal properties of aluminum–graphite composites by powder metallurgy. *Composites Part B: Engineering* 2013, **44**(1): 698-703.





## 2.1 About heat conduction

Thermal energy is transferred by radiation, convection (liquids and gases), and conduction (solids). The ability to conduct heat strongly depends on the composition of a material. It is considered as a transfer of internal energy caused by a temperature gradient. According to the second law of thermodynamics the heat flows in the direction of lower temperature. Described by Fourier's Law [1] in its differential form the local heat flux density  $\dot{q}$  is proportional to the negative temperature gradient  $\nabla T$  in the system with

$$\dot{q} = -k \cdot \nabla T, \quad (\text{Eq. 2.1})$$

where  $k$  is the thermal conductivity of the material. Using Fourier's Law, conservation of energy and the relation  $\Delta Q = c_p \rho \Delta T$ , where  $c_p$  is the specific heat and  $\rho$  is the mass density of the material, one derives the heat equation. It describes the correlation between the temporal change and the spacial variation of the temperature at a certain location in a solid body [2]

$$c_p \rho \frac{\partial T}{\partial t} - k \nabla^2 T = 0, \quad (\text{Eq. 2.2})$$

which is rewritten as

$$\frac{\partial T}{\partial t} = a \nabla^2 T, \quad \text{with } a = \frac{k}{c_p \rho}. \quad (\text{Eq. 2.3})$$

$a$  is the thermal diffusivity. As seen from Equation 2.3 the thermal diffusivity is the ratio of the thermal conductivity  $k$  to the volumetric heat capacity  $c_p \rho$  of a material and, therefore, characterizes the ability of a material to transfer heat relative to the ability to store it. All of these physical quantities are temperature dependent and specific for a given material. The mechanism of heat conduction strongly depends on the electronic as well as crystallographic structure of the material. As a consequence the thermal conductivity of a material may depend on the direction of the heat flow.

### 2.1.1 Heat conduction by electrons

In metals the atomic cores are surrounded by quasi-free electrons. These electrons are not only carrying electrical current but also transfer heat by colliding with atoms and other electrons. The fundamental expression of the electronic contribution to the thermal conductivity  $k_{\text{el}}$  is [3]

$$k_{el} = \frac{1}{3} n c_{el} v_{el} l_{el}, \quad (\text{Eq. 2.4})$$

where  $n$  is the number of conduction electrons per volume,  $c_{el}$  is the electronic heat capacity per electron,  $v_{el}$  is the electron velocity and  $l_{el}$  is the electron mean free path. With the assumption of quasi-free electrons the electron velocity equals the Fermi velocity  $v_F$  and  $c_{el} = (\pi k_B / v_F)^2 (T/m)$ . Following Equation 2.4  $k_{el}$  is rewritten to

$$k_{el} = \frac{\pi^2 n k_B^2 T \tau}{3m}, \quad (\text{Eq. 2.5})$$

where  $\tau = l_{el} / v_{el}$  is the electron lifetime. The relation between Equation 2.5 and the electrical conductivity  $\sigma_{el} = ne^2 \tau / m$  leads to the Wiedemann-Franz-Law [4]

$$\frac{k_{el}}{\sigma_{el}} = LT \quad \text{with} \quad L = \frac{k_{el}}{\sigma_{el} T} = \frac{\pi^2}{3} \left( \frac{k_B}{e} \right)^2 = 2.44 \times 10^{-8} \text{ W}\Omega\text{K}^{-2}, \quad (\text{Eq. 2.6})$$

where the lifetime of electrical and thermal transport is assumed to be the same.  $L$  is the so-called Lorenz number. Compared to heat transport via lattice vibrations (or phonons) electrons dominate thermal conduction in metals. Thus, metals like silver ( $429 \text{ Wm}^{-1}\text{K}^{-1}$ ), copper ( $401 \text{ Wm}^{-1}\text{K}^{-1}$ ), and aluminum ( $237 \text{ Wm}^{-1}\text{K}^{-1}$ ) are among the best known heat conductors [5]. This is in line with the electrical conductivity, which is highest for silver ( $6.21 \times 10^7 \text{ Sm}^{-1}$ ), followed by copper ( $5.88 \times 10^7 \text{ Sm}^{-1}$ ) and aluminum ( $3.65 \times 10^7 \text{ Sm}^{-1}$ ) [3]. Following Equation 2.6 the Lorenz numbers are 2.30, 2.27, and 2.18 for silver, copper, and aluminum. Quite remarkably this is in good agreement with the theoretical value of the Lorenz number given the fact that Equation 2.6 is independent of the mass and density of the particles. Moreover, this underlines the electronic nature of thermal transport in metals.

It is worth mentioning that the thermal conductivity is given for pure, highly crystalline materials. Depending on the thermomechanical treatment during the fabrication process the thermal conductivity may be lower [6]. In the presence of impurities, such as oxygen or other metal atoms, the thermal conductivity is lowered even further. This is especially true for alloys. The thermal conductivity of common copper alloys with copper content above 99% lies in the range from 200 to  $380 \text{ Wm}^{-1}\text{K}^{-1}$  [6]. Due to the combination of high thermal conductivity with excellent processing and low material costs, copper and aluminum are widely used as heat transferring materials in many applications.

## 2.1.2 Heat conduction in carbon

Carbon exists in many different natural and synthetic allotropic forms such as amorphous carbon, graphite, diamond, graphene, and carbon nanotubes [7]. Graphite consists of  $sp^2$ -hybridized carbon atoms bound in parallel planes (basal planes,  $a$ - $b$  axis) with hexagonal structure, as presented in Figure 2.1. Within the planes the carbon atoms are strongly bound via covalent bonds. The interlayer connection ( $c$  axis), however, is weak due to weak van der Waals forces. Moreover, the interlayer spacing is about three times larger than the in-plane C-C distance. Due to its layered structure graphite is a highly anisotropic material, when it comes to mechanical, electrical, and thermal properties. As a result of the  $sp^2$ -hybridization the fourth valence electron is located in the delocalized  $\pi$ -orbital leading to a metal-like electrical conduction. Perpendicular to the basal planes the electrical conductivity of graphite is three orders of magnitude lower [8].

According to the Wiedemann-Franz-Law (Equation 2.6) the electronic contribution to the thermal conductivity parallel to the basal is estimated to  $k_{e1} \approx 2 \text{ Wm}^{-1}\text{K}^{-1}$  (using  $\sigma_{e1}$  from Reference [8]). The contribution of the lattice vibration (or phonons) to the thermal conductivity  $k_{ph}$  is given by [3]

$$k_{ph} = \frac{1}{3} c_{ph} v_{ph} l_{ph}, \quad (\text{Eq. 2.7})$$

where  $c_{ph}$  is the heat capacity of the phonons,  $v_{ph}$  the phonon velocity and  $l_{ph}$  the phonon mean free path. Because of the high phonon velocity and mean free path in graphite the thermal conductivity of graphite is dominated by lattice vibrations. Klemens and Pedraza calculated  $k_{ph} = 1910 \text{ Wm}^{-1}\text{K}^{-1}$  [9]. Due to the strong binding of the carbon atoms along the basal planes the phonons propagate much faster than perpendicular to the planes, where the binding is weak and the lattice spacing is much larger [9,10]. Consequently, the thermal conductivity along the  $c$  axis is much lower.

With natural graphite existing in many different forms the thermal conductivity of these materials covers a wide range. Highly oriented pyrolytic graphite (HOPG) is an artificial graphite material, which exhibits the highest degree of preferred crystallographic orientation of the  $c$  axis. Therefore, the thermal conductivity of HOPG along and perpendicular to the basal planes approaches the values for ideal graphite single crystals [11]. Typical

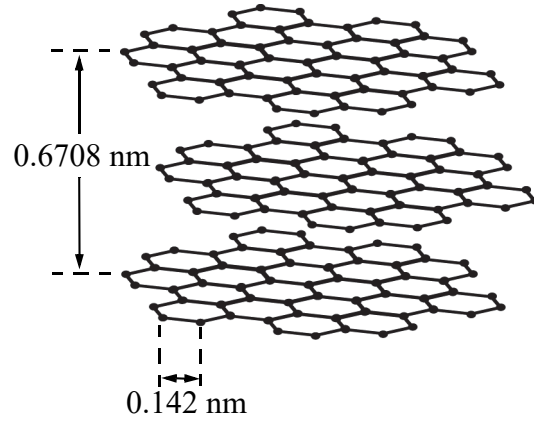


**Figure 2.1** Schematic structure of graphite with hexagonal unit cell (ABABAB stacking).

values for the thermal conductivity along the basal planes of HOPG are close to  $1900 \text{ Wm}^{-1}\text{K}^{-1}$ , which is more than four times higher than the best metals [5]. Perpendicular to the planes the thermal conductivity is three orders of magnitude lower and lies around  $5$  to  $15 \text{ Wm}^{-1}\text{K}^{-1}$  [5], directly reflecting the structural anisotropy. For all types of natural graphite the thermal conductivity lies between these two extreme values due to various factors such as defects, impurities, size and orientation of the grains, degree of graphitization, and so forth. At room temperature the phonon mean free path along the basal plane is on the order of  $1 \mu\text{m}$  [9]. Thus, the thermal conductivity at room temperature is reduced for a grain size below  $2 \mu\text{m}$ .

Among all naturally occurring materials natural diamond is the material with the highest thermal conductivity of  $2190 \text{ Wm}^{-1}\text{K}^{-1}$  at room temperature [12]. This high value is a direct result of the strong  $sp^3$ -hybridized covalent bonds and the high mean free path of the lattice vibrations. Synthetic diamond with low isotropic impurities is an even better heat conductor exhibiting a thermal conductivity of  $3320 \text{ Wm}^{-1}\text{K}^{-1}$  at room temperature, due to the reduction of phonon-isotropic scattering. [13]

This high conductivity is only matched by the two nanostructured carbon allotropes graphene and carbon nanotubes (CNTs) with thermal conductivities exceeding the bulk graphite limit. Graphene is a one atom thick single layer of graphite where the carbon atoms are strongly bound in a  $sp^2$ -hybridized hexagonal lattice and is considered to be a two dimensional system. Experimental studies revealed that the thermal conductivity of graphene along the plane exceeds  $3000 \text{ Wm}^{-1}\text{K}^{-1}$  at room temperature [14,15]. Increasing the number of layers (few-layer graphene) decreases the thermal conductivity and eventually approaches the value for bulk graphite [16]. With carbon nanotubes being single or multi layer of graphene rolled up at a specific angle the thermal conduction process is similar to graphene. The typical diameter of a single-walled carbon nanotube is in the order of  $1 \text{ nm}$  while the length may be up to six orders of magnitude higher. Therefore, CNTs are considered to be a one dimensional system. At room temperature the thermal conductivity of a single-walled CNT was found to be  $\sim 3500 \text{ Wm}^{-1}\text{K}^{-1}$  [17]. Due to wall-to-wall interactions the thermal conductivity of multi-walled CNTs lies below single-walled tubes. Still, the thermal conductivity exceeds a value of  $3000 \text{ Wm}^{-1}\text{K}^{-1}$  [18]. Amorphous carbon does not have a long-ranged crystalline structure and, therefore, is a bad heat conductor.

Given these extraordinary high thermal conductivities, graphite, diamond, graphene, and carbon nanotubes have great potential to enhance the thermal conductivity of conventional materials by forming carbon reinforced composites [19].

## 2.2 Modulation of thermal conductivity in composite materials

If a material is composed of components with different thermal conductivities and heat conduction mechanisms the thermal conductivity of the composite is generally unknown. For many applications, however, the knowledge of the thermal transport behavior is crucial. Besides the thermal conductivity of the composite components the resulting thermal conductivity depends on various factors, such as geometry and orientation of the reinforcement as well as thermal interface resistance. By utilizing the rule of mixture the thermal conductivity of such composite materials is over- or underestimated, since important factors concerning the heat transport are neglected. This is particularly significant when highly anisotropic materials are used. A widely used model for the calculation of the thermal conductivity enhancement (TCE) in two component composite materials was developed by Nan *et al.* [20] in the framework of effective medium approximation (EMA). As described by Nan [21] one expresses the thermal conductivity  $k(r)$  of a composite material by

$$k(r) = k^0 + k'(r) \quad (\text{Eq. 2.8})$$

where  $k^0$  is the constant part of the homogeneous matrix and  $k'(r)$  is the perturbation term, which contains all variations in  $k(r)$  caused by the reinforcing component. The expression for the effective thermal conductivity  $k$  of the composite independent of the position is obtained using the Green's function  $G$  for the homogeneous material defined by  $k^0$  and the transition matrix  $T$  that contains the structural parameters of the composite as follows [21]

$$k = k^0 + \langle T \rangle (I + \langle GT \rangle)^{-1}, \quad (\text{Eq. 2.9})$$

where  $I$  is the unit tensor with the brackets denoting spacial averaging. The matrix  $T$  is given by

$$T = \sum_n T_n + \sum_{n, m \neq n} T_n G T_m + \dots \cong \sum_n T_n = \sum_n k'_n (I - G k'_n)^{-1}, \quad (\text{Eq. 2.10})$$

where the first term is the sum of the  $T$  matrices of  $n$  particles and the successive terms account for the interactions between the different particles. If one neglects particle interactions the matrix  $T$  is simplified as shown in Equation 2.10. This approximation is only valid if the inclusions are homogeneously dispersed in and surrounded by the matrix, i.e., the volume fraction of the particles is sufficiently low ( $f < 0.4$ ) [22]. However, it has been

shown that this EMA remains valid for higher volume fractions, if the thermal conductivity of the matrix and the inclusion particles are within a factor of 100 or less [20]. Therefore, the model suits well for metal matrix composite containing carbon reinforcement. Considering now an ellipsoidal particle with a surrounding interface layer, the equivalent thermal conductivities along the symmetric axes of the ellipsoidal composite unit cell are derived from Equation 2.9 as follows [20]

$$k_{ii}^c = \frac{k_{ii}^p}{(1 + \gamma L_{ii} k_{ii}^p / k_m)}, \text{ with } \gamma = \begin{cases} (2 + 1/p)\kappa, & \text{for } p \geq 1 \\ (1 + 2p)\kappa, & \text{for } p \leq 1 \end{cases}, \quad (\text{Eq. 2.11})$$

where the parameter  $\kappa$  is defined by

$$\kappa = \begin{cases} R_k k_m / a_1, & \text{for } p \geq 1 \\ R_k k_m / a_3, & \text{for } p \leq 1 \end{cases}, \quad (\text{Eq. 2.12})$$

with  $R_k$  being the Kapitza resistance (i.e., interface resistance between matrix and inclusion) and  $k_m$  and  $k_{ii}^p$  being the thermal conductivity of the matrix and the ellipsoidal particle along the symmetric axes of the particle. The aspect ratio  $p = a_3 / a_1$  is  $< 1$  for oblate ( $a_1 = a_2 > a_3$ ) and  $> 1$  for prolate ( $a_1 = a_2 < a_3$ ) ellipsoids, where  $a_1$ ,  $a_2$ , and  $a_3$  are the radii of the ellipsoid. The geometrical factors  $L_{ii}$  (depolarization factors) depend on the shape of the particle. They are given by [23,24]

$$L_{11} = L_{22} = \begin{cases} \frac{p^2}{2(p^2 - 1)} - \frac{p}{2(p^2 - 1)^{3/2}} \cosh^{-1} p, & \text{for } p > 1 \\ \frac{p^2}{2(p^2 - 1)} + \frac{p}{2(1 - p^2)^{3/2}} \cos^{-1} p, & \text{for } p < 1 \end{cases} \quad (\text{Eq. 2.13})$$

$$L_{33} = 1 - 2L_{11}.$$

For a two phase composite with equal-sized ellipsoidal particles and interface resistance between the matrix and the particles one obtains the effective thermal conductivity of the composite from Equation 2.9 by choosing  $k_0 = k_m$  for the three material axes as follows [20]

$$k_{11} = k_{22} = k_m \frac{2 + f[\beta_{11}(1 - L_{11})(1 + \langle \cos^2 \theta \rangle) + \beta_{33}(1 - L_{33})(1 - \langle \cos^2 \theta \rangle)]}{2 - f[\beta_{11}L_{11}(1 + \langle \cos^2 \theta \rangle) + \beta_{33}L_{33}(1 - \langle \cos^2 \theta \rangle)]} \quad (\text{Eq. 2.14})$$

and

$$k_{33} = k_m \frac{1 + f[\beta_{11}(1 - L_{11})(1 - \langle \cos^2 \theta \rangle) + \beta_{33}(1 - L_{33})(\langle \cos^2 \theta \rangle)]}{1 - f[\beta_{11}L_{11}(1 - \langle \cos^2 \theta \rangle) + \beta_{33}L_{33}(\langle \cos^2 \theta \rangle)]}, \quad (\text{Eq. 2.15})$$

with

$$\beta_{ii} = \frac{k_{ii}^c - k_m}{k_m + L_{ii}(k_{ii}^c - k_m)}, \quad (\text{Eq. 2.16})$$

where  $f$  is the volume fraction of the inclusion particles. The average  $\langle \cos^2 \theta \rangle$  describes the orientation of the ellipsoidal particles within the matrix and is given by

$$\langle \cos^2 \theta \rangle = \frac{\int \rho(\theta) \cos^2 \theta \sin \theta d\theta}{\int \rho(\theta) \sin \theta d\theta}, \quad (\text{Eq. 2.17})$$

where  $\theta$  is the angle between the materials axis in  $k_{33}$  direction and the corresponding local particle symmetric axis and  $\rho(\theta)$  is a distribution function representing the particle orientation. For a random dispersion of the ellipsoidal particles  $\langle \cos^2 \theta \rangle = 1/3$ , whereas  $\langle \cos^2 \theta \rangle = 1$  for fully aligned inclusions. Using the Equations 2.14 and 2.15 the thermal conductivity is calculated for a two phase composite material containing inclusion particles with various shapes such as fibers, plates, or spheres [20]. For many systems these equations can be simplified (e.g., for very large or small aspect ratios, random or full alignment). Furthermore, using the described EMA one is able to predict parameters of composite materials which are difficult to access experimentally such as the thermal interface resistance or structural parameters [22].

### 2.3 Measurement of thermal diffusivity and conductivity

The determination of the thermal transport properties is realized by numerous approaches for measuring the heat flux and the temperature gradient based on Equation 2.1. This is done in steady state conditions, i.e., the temperature of the measured material does not change anymore. The heat flux is measured directly by, e.g., measuring the power of the used heating source or indirectly by comparison to a reference material. In both cases the experimental setup and the materials have to be well engineered. Depending on the thermal conductivity of the involved materials as well as the experimental setup reaching steady state conditions usually takes 30 minutes or more. Therefore, a good thermal insulation of the system is essential. One of the oldest steady state methods and a standard method today is the guarded hot plate method (ASTM C 177) developed in the beginning of the 20th century [25].

In recent decades several transient methods (non-steady state) to measure the thermal



transport properties have been developed. The main difference to steady state techniques is that the measurement is performed during the process of heating up or cooling down, which means that the measurement time is much shorter, typically a few seconds or less. Commonly used methods are the  $3\omega$  method [26], the hot wire method [27], the hot strip [28] and hot disk method [29], and the flash method [30]. In this study the flash method will be used to determine the thermal diffusivity and thermal conductivity of the materials. It will be described in detail in the following section.

### 2.3.1 Flash method

The flash method was first described by Parker *et al.* [30] in 1961; it is probably the most commonly used method for thermal transport investigations on bulk solid materials (ASTM E 1461). In this technique an usually disc shaped specimen is exposed to a short and intense light pulse on one side, while the temperature rise is recorded with an infrared detector on the other side, as schematically shown in Figure 2.2a. The typical temperature profile outlined in Figure 2.2b may be separated in three sections. Section I corresponds to a period of constant temperature prior to the light flash at  $t = 0$ , section II corresponds to the transient temperature rise period caused by the light flash, and section III to the cooling period after the temperature of the rear surface reached a maximum. The two main advantages of the flash method over many steady state techniques are the elimination of the problem of thermal contact resistance as well as the minimization of heat losses, by using a light flash as the heat source in combination with a short measurement time [30]. In order to obtain the thermal diffusivity  $a$  from the temperature profile one has to derive an analytical expression for the time-dependent temperature of the rear surface the solid.

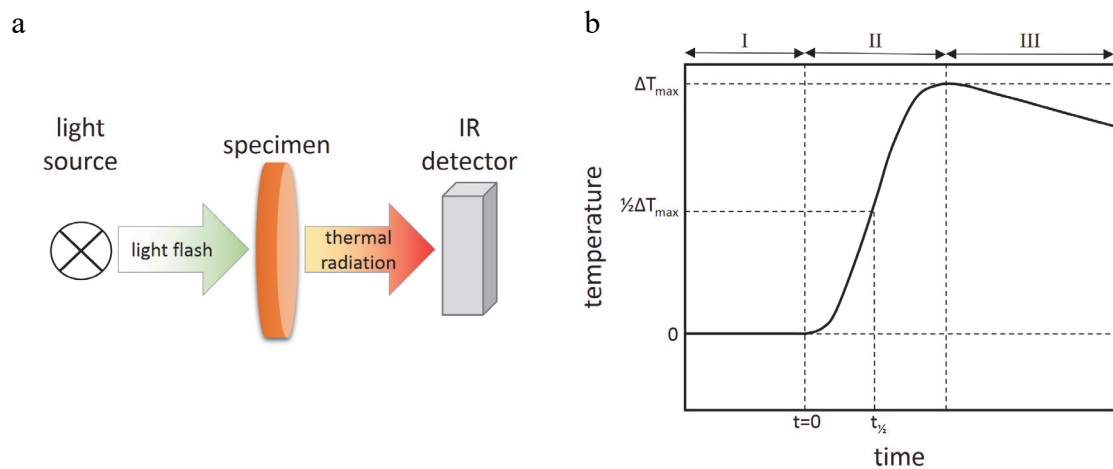


**Figure 2.2 (a)** Schematic setup of the flash method. **(b)** Temperature profile recorded by the IR detector. Prior to the light flash at  $t = 0$  the temperature is constant (I), after the flash the temperature is rising to a maximum (II), and eventually decreasing due to heat losses (III).

This is done by using the temperature distribution given by Carslaw and Jaeger [2] as

$$T(x, t) = \frac{1}{L} \int_0^L T(x, 0) dx + \frac{2}{L} \sum_{n=1}^{\infty} \exp\left(-\frac{n^2 \pi^2 a t}{L^2}\right) \times \cos\left(\frac{n \pi x}{L}\right) \int_0^L T(x, 0) \cos\left(\frac{n \pi x}{L}\right) dx, \quad (\text{Eq. 2.18})$$

where  $L$  is the thickness of the solid and  $a$  is the thermal diffusivity. By irradiating the front surface at  $x = 0$  with a short light pulse the energy flux  $q$  is absorbed within a small depth  $g$ . The temperature distribution is then given by [30]

$$\begin{aligned} T(x, 0) &= \frac{q}{\rho c_p g} \quad \text{for } 0 < x < g \\ \text{and} \\ T(x, 0) &= 0 \quad \text{for } g < x < L, \end{aligned} \quad (\text{Eq. 2.19})$$

where  $\rho$  is the density and  $c_p$  is the specific heat of the solid. With that Equation 2.18 is rewritten as [30]

$$T(x, t) = \frac{q}{\rho c_p L} \left[ 1 + 2 \sum_{n=1}^{\infty} \cos\left(\frac{n \pi x}{L}\right) \frac{\sin((n \pi g)/L)}{(n \pi g)/L} \times \exp\left(-\frac{n^2 \pi^2 a t}{L^2}\right) \right]. \quad (\text{Eq. 2.20})$$

For opaque materials  $g$  is a very small number and, therefore, Equation 2.20 is simplified to obtain the time dependent temperature development at the rear surface at  $x = L$  as follows [30]

$$T(L, t) = \Delta T_{max} \left[ 1 + 2 \sum_{n=1}^{\infty} (-1)^n \exp\left(-\frac{n^2 \pi^2 a t}{L^2}\right) \right], \quad (\text{Eq. 2.21})$$

where the maximum temperature  $\Delta T_{max}$  at the rear surface is given by  $\Delta T_{max} = q / (\rho c_p L)$ . With the definition of two dimensionless parameters  $V(L, t) = T(L, t) / \Delta T_{max}$  and  $\omega = \pi^2 a t / L^2$  Equation 2.21 is rewritten as follows [30]

$$V(\omega) = 1 + 2 \sum_{n=1}^{\infty} (-1)^n \exp(-n^2 \omega). \quad (\text{Eq. 2.22})$$

From the plot of Equation 2.22 shown in Figure 2.3 relations to obtain the thermal diffusivity are deduced. The dashed line in Figure 2.3 shows that for  $V(\omega) = 0.5$  the parameter  $\omega = 1.3698$ , which leads to the following relation for the thermal diffusivity [30]

$$a = \frac{1.3698L^2}{\pi^2 t_{1/2}}, \quad (\text{Eq. 2.23})$$

where  $t_{1/2}$  is the time that is required for the temperature of the rear surface to reach half of the maximum temperature (see also Figure 2.2b). With Equation 2.23 one is able to determine the thermal diffusivity without knowing the amount of energy absorbed at the front surface as long as (i) the light flash is negligibly short compared to the characteristic time of the transient temperature rise, (ii) the specimen is non-transparent to the light pulse and to thermal radiation, (iii) the specimen

is uniform in geometry and homogeneous in structure, and (iv) the heat loss is negligible. Non-transparent solids are the ideal materials to determine the thermal diffusivity over a wide range (i.e., 0.1 to 1000 mm<sup>2</sup>s<sup>-1</sup> [31]). For transparent materials a suitable thin coating of an opaque material is required. The measurement of liquids or molten materials requires a special container construction. Here it is important to minimize the influence of convection.

Besides the thermal diffusivity the flash method also determines the specific heat capacity  $c_p$  of the specimen if the total amount of absorbed energy  $Q$  is known. To determine  $c_p$  and with that the thermal conductivity using Equation 2.3 from the same measurement the amount of absorbed energy by the specimen  $Q$  has to be known. This energy is obtained by performing identical measurements on a reference sample with known  $c_p$ . The power and length of the pulse as well as the irradiated surface and the absorption properties of the specimen have to be identical. Comparable absorption properties are realized by applying a suitable coating on both of the specimen surfaces. Under the assumptions the relation for the derived specific heat capacity  $c_p^u$  is as follows

$$c_p^u = \frac{c_p^{ref} \rho^{ref} L^{ref} T_{max}^{ref}}{\rho^u L^u T_{max}^u}, \quad (\text{Eq. 2.24})$$

where the superscript  $u$  refers to the specimen with unknown  $c_p$  and  $ref$  refers to the reference sample. It is worth noting that this method is only applicable for isotropic specimen. Eventually, the thermal conductivity is calculated following Equation 2.3 using the measured values for  $a$  and  $c_p$ .

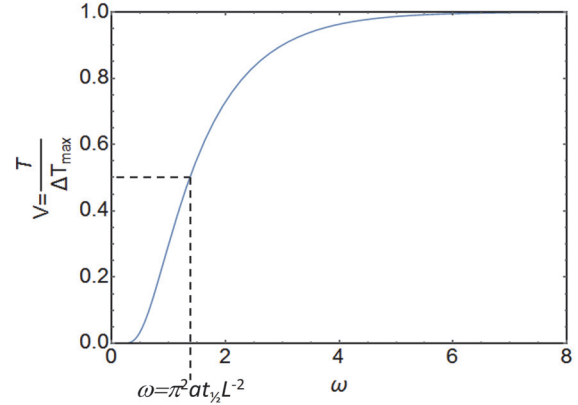


**Figure 2.3** Plot of the dimensionless function  $V(\omega)$  showing the temperature rise of the rear surface in a flash experiment

Comparing the typical temperature profile of a flash measurement (see Figure 2.2b) with the idealized case (Figure 2.3), it becomes evident that in a real measurement Equation 2.23 needs to be corrected to account for heat losses as well as the finite pulse length  $\tau$ . A finite pulse correction is required when the temperature rise time becomes short compared to the pulse length (i.e.,  $t_{1/2} < 50 \times \tau$ ). As is apparent from Equation 2.23 this is the case for very thin materials or materials with high thermal diffusivity. The effects caused by a finite light pulse is usually be corrected using the relation derived by Taylor and Clark [32]

$$a = \frac{C_1 L^2}{C_2 t_{1/2} - \tau}, \quad (\text{Eq. 2.25})$$

where  $C_1$  and  $C_2$  are specific constants for the triangular pulse shape with pulse duration  $\tau$ . Correcting the loss of heat becomes necessary for measurements of very thick samples or samples with low thermal diffusivity. For such samples the temperature rise time will be long. Therefore, heat losses due to radiation losses from the surface as well as conduction losses to the sample holder must be accounted for. The correction for the cooling part of the temperature profile (see section III in Figure 2.2b) by Cowan [33] uses the temperature ratios of  $T(5t_{1/2})/T(t_{1/2})$  and  $T(10t_{1/2})/T(t_{1/2})$ . For the adiabatic case (Equation 2.23) these ratios are equal to two. If heat is lost these temperature ratios are below two. The correction factor  $K_C$  for  $5t_{1/2}$  and  $10t_{1/2}$  are calculated from the polynomial fit

$$K_C = A + B\left(\frac{T(xt_{1/2})}{T(t_{1/2})}\right) + C\left(\frac{T(xt_{1/2})}{T(t_{1/2})}\right)^2 + D\left(\frac{T(xt_{1/2})}{T(t_{1/2})}\right)^2 + E\left(\frac{T(xt_{1/2})}{T(t_{1/2})}\right)^3 \\ + F\left(\frac{T(xt_{1/2})}{T(t_{1/2})}\right)^4 + G\left(\frac{T(xt_{1/2})}{T(t_{1/2})}\right)^5 + H\left(\frac{T(xt_{1/2})}{T(t_{1/2})}\right)^7, \quad (\text{Eq. 2.26})$$

where  $x$  is 5 or 10. This correction factor is used to calculate the thermal diffusivity as follows

$$a_{Cowan} = \frac{L^2}{t_{1/2}} K_C. \quad (\text{Eq. 2.27})$$

Clark and Taylor [34] introduced heat loss corrections for the rise curve (see section II in Figure 2.2b) using the ratio  $t_{3/4}/t_{1/4}$  which is the time to reach 75% of the maximum temperature divided by the time to reach 25% of the maximum with the ideal value  $t_{3/4}/t_{1/4} = 2.27$  (Equation 2.22). The correction factor  $K_{CT}$  is then calculated from

$$K_{CT} = -0.3461467 + 0.361578 \frac{t_{3/4}}{t_{1/4}} - 0.0652043 \left( \frac{t_{3/4}}{t_{1/4}} \right)^2, \quad (\text{Eq. 2.28})$$

which leads to the corrected thermal diffusivity

$$a_{Cowan} = \frac{L^2}{t_{1/2}} K_{CT}. \quad (\text{Eq. 2.29})$$

In addition to the above mentioned correction there have been various other procedures introduced to refine the determination of the thermal diffusivity for specific measurement conditions [35-38].

With the standard setup for the Flash method (see Figure 2.2a) the thermal diffusivity through the thickness of a disc shaped specimen is measured. For materials with isotropic thermal properties the measured thermal diffusivity applies to all directions, in particular to the in-plane or radial direction of the disc. If a material has anisotropic thermal properties the in-plane value will differ from the

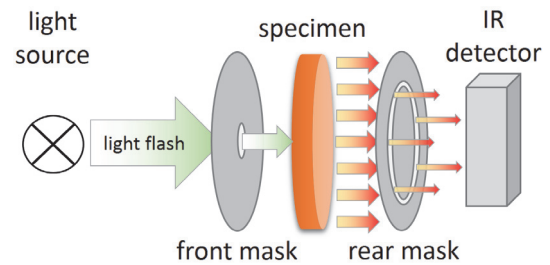


**Figure 2.4** Schematic setup of the modified flash method to measure the thermal diffusivity in radial direction.

through-plane conductivity. The standard flash method is modified for anisotropic samples by adding two masks to the setup, as presented in Figure 2.4. The mask between the light source and the specimen is used to collimate the light through a pinhole and with that the heat is applied to a small spot in the center of the front surface of the specimen. The mask between the specimen and the detector is used to block the thermal radiation of the rear surface at the center of the specimen but allows the radiation to pass through an annulus, which has a substantially larger diameter compared to the diameter of the pinhole in the first mask. This allows a detection of the heat flow in the in-plane direction of the specimen resulting in a temperature rise recorded by the IR detector, that corresponds to the radial thermal diffusivity. The calculation of the radial thermal diffusivity was introduced by Donaldson and Taylor [39] using a two-dimensional model for the temperature profile, where the dimensionless temperature is expressed as a product of a radial and an axial component. The thermal diffusivity is deduced from the temperature profile in a similar fashion by taking the time  $t_{1/2}$  in which the temperature rises to half of its maximum

$$a_{radial} = R^2 \frac{\tau_{1/2}}{t_{1/2}}, \quad (\text{Eq. 2.30})$$

where  $R$  is the radius of the pinhole in the front mask. The parameter  $\tau_{1/2}$  depends on the radius of the of the pinhole, the radius of the annulus in the rear mask, the sample thickness, and the axial thermal diffusivity, which is determined in a standard flash experiment.

## 2.4 Thermal expansion in solid materials

It is commonly known that solid materials (as well as liquids and gases) change their volume when the temperature is changing. However, if one assumes that atoms in a lattice are moving in a harmonic potential, the volume of a solid material is independent of the temperature. Since the attractive and repulsive forces between two neighboring atoms are not symmetric, the potential for an atom in a lattice is anharmonic. In the classical picture shown in Figure 2.5 the atoms are vibrating in such potential. With increasing temperature the mean distance of the atom increases. Therefore, the volume of the solid body expands. However, this model only takes into account longitudinal while neglecting transversal vibrations, which cause the atoms to be pulled towards each other. Thus, this classical model cannot explain negative thermal expansion, which occurs in some solids but points out anharmonicity as the most important mechanism for thermal expansion.

According to the theoretical approach by Grüneisen [40] the volume derivative of the equation of state leads to the connection between thermal expansion, compressibility, and specific heat for monoatomic solids. In the theory of Grüneisen all independent vibrations have the same frequency  $\omega$ . Moreover, the free energy  $F$  of a solid body contains only the energy of the lattice vibrations, and the elastic energy in absence of defects and electronic excitations. It is given by [42]

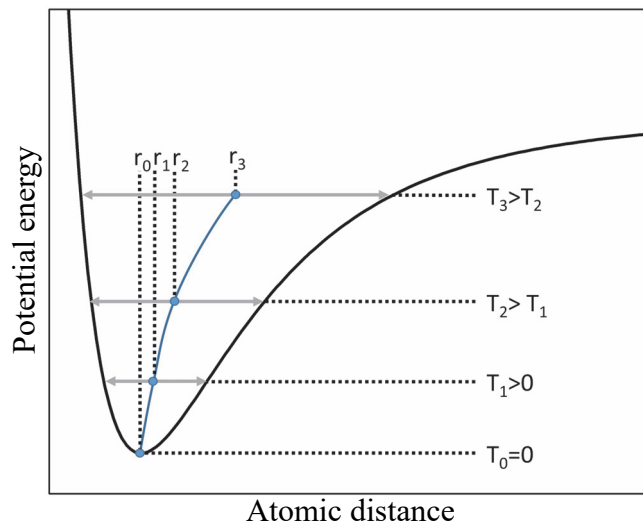


**Figure 2.5** Classical picture of atoms vibrating in an anharmonic potential leading to an increase in the mean atomic distance (blue dots) with increasing temperature.

$$F = \frac{BV}{2} \left( \frac{\delta V}{V} \right)^2 + \sum_{q,j} \left[ k_B T \ln \left( (1 - e^{-\hbar\omega_{q,j}/k_B T}) + \frac{1}{2} \hbar\omega_{q,j} \right) \right], \quad (\text{Eq. 2.31})$$

where  $V$  is the volume,  $\delta V$  is the small volume change,  $B$  is the bulk modulus, and  $q$  is the wave vector with the frequency  $\omega_q$ , while summation goes over all  $q$  and all phonon branches  $j$ . The volume derivative of Equation 2.31 leads to the pressure

$$p = \left( \frac{\partial F}{\partial V} \right)_T = -B \left( \frac{\delta V}{V} \right) - \hbar \sum_{q,j} \frac{\partial \omega_{q,j}}{\partial V} \left[ \frac{1}{e^{-\hbar\omega_{q,j}/k_B T} - 1} + \frac{1}{2} \right]. \quad (\text{Eq. 2.32})$$

Here the anharmonicity becomes apparent because the volume change results in a change of frequency (i.e.,  $(\partial\omega_{q,j}/\partial V) \neq 0$ ). For a solid body with harmonic potential the frequency change is zero. Assuming that the relative frequency change is independent of the frequency and proportional to the relative volume change leads to the relation [40,41]

$$\frac{\partial \omega_{q,j}}{\omega_{q,j}} = -\gamma \frac{\delta V}{V}, \quad (\text{Eq. 2.33})$$

where  $\gamma$  is the dimensionless Grüneisen parameter, which relates the phonon frequency to volume a change. It is a characteristic constant for a material and a given phonon branch. In most materials  $\gamma$  is positive and close to one. With the Grüneisen parameter Equation 2.32 is simplified to [42]

$$p = -B \frac{\delta V}{V} + \frac{\gamma}{V} \sum_{q,j} \hbar \omega_{q,j} \left[ \frac{1}{e^{-\hbar\omega_{q,j}/k_B T} - 1} + \frac{1}{2} \right]. \quad (\text{Eq. 2.34})$$

The sum in Equation 2.34 contains the energy of all phonons including the zero-point energy which is the total internal energy  $U$ . From that one obtains the equation of state

$$pV = -B\delta V + \gamma U(T). \quad (\text{Eq. 2.35})$$

The temperature derivative of the equation of state leads to one of the many formulations of the Grüneisen relation by using the definition of the bulk modulus ( $B = -V(\partial p/\partial V)_T$ )

$$\gamma = \frac{\alpha_V B V}{C_V}, \quad (\text{Eq. 2.36})$$

with

$$\alpha_V = \frac{1}{V} \left( \frac{\partial V}{\partial T} \right)_p \quad \text{and} \quad C_V = \left( \frac{\partial U}{\partial T} \right)_V, \quad (\text{Eq. 2.37})$$

where  $\alpha_V$  is the volumetric coefficient of thermal expansion (CTE) and  $C_V$  is the heat capacity. Since the bulk modulus does not change much with temperature, the ratio of thermal expansion and the heat capacity is more or less constant over a wide temperature range. Thus, the Grüneisen parameter is often referred to as a constant. However, the assumption that the frequencies for different crystal vibrations are the same is often invalid. Consequently, the Grüneisen parameter  $\gamma$  is often replaced by multiple parameters  $\gamma_j$  for each of the different vibrational branches  $j$ . The label  $j$  can also include other contributions to the thermal expansion such as magnetic or electronic ones. For longitudinal optical and acoustic modes the Grüneisen parameters are usually positive, whereas for transverse acoustic modes the Grüneisen parameter may be negative [44].

Another important and widely used definition for the thermal expansion is the linear coefficient of thermal expansion given by

$$\alpha_L = \frac{1}{L_0} \frac{\partial L}{\partial T}, \quad (\text{Eq. 2.38})$$

where  $L_0$  is a particular length of a material. When the linear CTE does not change much over a temperature interval  $\Delta T$  Equation 2.38 is simplified to obtain the mean linear CTE

$$\bar{\alpha}_L = \frac{1}{L_0} \frac{\Delta L}{\Delta T}, \quad (\text{Eq. 2.39})$$

where  $\Delta L$  is the absolute length change over the temperature interval  $\Delta T$ . The CTE of Equations 2.38 and 2.39 are often referred to as physical and technical coefficient of thermal expansion. For isotropic materials the volumetric CTE  $\alpha_V$  is three times the linear CTE  $\alpha_L$ . Additionally, a commonly used expression to compare the thermal expansion between different materials is the relative length change given by

$$\Delta L_{rel}(T) = \frac{\Delta L(T)}{L_0}, \quad (\text{Eq. 2.40})$$

where  $\Delta L(T)$  is the absolute length change at the temperature  $T$ . Furthermore, the thermal expansion is correlated to the melting point for metals with cubic structure, i.e., the higher the melting point the lower the CTE. Therefore, aluminum (22.5 ppmK<sup>-1</sup>) [43] has a higher CTE than copper (16.5 ppmK<sup>-1</sup>) [45] and silver (18.8 ppmK<sup>-1</sup>) [46]. Compared to semiconductors like silicon (2.4 ppmK<sup>-1</sup>) [45] the CTE of metals is a factor of 7 to 9 larger. Such a large CTE mismatch is problematic for thermal management applications, where semiconductors are in direct contact with metals for cooling purposes, since it causes thermal stress that may be higher than the strength of the materials to be cooled.



On the other hand these metals conduct heat very effectively, much better than metals with lower CTE. To tackle this problem one approach is to lower the thermal expansion of these highly conducting materials by reinforcing them with low expanding materials. The next section will suggest, that carbon materials are prime candidates to address this challenging task.

### 2.4.1 Thermal expansion of carbon materials

As already elaborated in Section 2.1.2 carbon materials have special heat conducting properties, that are highly anisotropic for, e.g.,  $sp^2$  carbons. Experimental observations also revealed unusual expansion behaviors for various carbon allotropes. Nelson and Riley [47] investigated the thermal expansion of graphite in dependence of the crystal orientation using the x-ray diffraction method. They reported a huge anisotropy for the CTE along ( $a$ - $b$  axis) and perpendicular ( $c$  axis) to the basal planes. It was found that below  $\sim 400^\circ\text{C}$  graphite contracts along the basal plane direction and, therefore, has a negative CTE ( $\alpha_{\text{Gr},ab} = -1.5 \text{ ppmK}^{-1}$  at room temperature) [47] as well as a negative Grüneisen parameter [48,49]. Above  $400^\circ\text{C}$  the CTE is positive, but remains below  $1 \text{ ppmK}^{-1}$  till up to  $800^\circ\text{C}$ .

In the direction perpendicular to the carbon layers graphite expands strongly ( $\alpha_{\text{Gr},c} = 27.1 \text{ ppmK}^{-1}$  at room temperature), which is even higher than the CTE of the metals discussed above. At  $\sim 400^\circ\text{C}$  the expansion coefficient reaches a plateau at  $28 \text{ ppmK}^{-1}$  before increasing further towards higher temperatures [47]. As mentioned before, the covalent bonding of the carbon atoms in the plane is much stronger than the bonding between adjacent layers. As result the elastic modulus is much larger between the layers as opposed to the direction along the layers [50,51]. Mounet and Marzari [49] calculated the in-plane Grüneisen parameters for graphite and found that  $\gamma$  is negative and as low as  $-40$  for the lowest modes, i.e., the lowest transversal acoustic mode (ZA; also called flexural or bending mode) and the (ZO') mode. For low temperatures this negative Grüneisen parameter will be dominant since most optical modes with  $\gamma > 0$  are not excited resulting in a negative thermal expansion along the basal plane  $\alpha_{\text{Gr},ab} < 0$  [48,52]. With increasing temperature more optical modes with positive  $\gamma$  will be excited and eventually dominating the contraction effect leading to a positive CTE along the basal planes. For a hexagonal crystal the mean linear CTE is given by

$$\bar{\alpha} = \frac{2}{3}\alpha_{ab} + \frac{1}{3}\alpha_c, \quad (\text{Eq. 2.41})$$

which is approximately  $8 \text{ ppmK}^{-1}$  for graphite at room temperature and is the value measured for polycrystalline graphite specimen [47].

In graphene the negative in-plane thermal expansion is even more pronounced, which was calculated to  $-7 \text{ ppmK}^{-1}$  at room temperature [53,54]. Again the flexural phonons with large negative Grüneisen parameter are the dominating factor for the negative CTE [49,55]. Yoon *et al.* [56] estimated the CTE of graphene at room temperature to  $-8 \text{ ppmK}^{-1}$  by temperature-dependent Raman spectroscopy. This is exceeding the in-plane contraction of graphite because in contrast to graphite there are no interplanar interactions that suppress the out of plane vibrations. This so called membrane effect was predicted by Lifshitz [57] and underlines the importance of flexural modes in layered materials. Rolling a graphene sheet to a carbon nanotube likewise suppresses contraction. Thus, CNTs exhibit lower contraction than graphene. Yosida [58] and Maniwa *et al.* [59] investigated the thermal expansion of single-walled carbon nanotube bundles using x-ray diffraction. Both studies confirmed that the CTE of the radius, i.e., normal to the bundle axis, is  $-1.5 \text{ ppmK}^{-1}$  at room temperature and remains negative for higher temperatures. Assuming negative expansion along the tube axis as it is observed in graphite or graphene, the volume expansion of single-walled CNTs is expected to be negative [58]. The inter-tube gap expansion is larger than the  $c$  axis expansion in graphite exhibiting a value of  $42 \text{ ppmK}^{-1}$  indicating that the lattice anharmonicity in nanotube bundles is larger than in graphite [59]. Furthermore, molecular dynamics simulations revealed, that the radial expansion is slightly lower than the axial [52]. In addition, it could be shown that the CTE increases with increasing nanotube curvature, i.e., decreasing radius. Zhang *et al.* [60] investigated the CTE of individual multi-walled CNTs and found that all walls show radial contraction as well as negative CTE in axial direction, which was independent of the tube diameter.

In contrast to the contraction of the  $sp^2$  allotropes discussed above diamond does not show negative expansion between 0 and 1600 K and is  $1 \text{ ppmK}^{-1}$  at room temperature [61,62] confirmed by theoretical calculations [52]. The expansion is still one order of magnitude lower than typical metals and also lower than silicon [45]. Again the strong covalent bonding between the carbon atoms is the reason for the low expansion.

Incorporating the above mentioned carbon materials into metal composite materials is a promising approach to tailor the thermal expansion, the thermal conductivity, as well as the mass density of advanced composites for thermal management applications.

## 2.4.2 Thermal expansion of composite materials

In a composite where matrix and filling particles expand differently when the temperature is changed the effective thermal conductivity may be predicted by various approaches. The simplest way is to calculate the thermal expansion of the composite by rule of mixture (ROM) using the CTE of the matrix  $\alpha_m$  and the filling material  $\alpha_f$

$$\alpha_{ROM} = f\alpha_f + (1-f)\alpha_m, \quad (\text{Eq. 2.42})$$

where  $f$  is the volume fraction of the filling particles. Calculating the thermal expansion of the composite by the ROM gives a rough estimate of the composite CTE, since the elastic properties of the components are neglected. Shapery derived a model for composites with isotropic and anisotropic thermal expansion containing isotropic phases [63]. It is based on extremum principles of thermoelasticity and considers the stress interaction between the composite components. The model predicts upper (+) and lower (-) bounds for the CTE given by

$$\alpha_{Shapery}^{(+)} = \alpha_f + (\alpha_m - \alpha_f) \frac{B_m(B_f - B_{HS}^{(-)})}{B_{HS}^{(-)}(B_f - B_m)}, \quad (\text{Eq. 2.43})$$

where the indices  $f$  and  $m$  refer to filler and matrix.  $B_{HS}^{(-)}$  is the Hashin and Shtrikman lower limit of the bulk modulus given by [64]

$$B_{HS}^{(-)} = B_m + \frac{f}{\frac{1}{B_f - B_m} + \frac{1-f}{B_m - 4/3 G_m}}. \quad (\text{Eq. 2.44})$$

The upper limit of the Bulk modulus  $B_{HS}^{(+)}$  yields the lower bound of the CTE  $\alpha_{Shapery}^{(-)}$ . It is obtained from Equation 2.44 by replacing the index  $f$  by  $m$ , and vice versa. If the bulk modulus  $B$  and the shear modulus  $G$  are unknown they can be calculated using the relations

$$B = \frac{E}{3(1-2\nu)} \quad \text{and} \quad G = \frac{E}{2(1+\nu)}, \quad (\text{Eq. 2.45})$$

where  $E$  is the Young's modulus and  $\nu$  is the Poisson's ratio of the composite component. Shapery showed that the upper bound of the CTE is equal to the expression derived earlier by Kerner for isotropic and homogeneous composites reinforced with spherical particles [65]. In addition, Shapery derived expressions for the longitudinal ( $\parallel$ ) and transverse ( $\perp$ ) CTE in composites containing aligned fibers with [63]

$$\alpha_{\parallel} = \frac{f\alpha_f E_f + (1-f)\alpha_m E_m}{fE_f + (1-f)E_m} \quad (\text{Eq. 2.46})$$

and

$$\alpha_{\perp} = (1-f)(1+\nu_m)\alpha_m + f(1-\nu_f)\alpha_f - \alpha_{\parallel}\nu_c, \quad (\text{Eq. 2.47})$$

where  $\nu_c = f\nu_f + (1-f)\nu_m$  is the Poisson's ratio of the composite. However, in some

cases these models fail to predict the expansion behavior accurately, especially when internal stress in the composite is present, which is introduced during the creation process when the composite components have a large CTE mismatch. Consequently, plastic deformations of the matrix and the filler may occur, which have an influence on the expansion of the composite. Moreover, the predictions become less accurate for reinforcing materials with anisotropic thermal expansion.

## 2.5 Raman scattering

Theoretically predicted by Smekal [66], discovered by Raman and Krishnan in liquids [67] and Landsberg and Mandelstam in crystals [68] the so-called Raman effect describes the inelastic scattering of a photon by a molecule or a crystal. Compared to elastic scattering (Rayleigh scattering) of photons with matter Raman scattering is several orders of magnitude less likely to happen, which made the observation of the effect difficult before the availability of lasers. If a photon scatters inelastically with a molecule or a crystal two different processes may happen. The material may absorb energy by exciting a phonon while the energy of the scattered photon is reduced by the phonon energy. This process is referred to as Stokes scattering. If the molecule or crystal is in an excited vibrational state and a photon scatters inelastically the material may lose the energy of a phonon, which increases the energy of the scattered photon by the energy of the destroyed phonon. This process is referred to as anti-Stokes scattering. A typical Raman spectrum shows the intensity of the scattered light over its frequency difference to the incident photons. The frequency shifts for Stokes and anti-Stokes scattering are symmetric around zero shift, since they belong to the same phonon energy. However, the intensities for the Stokes and anti-Stokes lines are different, because they depend on the initial population of the phonon states, which is temperature dependent. Raman spectroscopy is a very versatile technique able to identify materials, investigate phonon frequencies and peak widths, the presence of impurities in a material, the level of doping, measure uniaxial and hydrostatic stress, molecule or crystal orientation, and many other structural analyses. [69]

### 2.5.1 Raman spectroscopy of graphite

In this study Raman spectroscopy will be utilized on graphite to verify the presence of graphite itself, the presence of defects or disorder in the carbon lattice and the orientation of the graphite layers in a particular system, i.e., graphite embedded in a metal matrix.

The crystallographic space group of graphite is  $D_{6h}^4$  having twelve vibrational modes at

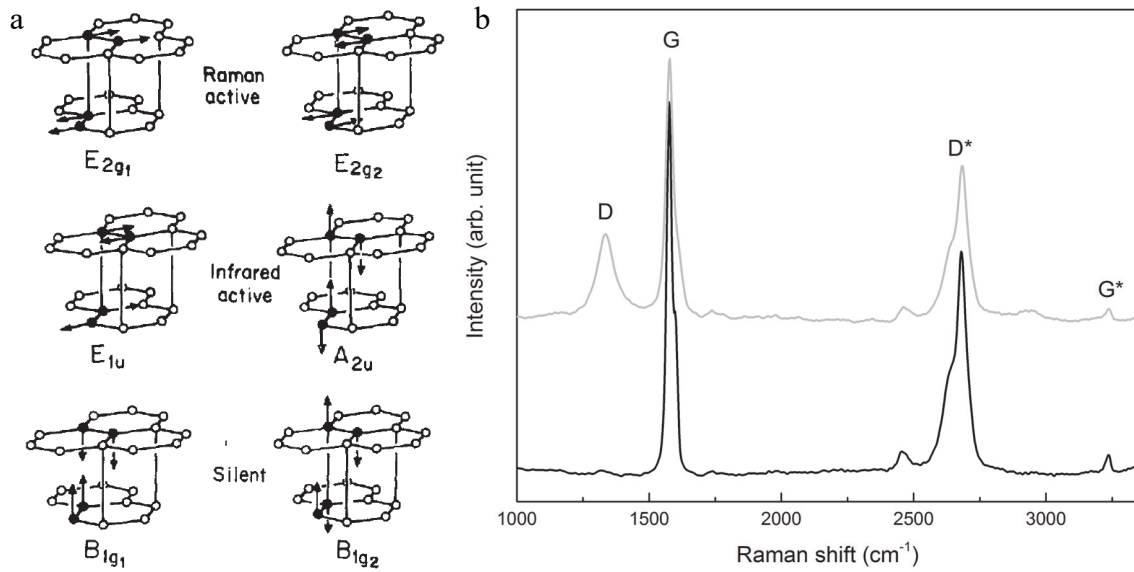


**Figure 2.6 (a)** Optical lattice modes in graphite with indicated Raman and infrared activity (taken from [70]). **(b)** Raman spectrum of graphite taken at a well ordered (black line) and a disordered (gray line) part of a graphite flake. The spectrum for the disordered part was shifted for clarity.

$q = 0$  with three acoustic modes, three infrared-active modes, two silent modes, and four Raman-active modes shown in Figure 2.6a [70,71]. The Raman-active  $E_{2g}$  modes were measured by Tuinstra and Koenig [72], and Nemanich and Solin [73] directly using Raman spectroscopy. The typical Raman spectrum of a well ordered graphite flake is presented in Figure 2.6b containing the first-order spectrum with the  $E_{2g}$  mode at around  $1583 \text{ cm}^{-1}$  often referred to as G line. The second-order Raman spectrum contains the overtone of the G line - the G\* peak - which lies higher than twice the frequency of the G line, due to overbending of the longitudinal optical branches of graphite [71]. Moreover, Figure 2.6b shows the Raman spectrum of the disordered part of graphite, taken at the edge of the flake, which contains an additional peak at around  $1370 \text{ cm}^{-1}$ . This mode is assigned to the disorder in graphite and, therefore, named D mode [72]. The D\* mode in the second order spectrum is very close to twice the Raman shift of the D line and is assigned to be an overtone of the D peak [71].

### 2.5.2 Selection rules for the G line

The scattering efficiency or the intensity of the Raman lines depends on the polarization of the incoming and the scattered light. To calculate the selection rules for a specific Raman process one uses the so-called second rank Raman tensor  $\mathbf{R}$ , which is specific for each of the crystallographic point groups and is defined such that it contains a numerical

constant [74]. If one is only interested in relative and not absolute Raman intensities, it is not necessary to know this constant. The intensity  $I$  is given by

$$I \propto |e_{in} \cdot \mathbf{R} \cdot e_{sc}|^2, \quad (\text{Eq. 2.48})$$

where  $e_{in}$  and  $e_{sc}$  are the polarization vectors of the incoming and the scattered light and  $\mathbf{R}$  is the Raman tensor for the phonon, which is found in literature [74]. In this study the polarization dependence of the G line in the Raman spectrum of graphite will be used to determine the orientation of the graphite planes, in particular for graphite flakes embedded into a metal matrix. For the  $E_{2g}$  transition the Raman tensors are [74]

$$\mathbf{R}_1 = \begin{bmatrix} 0 & f & 0 \\ f & 0 & 0 \\ 0 & 0 & 0 \end{bmatrix} \text{ and } \mathbf{R}_2 = \begin{bmatrix} f & 0 & 0 \\ 0 & -f & 0 \\ 0 & 0 & 0 \end{bmatrix}, \quad (\text{Eq. 2.49})$$

where  $f$  is a constant factor. The total Raman intensity is then obtained by

$$I \propto |e_{in} \cdot \mathbf{R}_1 \cdot e_{sc}|^2 + |e_{in} \cdot \mathbf{R}_2 \cdot e_{sc}|^2. \quad (\text{Eq. 2.50})$$

Lets now consider a well ordered graphite crystal, where the hexagonal carbon planes are oriented in the  $x$ - $y$  plane of a Cartesian coordinate system, as indicated in Figure 2.7a. For simplicity, the polarization vectors of the incoming and the scattered light have the same direction, which is easy to realize experimentally in a Raman setup. Using

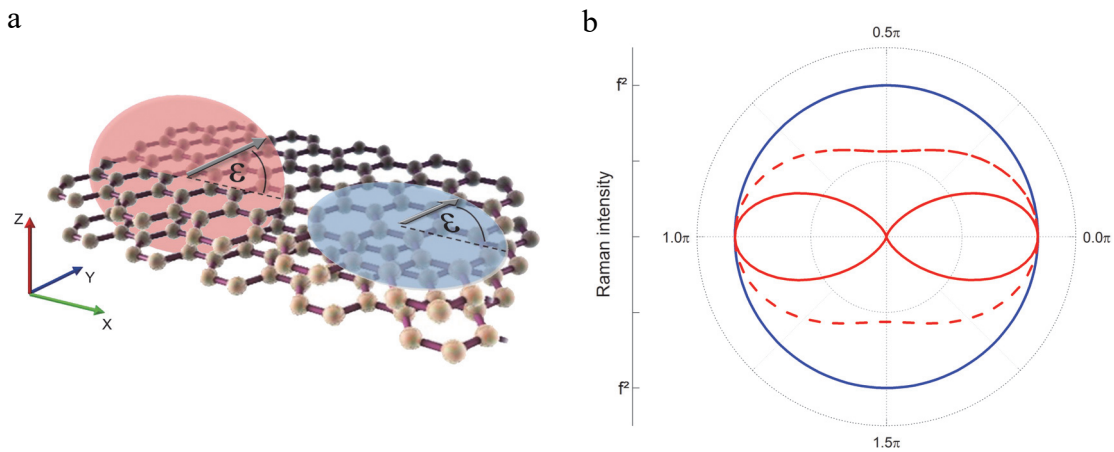


**Figure 2.7 (a)** Scheme for the orientation of a graphite basal plane with respect to the polarization vector. The blue/red circle indicates the polarization vector is changed in the  $x$ - $y$  plane/ $x$ - $z$  plane. **(b)** Polar plot of the relative Raman intensities in dependence of the polarization angle calculated with Equations 2.52 (blue curve) and 2.54 (red curve). The dashed curve shows the intensity for a graphite crystal that is rotated by  $60^\circ$  about the  $x$  axis while the polarization is changed in the  $x$ - $z$  plane.

Equation 2.50 the selection rules for Raman intensity of the G peak are calculated in dependence of the angle of the polarization vector with respect to the orientation of the graphite planes. Let us first consider the rotation of the polarization vectors in the  $x$ - $y$  plane (as indicated by the blue circle in Figure 2.7a). The polarization vectors are expressed as

$$e_{in,1} = e_{sc,1} = \begin{pmatrix} \cos(\varphi) \\ \sin(\varphi) \\ 0 \end{pmatrix}, \quad (\text{Eq. 2.51})$$

where  $\varphi$  is the rotation angle of the polarization. The total Raman intensity is then proportional to

$$I_1(\varphi) \propto |e_{in,1} \cdot \mathbf{R}_1 \cdot e_{sc,1}|^2 + |e_{in,1} \cdot \mathbf{R}_2 \cdot e_{sc,1}|^2 = f^2, \quad (\text{Eq. 2.52})$$

and, therefore, the intensity is independent of polarization changes within the  $x$ - $y$  plane, i.e., parallel to the graphite basal plane. If one changes the polarization of the incoming and the scattered light within the  $x$ - $z$  plane (as indicated by the red circle in Figure 2.7a) the polarization vectors are expressed as

$$e_{in,2} = e_{sc,2} = \begin{pmatrix} \cos(\varphi) \\ 0 \\ \sin(\varphi) \end{pmatrix}. \quad (\text{Eq. 2.53})$$

The polarization dependence of the Raman intensity of the G peak is again calculated using Equation 2.50 and results in

$$I_2(\varphi) \propto |e_{in,2} \cdot \mathbf{R}_1 \cdot e_{sc,2}|^2 + |e_{in,2} \cdot \mathbf{R}_2 \cdot e_{sc,2}|^2 = f^2 \cos^4 \varphi. \quad (\text{Eq. 2.54})$$

The G line has a maximum when the polarization vectors point in  $x$  direction (i.e.,  $\varphi = 0, \pi$ ) and is zero when the polarization vectors point in  $z$  direction (i.e.,  $\varphi = \pi/2, 3\pi/2$ ), as shown in Figure 2.7b. Due to the symmetry the same intensity dependence applies when the polarization is changed in the  $y$ - $z$  plane. It is worth to mention that for all other orientation scenarios the intensity profile lies in between the above mentioned extreme cases (e.g., dashed line in Figure 2.7b representing a rotation of the basal plane by  $60^\circ$  about the  $x$  axis).

### 2.5.3 Phonons under strain in silicon

The Raman spectrum of silicon (Si) contains a peak around  $520 \text{ cm}^{-1}$  corresponding to the first order optical phonon for zero wave vector that is three fold degenerate. Shown by Hart *et al.* [75] and Balkanski *et al.* [76] the frequency shifts when the temperature is changed due to anharmonic effects. Moreover, the frequency of the phonon is sensitive to stress in the material, which was investigated by Anastassakis *et al.* [77]. The effect of strain on the shift of the Raman modes in Si is described by the secular equation [78]

$$\begin{bmatrix} p\varepsilon_{11} + q(\varepsilon_{22} + \varepsilon_{33}) - \lambda & 2r\varepsilon_{12} & 2r\varepsilon_{13} \\ 2r\varepsilon_{12} & p\varepsilon_{22} + q(\varepsilon_{33} + \varepsilon_{11}) - \lambda & 2r\varepsilon_{23} \\ 2r\varepsilon_{13} & 2r\varepsilon_{23} & p\varepsilon_{33} + q(\varepsilon_{11} + \varepsilon_{22}) - \lambda \end{bmatrix} = 0, \quad (\text{Eq. 2.55})$$

where  $p$ ,  $q$ , and  $r$  are the phonon deformation potentials of the material and  $\varepsilon_{ij}$  are the components of the strain tensor  $\varepsilon$ . The eigenvalues  $\lambda_i = \omega_i^2 - \omega_0^2$  ( $i=1, 2, 3$ ) predict the strain induced Raman frequency shifts

$$\Delta\omega_i = \omega_i - \omega_0 \approx \frac{\lambda_i}{2\omega_0}, \quad (\text{Eq. 2.56})$$

where  $\omega_0$  is the frequency for zero strain. It becomes apparent that strain lifts the degeneracy, while the intensity depends on the polarization of the incoming and the scattered light as well as the strain tensor  $\varepsilon$ , which is connected to stress  $\sigma$  by Hook's law

$$\varepsilon = \mathbf{S} \cdot \sigma, \quad (\text{Eq. 2.57})$$

with  $\mathbf{S}$  being the fourth rank compliance tensor. The eigenvalues give the frequency shift for each polarization direction

$$\Delta\omega_1 = \frac{\lambda_1}{2\omega_0} = \frac{1}{2\omega_0} [p\varepsilon_{11} + q(\varepsilon_{22} + \varepsilon_{33})], \quad (\text{Eq. 2.58})$$

$$\Delta\omega_2 = \frac{\lambda_2}{2\omega_0} = \frac{1}{2\omega_0} [p\varepsilon_{22} + q(\varepsilon_{33} + \varepsilon_{11})], \quad (\text{Eq. 2.59})$$

and

$$\Delta\omega_3 = \frac{\lambda_3}{2\omega_0} = \frac{1}{2\omega_0} [p\varepsilon_{33} + q(\varepsilon_{11} + \varepsilon_{22})]. \quad (\text{Eq. 2.60})$$

In the case of uniaxial stress  $\sigma_{11}$  along the  $x$  direction the components of the strain tensor



are given by  $\varepsilon_{11} = S_{11}\sigma_{11}$ ,  $\varepsilon_{22} = S_{12}\sigma_{11}$ , and  $\varepsilon_{33} = S_{12}\sigma_{11}$  following Equation 2.57, where the  $S_{ij}$  are the components of the compliance tensor. The shift of the third Raman mode is given by [79]

$$\Delta\omega_3 = \frac{\lambda_3}{2\omega_0} = \frac{1}{2\omega_0}[pS_{12} + q(S_{11} + S_{12})]\sigma_{11}, \quad (\text{Eq. 2.61})$$

which is the only mode observed if the scattered light is polarized in the  $z$  direction for a standard back scattering Raman setup [80]. Using  $p$  and  $q$  from Reference [81] as well as  $S_{11}$  and  $S_{12}$  from Reference [82], the shift of the third Raman mode is

$$\Delta\omega_3[\text{cm}^{-1}] \cong -2.30 \times 10^{-9} \sigma_{11}[\text{Pa}], \quad (\text{Eq. 2.62})$$

which means that an uniaxial stress of 1 GPa will shift the Raman peak by about  $2 \text{ cm}^{-1}$ . If biaxial stress in the  $x$ - $y$  plane is present (e.g.,  $\sigma_{11} = \sigma_{22}$  for isotropic stress) Equation 2.60 becomes [79]

$$\Delta\omega_3 = \frac{1}{2\omega_0}[pS_{12} + q(S_{11} + S_{12})](\sigma_{11} + \sigma_{22}) \quad (\text{Eq. 2.63})$$

or

$$\Delta\omega_3[\text{cm}^{-1}] \cong -4.56 \times 10^{-9} \left( \frac{\sigma_{11} + \sigma_{22}}{2} \right) [\text{Pa}]. \quad (\text{Eq. 2.64})$$

That means that an isotropic biaxial stress of 1 GPa causes a shift of about  $4 \text{ cm}^{-1}$ . If the stress is compressive the Raman frequency will increase, whereas for tensile stress it decreases. In this study the stress and temperature dependence of the Raman peak in Si will be used to determine induced thermal stress in Si when attached to a heat sink with different CTE.

---

## References

- [1] Fourier JBJ, Freeman A. *The Analytical Theory of Heat*. The University Press, 1878.
- [2] Carslaw HS, Jaeger JC. *Conduction of Heat in Solids*. Clarendon Press, 1986.
- [3] Kittel C. *Introduction to solid state physics*. Wiley, 2005.
- [4] Franz R, Wiedemann G. Ueber die Wärme-Leitungsfähigkeit der Metalle. *Annalen der Physik* 1853, **165**(8): 497-531.
- [5] Ho CY, Powell RW, Liley PE. *Thermal conductivity of the elements: a comprehensive review*. Published by the American Chemical Society, for the National Bureau of Standards, 1974.
- [6] Davis JR, Committee ASMIH. *Copper and Copper Alloys*. ASM International, 2001.
- [7] Hirsch A. The era of carbon allotropes. *Nat Mater* 2010, **9**(11): 868-871.
- [8] Krishnan KS, Ganguli N. Large Anisotropy of the Electrical Conductivity of Graphite. *Nature* 1939, **144**: 667
- [9] Klemens PG, Pedraza DF. Thermal conductivity of graphite in the basal plane. *Carbon* 1994, **32**(4): 735-741.
- [10] Tyler WW, Wilson AC. Thermal Conductivity, Electrical Resistivity, and Thermoelectric Power of Graphite. *Physical Review* 1953, **89**(4): 870-875.
- [11] Hooker CN, Ubbelohde AR, Young DA. *Anisotropy of Thermal Conductance in Near-Ideal Graphite*, vol. 284, 1965.
- [12] Berman R, Foster EL, Ziman JM. *The Thermal Conductivity of Dielectric Crystals: The Effect of Isotopes*, vol. 237, 1956.
- [13] Anthony TR, Banholzer WF, Fleischer JF, Wei L, Kuo PK, Thomas RL, *et al.* Thermal diffusivity of isotopically enriched  $^{12}\text{C}$  diamond. *Physical Review B* 1990, **42**(2): 1104-1111.
- [14] Balandin AA, Ghosh S, Bao W, Calizo I, Teweldebrhan D, Miao F, *et al.* Superior Thermal Conductivity of Single-Layer Graphene. *Nano Letters* 2008, **8**(3): 902-907.
- [15] Ghosh S, Calizo I, Teweldebrhan D, Pokatilov EP, Nika DL, Balandin AA, *et al.* Extremely high thermal conductivity of graphene: Prospects for thermal management applications in nanoelectronic circuits. *Applied Physics Letters* 2008, **92**(15): 151911.
- [16] Ghosh S, Bao W, Nika DL, Subrina S, Pokatilov EP, Lau CN, *et al.* Dimensional crossover of thermal transport in few-layer graphene. *Nat Mater* 2010, **9**(7): 555-558.
- [17] Pop E, Mann D, Wang Q, Goodson K, Dai H. Thermal Conductance of an Individual Single-Wall Carbon Nanotube above Room Temperature. *Nano Letters* 2005, **6**(1): 96-100.
- [18] Kim P, Shi L, Majumdar A, McEuen P. Thermal Transport Measurements of Individual Multiwalled Nanotubes. *Physical Review Letters* 2001, **87**(21).
- [19] Balandin AA. Thermal properties of graphene and nanostructured carbon materials. *Nature materials* 2011, **10**(8): 569-581.
- [20] Nan C-W, Birringer R, Clarke DR, Gleiter H. Effective thermal conductivity of particulate composites with interfacial thermal resistance. *Journal of Applied Physics* 1997, **81**(10).
- [21] Nan C-W. Physics of inhomogeneous inorganic materials. *Progress in Materials Science* 1993, **37**(1): 1-116.

- [22] Nan C-W, Li X-P, Birringer R. Inverse Problem for Composites with Imperfect Interface: Determination of Interfacial Thermal Resistance, Thermal Conductivity of Constituents, and Microstructural Parameters. *Journal of the American Ceramic Society* 2000, **83**(4): 848-854.
- [23] Landau LD, Lifshitz EM. CHAPTER I - ELECTROSTATICS OF CONDUCTORS. In: Landau LD, Lifshitz EM (eds). *Electrodynamics of Continuous Media (Second Edition Revised and Enlarged)*, vol. 8. Pergamon: Amsterdam, 1984, pp 1-33.
- [24] Nan C-W. Effective-medium theory of piezoelectric composites. *Journal of Applied Physics* 1994, **76**(2): 1155-1163.
- [25] Poensgen R. Ein technisches Verfahren zur Ermittlung der Wärmeleitfähigkeit plattenförmiger Stoffe. *Mitteilungen über Forschungsarbeiten auf dem Gebiete des Ingenieurwesens*, vol. 130. Springer Berlin Heidelberg, 1912, pp 25-40.
- [26] Cahill DG, Pohl RO. Thermal conductivity of amorphous solids above the plateau. *Physical Review B* 1987, **35**(8): 4067-4073.
- [27] McLaughlin E, Pittman JFT. *Determination of the Thermal Conductivity of Toluene-A Proposed Data Standard-from 180 to 400k under Saturation Pressure by the Transient Hot-Wire Method I. The Theory of the Technique*, vol. 270, 1971.
- [28] Gustafsson SE, Karawacki E, Khan MN. Transient hot-strip method for simultaneously measuring thermal conductivity and thermal diffusivity of solids and fluids. *Journal of Physics D: Applied Physics* 1979, **12**(9).
- [29] Gustafsson SE. Transient plane source techniques for thermal conductivity and thermal diffusivity measurements of solid materials. *Review of Scientific Instruments* 1991, **62**(3): 797-804.
- [30] Parker WJ, Jenkins RJ, Butler CP, Abbott GL. Flash Method of Determining Thermal Diffusivity, Heat Capacity, and Thermal Conductivity. *Journal of Applied Physics* 1961, **32**(9): 1679-1684
- [31] ASTM E1461-11, Standard Test Method for Thermal Diffusivity by the Flash Method, ASTM International, West Conshohocken, PA, 2011, www.astm.org
- [32] Taylor RE, Clark III LM. Finite pulse time effects in flash diffusivity method. *High Temp.-High Press.* 1974, **6**(1): 65-72.
- [33] Cowan RD. Pulse method of measuring thermal diffusivity at high temperatures. *Journal of Applied Physics* 1963, **34**.
- [34] Clark Iii LM, Taylor RE. Radiation loss in the flash method for thermal diffusivity. *Journal of Applied Physics* 1975, **46**(2): 714-719.
- [35] Cape J, Lehman GW. Temperature and Finite Pulse-Time Effects in the Flash Method for Measuring Thermal Diffusivity. *Journal of Applied Physics* 1963, **34**(7): 1909-1913.
- [36] Azumi T, Takahashi Y. Novel finite pulse-width correction in flash thermal diffusivity measurement. *Review of Scientific Instruments* 1981, **52**(9): 1411-1413.
- [37] Larson KB, Koyama K. Correction for Finite-Pulse-Time Effects in Very Thin Samples using the Flash Method of Measuring Thermal Diffusivity. *Journal of Applied Physics* 1967, **38**(2): 465-474.
- [38] Dusza L. Combined solution of the simultaneous heat loss and finite pulse time corrections with the laser flash method. *High Temp.-High Press.* 1995/1996, **27/28**: 467-73.
- [39] Donaldson AB, Taylor RE. Thermal diffusivity measurement by a radial heat flow method. *Journal of Applied Physics* 1975, **46**(10): 4584-4589.
- [40] Grüneisen E. Theorie des festen Zustandes einatomiger Elemente. *Annalen der Physik* 1912, **344**(12): 257-306.

- 
- [41] Grüneisen E. *The State of a Solid Body*. National Aeronautics and Space Administration, 1959.
- [42] Hunklinger S. *Festkörperphysik*. Oldenbourg, 2007.
- [43] Collins JG, White GK, Swenson CA. The thermal expansion of aluminum below 35 K. *J Low Temp Phys* 1973, **10**(1-2): 69-77.
- [44] Barron THK. Grüneisen parameters for the equation of state of solids. *Annals of Physics* 1957, **1**(1): 77-90.
- [45] White GK. Thermal expansion of reference materials: copper, silica and silicon. *Journal of Physics D: Applied Physics* 1973, **6**(17).
- [46] White GK, Collins JG. Thermal expansion of copper, silver, and gold at low temperatures. *J Low Temp Phys* 1972, **7**(1-2): 43-75.
- [47] Nelson JB, Riley DP. The thermal expansion of graphite from 15°C. to 800°C.: part I. Experimental. *Proc Phys Soc* 1945, **57**(6).
- [48] Suleimanov RA, Abdullaev NA. The nature of negative linear expansion of graphite crystals. *Carbon* 1993, **31**: 1011-1013.
- [49] Mounet N, Marzari N. First-principles determination of the structural, vibrational and thermodynamic properties of diamond, graphite, and derivatives. *Physical Review B* 2005, **71**(20): 205214.
- [50] Gauster WB, Fritz IJ. Pressure and temperature dependences of the elastic constants of compression-annealed pyrolytic graphite. *Journal of Applied Physics* 1974, **45**(8): 3309-3314.
- [51] Bosak A, Krisch M, Mohr M, Maultzsch J, Thomsen C. Elasticity of single-crystalline graphite: Inelastic x-ray scattering study. *Physical Review B* 2007, **75**(15): 153408.
- [52] Schelling PK, Keblinski P. Thermal expansion of carbon structures. *Physical Review B* 2003, **68**(3): 035425.
- [53] Chen C, Rosenblatt S, Bolotin KI, Kalb W, Kim P, Kymissis I, *et al.* Performance of monolayer graphene nanomechanical resonators with electrical readout. *Nat Nano* 2009, **4**(12): 861-867.
- [54] Singh V, Sengupta S, Solanki HS, Dhall R, Allain A, Dhara S, *et al.* Probing thermal expansion of graphene and modal dispersion at low-temperature using graphene nanoelectromechanical systems resonators. *Nanotechnology* 2010, **21**(16): 165204.
- [55] Jin-Wu J, Bing-Shen W, Jian-Sheng W, Harold SP. A review on the flexural mode of graphene: lattice dynamics, thermal conduction, thermal expansion, elasticity and nanomechanical resonance. *J Phys: Condens Matter* 2015, **27**(8): 083001.
- [56] Yoon D, Son Y-W, Cheong H. Negative Thermal Expansion Coefficient of Graphene Measured by Raman Spectroscopy. *Nano Letters* 2011, **11**(8): 3227-3231.
- [57] Lifshitz I. Thermal properties of chain and layered structures at low temperatures. *Zh Eksp Teor Fiz* 1952, **22**(4): 475-486.
- [58] Yosida Y. High-temperature shrinkage of single-walled carbon nanotube bundles up to 1600 K. *Journal of Applied Physics* 2000, **87**(7): 3338-3341.
- [59] Maniwa Y, Fujiwara R, Kira H, Tou H, Kataura H, Suzuki S, *et al.* Thermal expansion of single-walled carbon nanotube (SWNT) bundles: X-ray diffraction studies. *Physical Review B* 2001, **64**(24): 241402.
- [60] Zhang J, Ji L, Zuo J. Large Negative Thermal Expansion of an Individual Carbon Nanotube. *Bulletin of the American Physical Society* 2008, **53**.
- [61] Slack GA, Bartram SF. Thermal expansion of some diamondlike crystals. *Journal of Applied Physics* 1975, **46**(1): 89-98.

- [62] Haruna K, Maeta H. Thermal expansion of synthetic diamond single crystals at low temperatures. *Diamond and Related Materials* 1993, **2**(5–7): 859-861.
- [63] Schapery RA. Thermal Expansion Coefficients of Composite Materials Based on Energy Principles. *Journal of Composite Materials* 1968, **2**(3): 380-404.
- [64] Hashin Z, Shtrikman S. A variational approach to the theory of the elastic behaviour of polycrystals. *Journal of the Mechanics and Physics of Solids* 1962, **10**(4): 343-352.
- [65] Kerner EH. The elastic and thermo-elastic properties of composite media. *Proceedings of the physical society Section B* 1956, **69**(8).
- [66] Smekal A. Zur Quantentheorie der Dispersion. *Naturwissenschaften* 1923, **11**(43): 873-875.
- [67] Raman CV. A new radiation. *Indian Journal of physics* 1928, **2**: 387-398.
- [68] Eine neue Erscheinung bei der Lichtzerstreuung in Krystallen. *Naturwissenschaften* 1928, **16**(28): 557-558.
- [69] Cardona M. Introduction. *Light Scattering in Solids I*. Springer Berlin Heidelberg, 1983, pp 1-22.
- [70] Dresselhaus MS, Dresselhaus G. Light scattering in graphite intercalation compounds. In: Cardona M, Güntherodt G (eds). *Light Scattering in Solids III*, vol. 51. Springer Berlin Heidelberg, 1982, pp 3-57.
- [71] Reich S, Thomsen C. Raman spectroscopy of graphite. *Phil Trans R Soc Lond A* 2004, **362**(1824): 2271-2288.
- [72] Tuinstra F, Koenig JL. Raman Spectrum of Graphite. *The Journal of Chemical Physics* 1970, **53**(3): 1126-1130.
- [73] Nemanich RJ, Solin SA. First- and second-order Raman scattering from finite-size crystals of graphite. *Physical Review B* 1979, **20**(2): 392-401.
- [74] Cardona M. Resonance phenomena. In: Cardona PDM, Güntherodt PDG (eds). *Light Scattering in Solids II*. Springer Berlin Heidelberg, 1982, pp 19-178.
- [75] Hart TR, Aggarwal RL, Lax B. Temperature Dependence of Raman Scattering in Silicon. *Physical Review B* 1970, **1**(2): 638-642.
- [76] Balkanski M, Wallis RF, Haro E. Anharmonic effects in light scattering due to optical phonons in silicon. *Physical Review B* 1983, **28**(4): 1928-1934.
- [77] Anastassakis E, Pinczuk A, Burstein E, Pollak FH, Cardona M. Effect of static uniaxial stress on the Raman spectrum of silicon. *Solid State Communications* 1970, **8**(2): 133-138.
- [78] Cerdeira F, Buchenauer CJ, Pollak FH, Cardona M. Stress-Induced Shifts of First-Order Raman Frequencies of Diamond- and Zinc-Blende-Type Semiconductors. *Physical Review B* 1972, **5**(2): 580-593.
- [79] Wolf ID. Micro-Raman spectroscopy to study local mechanical stress in silicon integrated circuits. *Semicond Sci Technol* 1996, **11**(2).
- [80] Loudon R. The Raman effect in crystals. *Advances in Physics* 1964, **13**(52): 423-482.
- [81] Anastassakis E, Cantarero A, Cardona M. Piezo-Raman measurements and anharmonic parameters in silicon and diamond. *Physical Review B* 1990, **41**(11): 7529-7535.
- [82] Anastassakis E, Siakavellas M. Elastic properties of textured diamond and silicon. *Journal of Applied Physics* 2001, **90**(1): 144-152.





microplatelets this ratio is lower with a value of 60. Therefore, microplatelets are expected to be more rigid towards deformation or bending.

**Table 3.1** Platelet shaped graphite particles used as reinforcement in metal/graphite composites

Supplier	Name	Lateral size [μm]	Thickness [nm]
XG Sciences Inc.	M5	5	20
XG Sciences Inc.	M25	25	20
TIMCAL Inc. C-Therm	T80	80	50
Graphene Laboratories Inc.	G300	300	5000

## 3.2 Composite fabrication

The preparation of the composites was carried out in two main steps. To homogenize the Cu/Gr powder mixture high energy ball milling was used to obtain powder mixtures containing 2 to 50 vol% of graphite platelets. The procedure was carried out using a planetary ball mill (Fritsch, PULVERISETTE 6, see Figure 3.1) with a 250 ml milling jar filled with 50 grinding balls, both made of zirconia ( $ZrO_2$ ). The process parameters were varied between 250 and 400 rpm for the rotation speed of the milling jar, while the total milling time was set to 1 to 3 hours. Such high rotation speed heats up the powder mixture as well as the milling jar. Therefore, the process was paused for 30 min after every 30 min of ball milling to let the system cool down. The temperature of the jar was meanwhile checked using an infrared thermometer (Votcraft IR800-20D). Since the milling process was carried out under ambient conditions, to high temperatures could have resulted in oxidation of the copper particles, which would eventually decrease the thermal conductivity of the composite. For a single milling run the volume of the powder mixture was held above 30 ml.

In the second step, the as-prepared Cu/Gr powder mixture was consolidated with spark plasma sintering (SPS) also known as field assisted sintering technique [1,2]. This is a technique that involves both, high pressure and high temperature. However, the main



**Figure 3.1** Picture of the planetary ball mill with opened lid containing the milling jar.



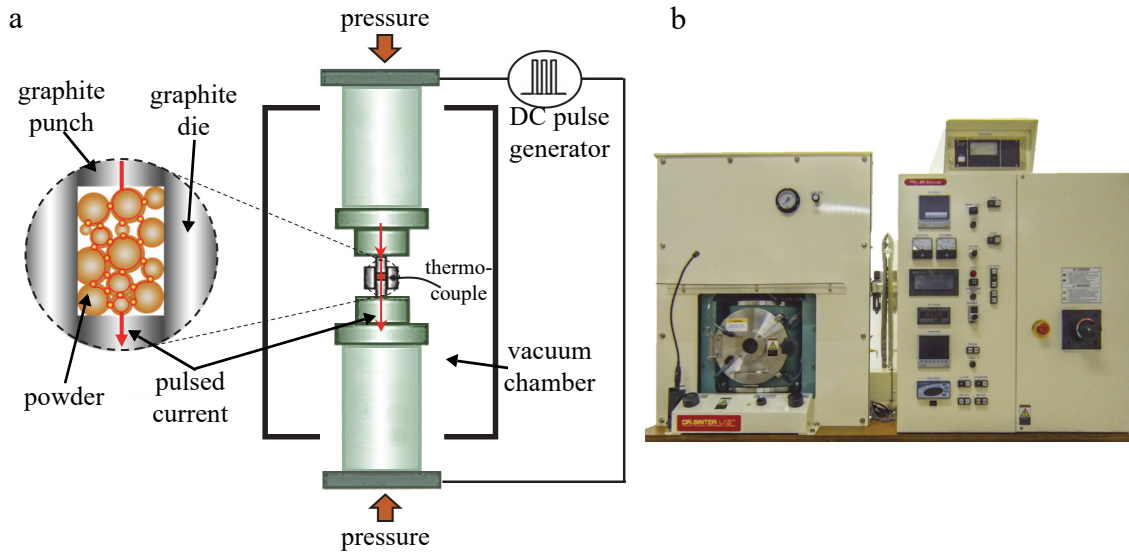


**Figure 3.2** (a) Scheme of the SPS process and (b) photograph of the SPS apparatus with the sintering chamber on the left and the pulse generator with the sintering controller on the right.

difference between SPS and other sintering techniques of the same family (e.g., hot isostatic pressing) is that the heat for the sintering process is generated by a pulsed DC current. This current is passing directly through the pressing die as well as the compacted powder. The scheme of the SPS setup is shown in Figure 3.2a. The biggest advantage of this internal heating is the fact that the heating as well as the cooling rate is very high and may reach 1000 K/min, while full densification is obtained at much lower temperatures, usually far below the melting point. This prevents phase separation due to melting and allows sintering of powders that contain components with different densities. The fast processing and the lower temperatures restrains grain growth or coarsening. This makes the technique applicable to densify nanopowders, while maintaining the nanostructure in the sintered solid [3]. In this study a Dr. Sinter Lab Jr. 211Lx SPS apparatus (Fuji Electronic Industrial Co.) was used, as shown in Figure 3.2b. For a sinter process the homogenized powder was placed into the cylindric graphite die with 6, 15 or 25 mm diameter. The graphite punches were coated with a thin layer of boron nitride spay (EKamold EP, ESK Ceramics GmbH & Co. KG) to prevent adhesion between punch and sintered specimen. After that the die-punch-powder assembly was placed into the vacuum chamber. A thermocouple was placed into a small pinhole of the graphite die to read out the temperature of the specimen, which controls the pulsed DC current. After reaching a vacuum pressure below 5 Pa the powder was precompact with a pressure of 40 to 50 MPa, which is maintained during the remainder of the process. The sintering temperature of 600 and 700°C for Cu/Gr composites and pure Cu, was reached with a heating rate of 50 K/min. After a dwell time of 5 min at the sintering temperature the current was switched off and the specimen cooled down to room temperature. The temperature profile for the consolidation of Cu is shown in Figure 3.3a. The optimal sintering temperature was found by

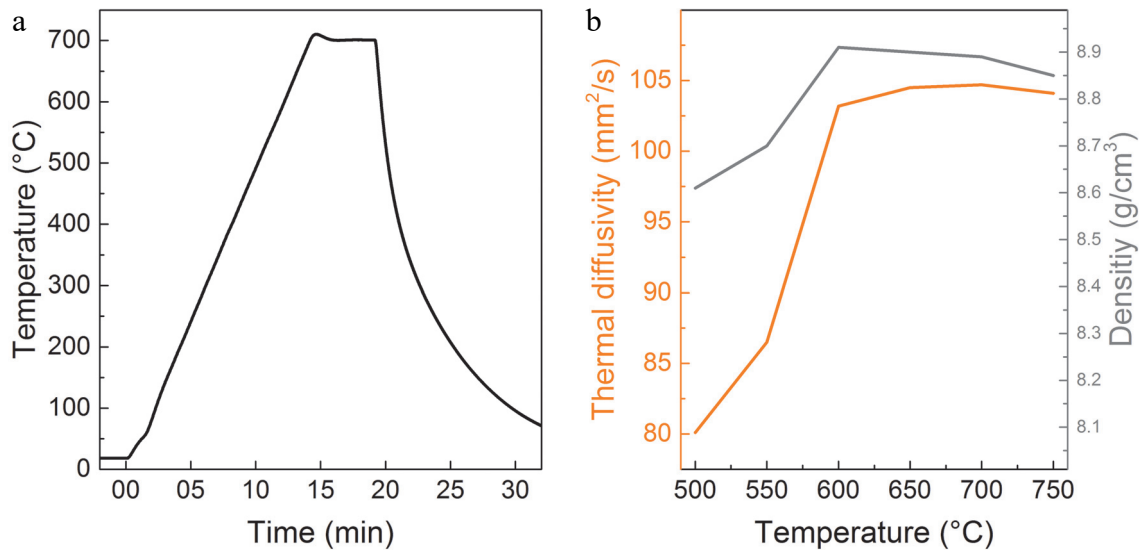


**Figure 3.3** (a) Typical temperature profile for the SPS process of Cu. (b) Thermal diffusivity (orange line, left scale) and density (gray line, right scale) of Cu for different sintering temperatures.

maximizing both the thermal diffusivity as well as the density of the sample. Figure 3.3b shows a plot of thermal diffusivity and density of Cu sintered at different temperatures. The thermal diffusivity strongly increases from a sintering temperature of 500 to 600°C. Between 600 and 700°C the thermal diffusivity increases further and reaches a maximum before slightly decreasing towards 750°C. Likewise the density strongly increases until 600°C where it reaches a maximum. With further increase of the sintering temperature the density drops only slightly. The best combination of high thermal diffusivity and high density was found at 700°C. For the Cu/Gr composites the optimal temperature was found at 600°C.

After the specimen is removed from the graphite die the surfaces are polished to remove remainders of the boron nitride coating. The entire sintering process takes less than 30 min. The consolidation of graphite nanoplatelet composites was done for graphite concentrations of 2, 5, 8, 20, and 26 vol%. Higher graphite concentrations lead to mechanically unstable specimen. For the micropatelet composites the higher graphite concentrations could be achieved by SPS. Cu/GmP powder mixtures with 8, 20, 40 and 50 vol% of graphite could successfully be consolidated to mechanically stable specimen.

### 3.3 Thermal diffusivity measurements

The thermal diffusivity was determined as described in Section 2.3.1 using the LFA447 Nano-Flash (Netzsch) apparatus, schematically displayed in Figure 3.4a. The sample is exposed to a Xenon flash lamp pulse of durations between 0.06 to 0.31 ms with a pulse energy of up to 10 J. The temperature rise on the opposing surface was recorded by a InSb

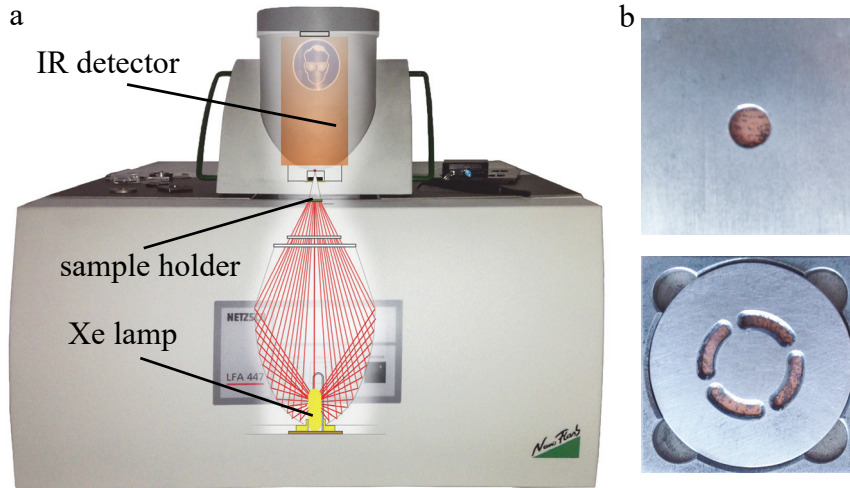


**Figure 3.4** (a) Photograph of the LFA447 NanoFlash with schematic representation of the setup and (b) photographs of the sample holder for in-plane diffusivity measurements containing an uncoated Cu/Gr sample with the side facing the flash lamp (top) and the side facing the IR detector (bottom).

infrared detector that is cooled with liquid nitrogen. To ensure equal light absorption and emission for all measured samples the surfaces were coated with a thin layer (1 to 3  $\mu\text{m}$ ) of graphite (Graphit 33, CRC Kontakt Chemie). The through-plane thermal diffusivity measurements were carried out on cylindrical samples with a diameter of 15 and 25 mm with typical thickness of 1 mm, but also up to 10 mm. For the in-plane thermal diffusivity measurements a special sample holder was used (see Figure 3.4b and Figure 2.4), where samples with a diameter of 25 mm are required.

A graphite sample (POCO Graphite AXM 5Q) was used as a reference material for specific heat calibration following Equation 2.24. The density of the samples was determined by Archimedes' principle by measuring the weight in air and in deionized water using a special holder for the balance resulting in

$$\rho = \frac{\rho_{H_2O}}{1 - \frac{m_{H_2O}}{m_{air}}}, \quad (\text{Eq. 3.1})$$

where  $\rho_{H_2O}$  is the density of water,  $m_{air}$  is the weight of the sample in air, and  $m_{H_2O}$  is the corresponding weight in water. The thermal conductivity  $k$  is then obtained from

$$k = ac_p\rho, \quad (\text{Eq. 3.2})$$

following Equation 2.3 for the in-plane and through-plane direction using the corresponding thermal diffusivity.

### 3.4 Thermal expansion measurements

The thermal expansion was measured on cylindrical samples with a diameter of 6 mm and a length of 1 to 6 mm on the horizontal dilatometer L75XH1000 (Linseis), as shown in Figure 3.5. During a measurement a quartz piston is pushing on the specimen with a constant force, while the temperature is changed at a constant rate. The resulting length change of the specimen is transferred via the piston to the linear variable differential transformer, which records the displacement. Measurements were performed under ambient conditions between 25 and 150°C with constant heating rates of 1 and 2 K/min. For each sample the temperature was cycled at least five times to ensure reproducibility and optimal contact between specimen and quartz piston. To acquire the CTE parallel as well as perpendicular to the rotation symmetry axis of the cylindrical sample the round side-walls were polished flat to obtain two additional parallel surfaces. The displacement/time curves were calibrated using empty dilatometer measurements following

$$\Delta L_{corr} = \Delta L_{sample} - \Delta L_{empty}, \quad (\text{Eq. 3.3})$$

where  $\Delta L_{corr}$  is the corrected displacement of the sample measurement,  $\Delta L_{sample}$  is the uncalibrated sample measurement and  $\Delta L_{empty}$  is the displacement measured with empty sample holder. As a control the measurements were also calibrated using a 20 mm long  $\text{Al}_2\text{O}_3$  reference sample.

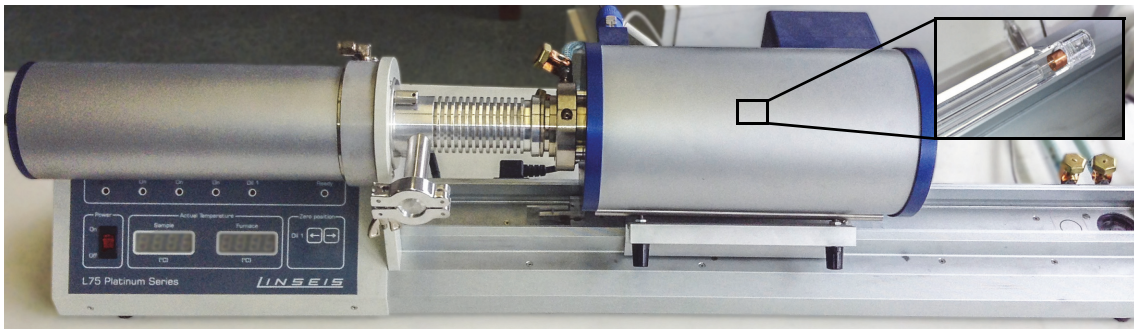


**Figure 3.5** Photograph of the dilatometer L75XH1000. The inset shows the sample holder with a Cu sample, the quartz piston, and the thermocouple.

### 3.5 Structural characterization

The morphology of the graphite platelets as well as the powder mixtures and the consolidated composites was investigated using a scanning electron microscope (SEM Hitachi SU-8030). The respective powders and consolidated composites were glued to a SEM stage with a conductive carbon based adhesive (CCC Carbon Adhesive).

Atomic force microscopy was used to obtain information about the thickness of the graphite nanoplatelets on a Park AFM (Schaefer Technologie GmbH) operated in non-contact mode. The samples were prepared by dispersing the powders in ethanol and then spin coated on a silicon wafer.

### 3.6 Raman spectroscopy

#### Graphite orientation

The polarization-dependent Raman spectroscopy was performed on the cross section of the fractured specimen. The excitation was done by a green laser with a wavelength of 532 nm and a power of 1 mW to avoid laser heating. The polarization of the incoming as well as the backscattered light was chosen parallel to each other and was focused using a 10× objective. A  $\lambda/2$  wave plate was used to rotate the angle between the polarization direction and the sample normal. The spectra were recorded by a Horiba T64000 triple monochromator (see also Figure 4.7a in Section 4.2).

#### Strain in silicon

The temperature dependent Raman spectra of silicon were obtained with a micro-Raman spectrometer in backscattering geometry having an excitation wavelength of 532 nm and a spectral resolution of  $0.05 \text{ cm}^{-1}$ . The temperature of the 100  $\mu\text{m}$  thick silicon wafer (5×5 mm) was varied using a cooling/heating stage (THMS600 Linkam Scientific) under nitrogen atmosphere at temperatures of 83 to 300 K. Silicon pieces of similar size were attached with epoxy glue (UHU Plus endfest 300) to blocks made of aluminum, copper and a copper composite containing 50 vol% of G300 and cured over night at room temperature to avoid residual stress in the silicon substrate (see also Figure 4.23 in Section 4.5). The samples were cooled down to 83 K and subsequently heated to 298 K with a heating rate of 10 K/min and with Raman spectra taken every 5 K.

### **3.7 LED heat sink setup and thermographic images**

Light emitting diodes (3 W, white, WTN-3W-190kw) were mounted on heat sinks made of copper and a copper composite containing 50 vol% of G300 with a thermally conductive silver-based adhesive (Pyro-Duct 597-A). Additionally, each LED-heat sink assembly was attached to an aluminum block. The power consumption of the LEDs was measured separately to ensure that both diodes generate the same amount of heat. The temperature of the LEDs as well as the heat sinks was monitored with an infrared camera. To provide reliable thermal image interpretation, an adhesive emission tape, with defined emission factor of 0.95, was attached to the surface of the heat sinks. (see also Figure 4.27a in Section 4.6)

---

## References

- [1] Saheb N, Iqbal Z, Khalil A, Hakeem AS, Al Aqeeli N, Laoui T, *et al.* Spark Plasma Sintering of Metals and Metal Matrix Nanocomposites: A Review. *Journal of Nanomaterials* 2012, **2012**.
- [2] Orrù R, Licheri R, Locci AM, Cincotti A, Cao G. Consolidation/synthesis of materials by electric current activated/assisted sintering. *Materials Science and Engineering: R: Reports* 2009, **63**(4–6): 127-287.
- [3] Olevsky EA, Kandukuri S, Froyen L. Consolidation enhancement in spark-plasma sintering: Impact of high heating rates. *Journal of Applied Physics* 2007, **102**(11): 114913







## 4.1 Structure and morphology

### 4.1.1 Copper powder and graphite platelets

The as received materials were investigated by scanning electron microscopy (SEM) to reveal the morphology as well as the size of the composite components. As a source for the copper matrix in the composites, copper powder with an average particle size of  $3\ \mu\text{m}$  was chosen, which is up to 2 orders of magnitude smaller than the lateral size of the graphite platelets. A representative scanning electron microscope image of the as received powder is displayed in Figure 4.1.

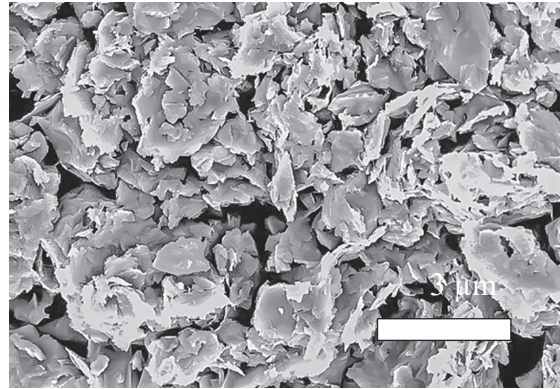


**Figure 4.1** SEM image of as received copper powder.

Figure 4.2 shows the SEM images of the graphite nanoplatelets as well as the graphite microplatelets with different magnifications. For the M5 and M25 powders the platelets

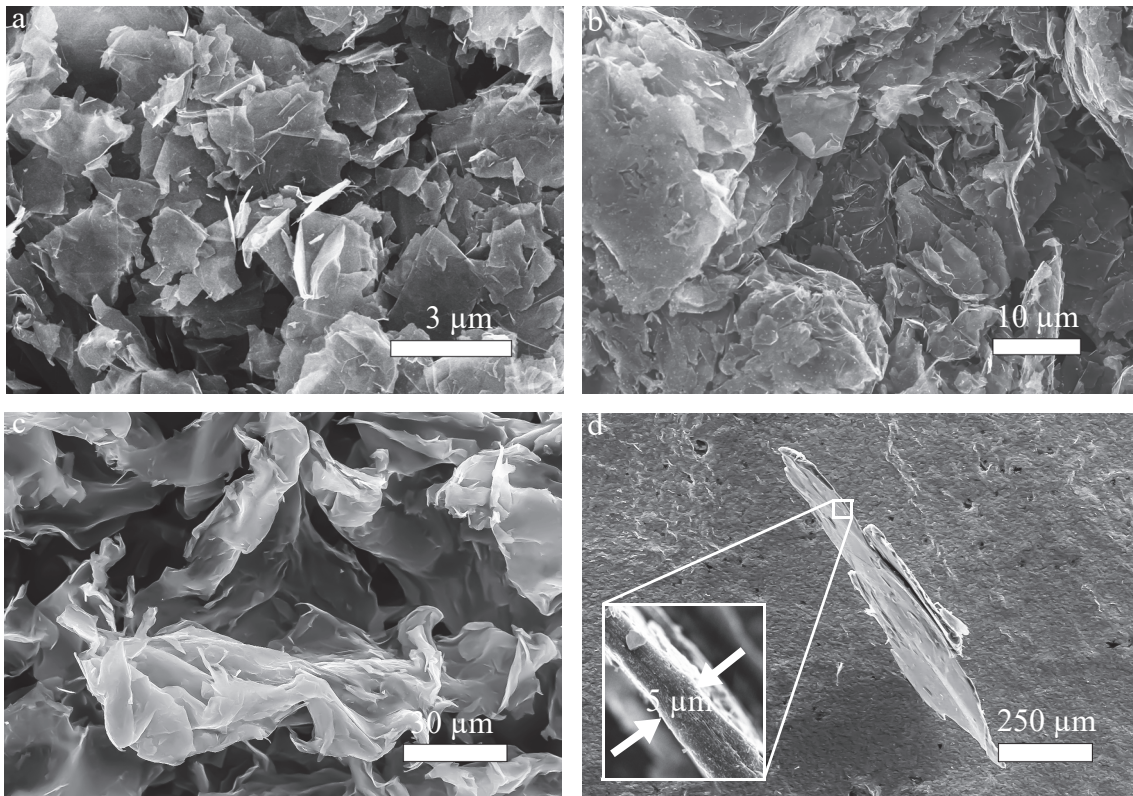


**Figure 4.2** SEM images of as received (a) M5, (b) M25, and (c) T80 graphite powders. (d) Free standing G300 platelet with the inset showing the thickness of a G300 platelet.

have a very similar structure with the only difference being the average lateral size of the platelets. The T80 GnPs have an average lateral size of 80  $\mu\text{m}$  and appear to be less rigid and more wavy than the M5 and M25 platelets. Compared to the GnPs the G300 microplatelets exhibit the largest average lateral size of 300  $\mu\text{m}$ . In contrast to the nanoscale thickness of the M5, M25, and T80 platelets, verified by atomic force microscopy, the G300 GmPs have a microscale thickness of about 5  $\mu\text{m}$  shown in the inset of Figure 4.2d (see also Table 3.1).

#### 4.1.2 Consolidated materials

As mentioned in Section 3.2 using spark plasma sintering as the consolidation technique one is able to obtain (i) high densification at low temperatures, i.e., significantly below the melting point, (ii) in a short time frame. Figure 4.3a shows the densities of the pure Cu samples as well as the Cu/Gr composites. The values are highly reproducible for all graphite platelet types over the entire concentration range and are very close to the expected density obtained by rule of mixture (dashed line). In fact, the densities are usually within 98% of full densification, confirming that SPS is an effective technique to achieve high densities at low temperatures in a fast process. The composites are mechanically stable and could be polished and processed to any shape needed. It was necessary to produce samples with different shapes and sizes for the different measurement tech-

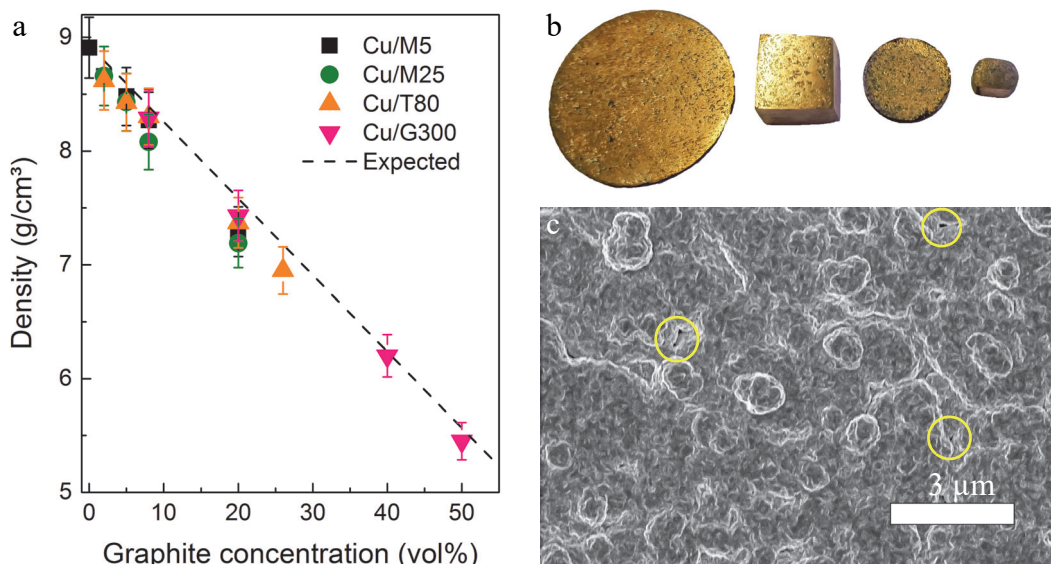


**Figure 4.3** (a) Plot of the density of the Cu/Gr composites in dependence of the graphite concentration in comparison with the expected density obtained by rule of mixture (dashed line) (b) Photograph of typical composite samples for different experiments. The size of the images corresponds to the actual size of the samples. (c) SEM image of consolidated copper. The yellow circles indicate porosity in the material.

niques, e.g., diffusivity, expansion, and Raman measurements. Figure 4.3b exemplary displays composites with different shapes and sizes used in the experiments in this study. To confirm the low degree of porosity in the consolidated samples a pure Cu sample was investigated with SEM shown in Figure 4.3c. Only very few pores are visible indicated by the yellow circles in the image.

The fractured cross-sections of the consolidated Cu/Gr composites were investigated with SEM for the different platelet reinforcements. Figure 4.4 presents images of the fractured cross-sections of Cu/GnP composites for different magnifications. Compared to the isotropic structure of the pure Cu samples the composites look remarkably different. Inter-

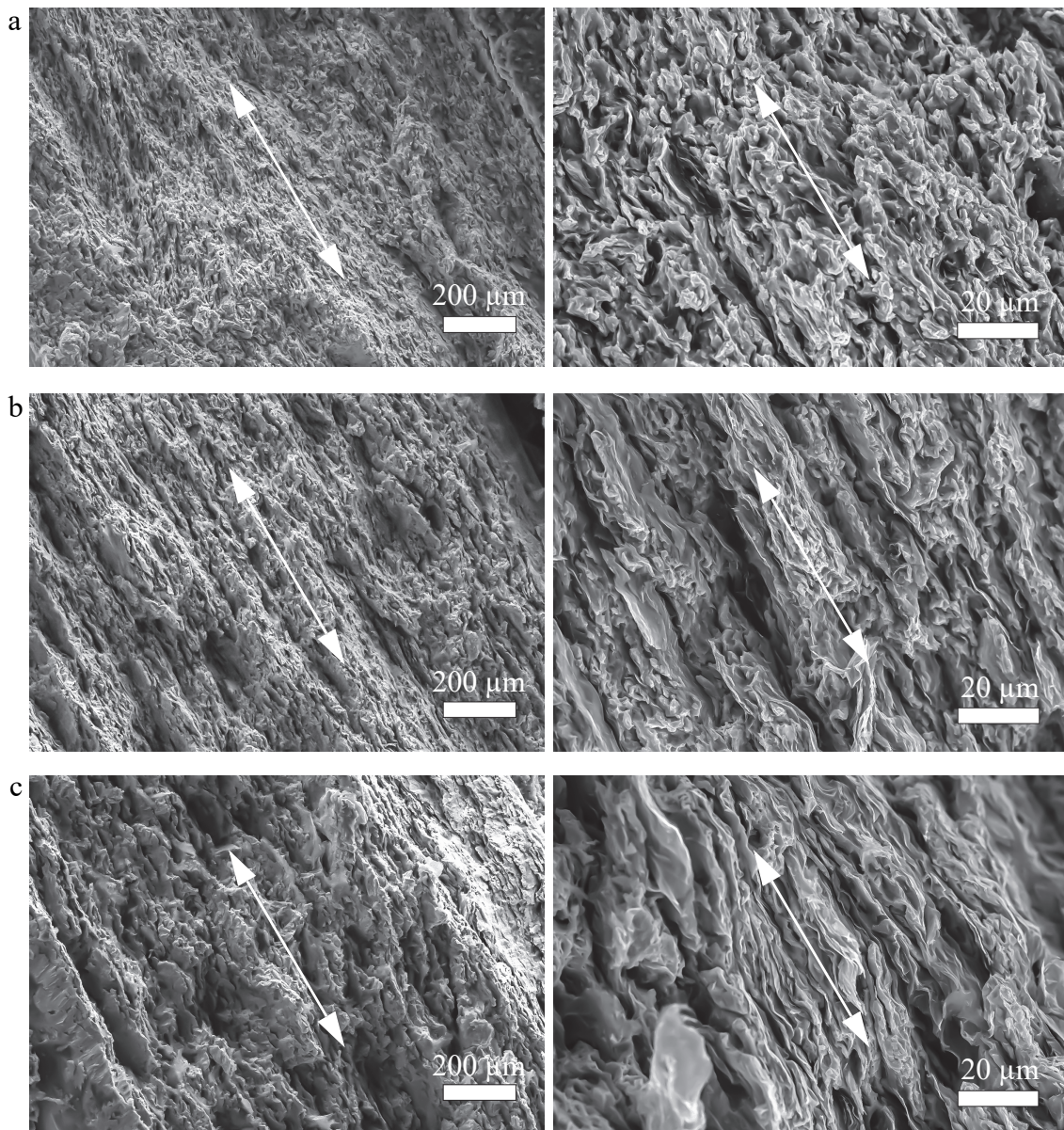


**Figure 4.4** SEM images with low (left column) and high (right column) magnification of consolidated copper/GnP composites containing (a) M5 platelets, (b) M25 platelets, and (c) T80 platelets. The white arrows indicate the direction of the preferred platelet alignment, which is perpendicular to the direction of the applied force during SPS.

estingly, the platelets align along a preferred direction within the Cu matrix indicated by the white arrows in Figure 4.4. This direction is perpendicular to the direction of the applied force during spark plasma sintering. Moreover, the layered structure is more apparent in composites with larger graphite platelets, i.e., an increased difference between the size of the Cu particles and graphite platelets. This could indicate a higher degree of platelet alignment.

For Cu/GmP composites the platelet alignment is expected to be most prominent, since the lateral size of the platelets is yet one order of magnitude higher. Figure 4.5 shows the SEM image of the aligned graphite microplatelets. The platelets are evenly distributed within the Cu matrix. Moreover, the order of the layered structure is significantly increased compared to the Cu/GnP composites, displayed in Figure 4.4. Thus, the observed structural anisotropy is

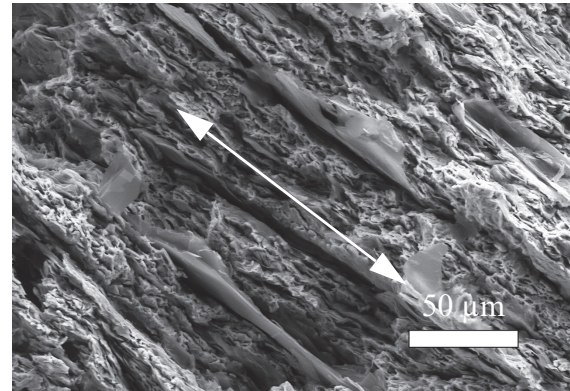


**Figure 4.5** SEM image of the fractured cross-section of a consolidated copper/G300 sample. The white arrow indicates the direction of preferred alignment.

expected to translate to anisotropic thermal properties of the composites. The degree of alignment will be quantized by polarization-dependent Raman spectroscopy in the next section.

To maintain the excellent thermal conductivity of the graphite platelets care has to be taken not to increase the number of defects in the carbon lattice. A Raman spectrum of the graphite particles was taken after each step of the production process to compare the intensity ratios between the D and the G peak to the ratio of the as received material. In Figure 4.6 the respective Raman spectra for T80 GnPs and G300 GmPs are shown. The D/G intensity ratio for the as received T80 platelets is 0.16 and increases to 0.31 after ball milling. The SPS process does not increase the ratio. For the as received G300 GmPs the D/G ratio is 0.21 which increased to 0.27 by ball milling. After SPS the value remains constant (0.28). The increase of the D peak caused by ball milling indicates the additional introduction of defects to the carbon lattice as well as a decreased crystalline size of the graphite platelets [3-5]. However, the increase is not significant. The influence of the sintering process on the crystalline structure of the graphite platelets is negligible. Therefore, it can be assumed that the platelets excellent thermal properties are maintained within the composite material.

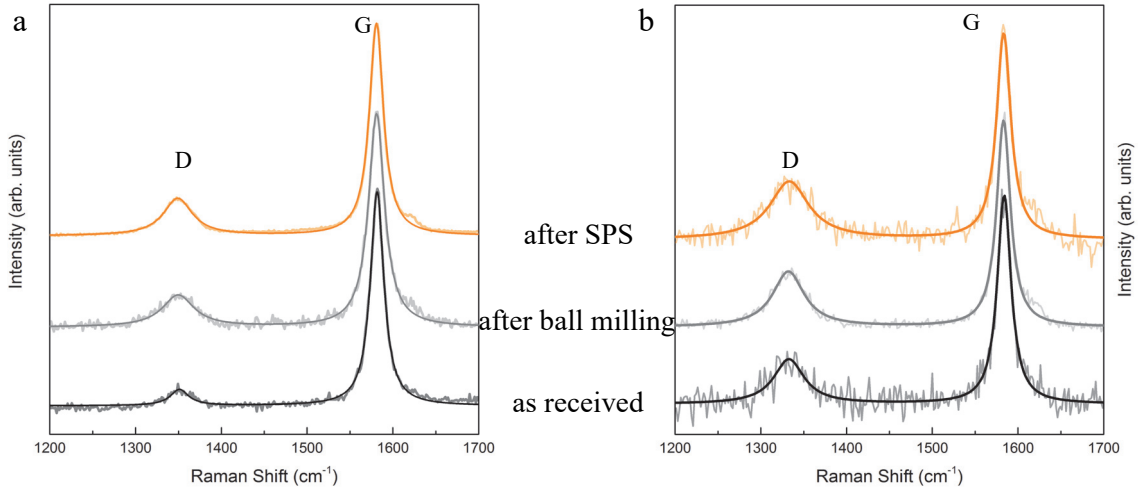


**Figure 4.6** Raman spectrum of (a) T80 GnPs and (b) G300 GmPs. The spectra taken before (black line) and after ball milling (gray line) as well as after spark plasma sintering (orange line) were normalized to the G peak intensity and shifted for clarity.

## 4.2 Quantification of graphite alignment

As shown in Section 2.5.2 the relative Raman intensity of the G line are calculated from the polarization of the incoming and the scattered light, see Equation 2.50. Assuming that the graphite basal planes are oriented along the  $x$ - $y$  plane the intensity was calculated for a single graphite crystal for two different polarization scenarios. Without loss of generality, any orientation of the graphite basal plane is possible in a composite material. There are several possibilities to extend Equation 2.50 to cases when the graphite basal plane is rotated away from the  $x$ - $y$  plane. One way is to transform the Raman tensors of the  $E_{2g}$  phonon by applying the rotation matrices

$$\Gamma_x(\gamma_x) = \begin{bmatrix} 1 & 0 & 0 \\ 0 & \cos\gamma_x & -\sin\gamma_x \\ 0 & \sin\gamma_x & \cos\gamma_x \end{bmatrix} \text{ and } \Gamma_y(\gamma_y) = \begin{bmatrix} \cos\gamma_y & 0 & \sin\gamma_y \\ 0 & 1 & 0 \\ -\sin\gamma_y & 0 & \cos\gamma_y \end{bmatrix}, \quad (\text{Eq. 4.1})$$

where  $\gamma_x$  and  $\gamma_y$  cause a rotation about the  $x$  and  $y$  axis, respectively. Only the rotation about these two angles are necessary to obtain any possible basal plane orientation. The Raman intensity of a rotated graphite crystal is modified to

$$I(\varphi, \gamma_x, \gamma_y) \propto \left| e_{in} \cdot \Gamma_x^\dagger \cdot \Gamma_y^\dagger \cdot \mathbf{R}_1 \cdot \Gamma_y \cdot \Gamma_x \cdot e_{sc} \right|^2 + \left| e_{in} \cdot \Gamma_x^\dagger \cdot \Gamma_y^\dagger \cdot \mathbf{R}_2 \cdot \Gamma_y \cdot \Gamma_x \cdot e_{sc} \right|^2. \quad (\text{Eq. 4.2})$$

The rotation about the  $z$  axis is invariant due to the symmetry of the system. An example for the intensity distribution after a rotation by  $60^\circ$  about the  $x$  axis was shown in Figure 2.7b for a polarization change in the  $x$ - $z$  plane.

The relation between orientation of the graphite basal plane and the polarization-dependent Raman intensity of the G line are used to determine the orientation distribution of graphite particles that are embedded in a composite material. It is apparent that for random distribution of graphite particles the intensity will be constant for all possible polarization vectors. For fully aligned particles, i.e., the basal planes are parallel to each other, the Raman intensity is expected to be described by Equation 2.54 if the polarization is changed perpendicular to the alignment. Any orientation distribution of the basal planes may be described by a distribution function  $g(\gamma)$  for the rotation angles  $\gamma_x$  and  $\gamma_y$ . The overall Raman intensity is then obtained by integrating over all possible basal plane orientations resulting in

$$I_{tot}(\varphi) \propto \iint g(\gamma_x)g(\gamma_y)I(\varphi, \gamma_x, \gamma_y)d\gamma_x d\gamma_y, \quad (\text{Eq. 4.3})$$

where  $I(\varphi, \gamma_x, \gamma_y)$  is given by Equation 4.2. This relation allows to determine the orientation distribution of graphite particles that are embedded in a composite material. In the case of the Cu/Gr composite materials the platelets are distributed along a preferred direction due to the uniaxial pressing force applied in the SPS process. Therefore,  $g(\gamma)$  chosen to a normal distribution given by

$$g(\gamma, \sigma_G) = \frac{1}{\sigma_G \sqrt{2\pi}} \exp\left(-\frac{\gamma^2}{2\sigma_G^2}\right), \quad (\text{Eq. 4.4})$$

where  $\sigma_G$  is the standard deviation of the angle distribution. Thus, the overall Raman intensity of the G line depends on the angle of the polarization vector  $\varphi$  and the standard deviation  $\sigma_G$ . The polarization-dependent Raman intensity is measured in a setup presented in Figure 4.7a where the polarization of the incoming and the scattered light is changed in the  $x$ - $z$  plane (see also Equation 2.53) and the samples are oriented in the  $x$ - $y$  plane. To calibrate the Raman intensity of the composite materials highly oriented pyrolytic graphite (HOPG) was measured in the same microscope. The SEM image of HOPG presented in Figure 4.7b shows fully aligned graphite basal planes which were aligned in the  $x$ - $y$  plane in the Raman setup. For perfect measurement conditions the intensity of the HOPG G mode is expected to follow  $I_{HOPG}(\varphi) \propto f^2 \cos^4 \varphi$ . However, there are several factors that influence the measurement such as the imperfect polarizers or the finite collection angle of the  $10\times$  objective used in the setup. Therefore, the intensity is expected to be nonzero for a polarization angle of  $90^\circ$  and  $270^\circ$  as opposed to the theoretically expected trend shown in Figure 2.7b (red curve). This was confirmed by the measured intensity plotted in Figure 4.7c. For the forbidden polarization direction the

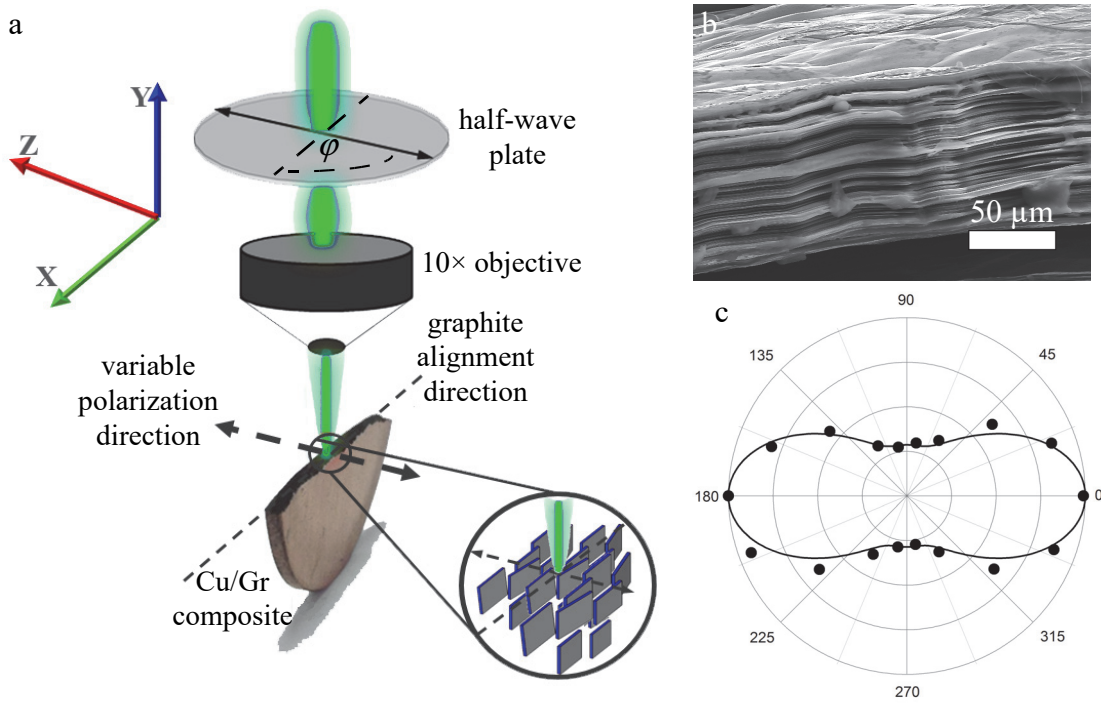


**Figure 4.7** (a) Setup of the polarization-dependent Raman spectroscopy. (b) SEM image of highly oriented pyrolytic graphite. (c) Polar plot of the G peak intensity of HOPG in dependence over the polarization angle. The measured data represented by the black symbols are fitted to Equation 4.5 represented by the black line.

intensity drops to 28% of the maximum intensity measured for a polarization angle of  $0^\circ$  and  $180^\circ$ . To correct the non-vanishing intensity the correction term  $I_0$  is added to the HOPG intensity as

$$I_{HOPG}(\varphi) \propto f^2 \cos^4 \varphi + I_0. \quad (\text{Eq. 4.5})$$

The correction from the HOPG measurement is then used for the composite measurement, which modifies Equation 4.3 to

$$I_{tot}(\varphi, \sigma_G) \propto \iint g(\gamma_x, \sigma_G) g(\gamma_y, \sigma_G) I(\varphi, \gamma_x, \gamma_y) d\gamma_x d\gamma_y + I_0, \quad (\text{Eq. 4.6})$$

with  $I_0$  taken from the calibration measurement (black curve in 4.7c). The angle  $\varphi$  is controlled during the experiment making  $\sigma_G$  the only fitting parameter for the polarization-dependent Raman intensity of the graphite containing composites.



## GnP composites

The polarization-dependent Raman measurements were performed on the fractured cross-section as illustrated in Figure 4.7a on M5, M25 and T80 composites for different filler concentrations. The intensities are plotted over the polarization angle in Figure 4.8 and fitted to Equation 4.6. Within the measurement accuracy the intensity was independent of the concentration of the platelets embedded in the copper matrix. As expected from the SEM observations in Section 4.1.2 the G peak intensity has a maximum when the polarization direction is chosen parallel to the observed direction of the preferred alignment, i.e., perpendicular to the force applied during SPS. An intensity minimum was observed for polarization angles of  $90^\circ$  and  $270^\circ$  where the intensity drops to 73% for M5, 65% for M25, and 54% for T80 composites, respectively. As expected from the analysis of the structure the Cu/T80 composites exhibit the best alignment confirming that larger lateral size of the platelets leads to better alignment. From the fit of the measured data to Equation 4.6 the respective standard deviations for the angle distribution of the alignment are obtained. The corresponding values (in radians) for  $\sigma_G$  are 0.70 (M5), 0.60 (M25), and 0.47 (T80), which corresponds to  $40^\circ$ ,  $34^\circ$ , and  $27^\circ$ , respectively. These findings will be used later for thermal enhancement calculations.

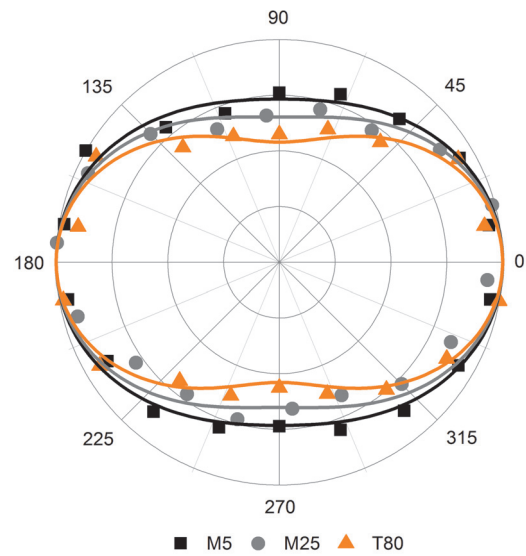


**Figure 4.8** Polar plot of the G peak intensity of composites containing different sized GnPs over the polarization angle  $\varphi$  (symbols) and the according fit to Equation 4.6 (solid lines). The intensity is independent of the platelet concentration and just depends on the lateral size of the platelet. The symbol size represents the measurement accuracy.

## GmP composites

In a similar fashion the polarization-dependent Raman intensity of the Cu/G300 composites were measured shown in Figure 4.9. In contrast to the GnP composites the intensity does depend on the concentration of the G300 platelets, at least for the lower volume fractions. However, it is worth to note that the concentration range was significantly larger for the microplatelet than for the nanoplatelet composites. Again, the intensity of the G mode in Figure 4.9 has a maximum when the polarization of the

incoming and the scattered light are chosen parallel to the direction of preferred alignment, i.e., for  $\varphi = 0^\circ, 180^\circ$ . The intensity drops at  $90^\circ$  and  $270^\circ$  and increases with increasing concentration from 71% of the maximum intensity for the 8 vol% composite to as low as 41% for 40 and 50 vol% filler concentration. The Raman analysis confirms that the order of the graphite basal planes and, therefore, the degree of alignment is the highest for Cu/G300 composites with high platelet concentration compared to all studied composite systems. Fitting the measured data to Equation 4.6 leads to  $\sigma_G$  of 0.69 for 8 vol%, 0.61 for 20 vol%, and 0.37 for 40 and 50 vol%.

The Raman analysis of the platelets alignment confirmed the structural observations quantitatively. With increasing lateral size of the platelets the order of the basal planes increased. Besides the size of the platelets, the uniform force applied during SPS is the second key factor for achieving this anisotropic structure, because the platelets are non-spherical with a high aspect ratio. Therefore, uniform load causes a rotation of the platelets to the direction normal to the load axis. This was observed before for extruded metal matrix composites reinforced by non-spherical particles [6,7]. Since graphite has strongly anisotropic thermal properties (see Section 2.1.2), this anisotropy is expected to transfer to the composite material leading to a direction-dependent thermal conductivity and expansion. Composites with the best alignment are expected to possess thermal properties with the highest anisotropy. Moreover, the alignment was quantized, providing a structural parameter for the modeling of the thermal properties by means of the effective medium approximation.

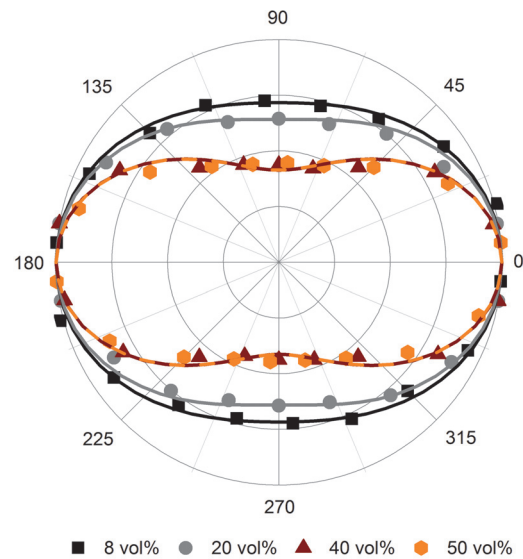


**Figure 4.9** Polar plot of the G peak intensity of composites containing G300 platelets with different filler fractions over the polarization angle  $\varphi$  (symbols) and the according fit to Equation 4.6 (solid lines). The symbol size represents the measurement accuracy.

### 4.3 Thermal transport in copper/graphite composites

The findings in the previous section revealed that there are two distinguished directions for the heat transport in the composite: (i) parallel to the platelet alignment referred to as in-plane direction (indicated by the arrows in Figure 4.4 and Figure 4.5) and (ii) perpendicular to the alignment referred to as through-plane direction, i.e., parallel to the applied

force during SPS. Therefore, the thermal transport properties of the Cu/Gr composites was investigated with respect to these directions. More specifically, the thermal diffusivity was determined by the light flash method as described in Sections 2.3.1 and 3.3. The through-plane thermal diffusivity  $a_{tp}$  was measured in the standard setup configuration (see also Figure 2.2), whereas, the in-plane diffusivity  $a_{ip}$  was determined using the modified setup (see also Figure 2.4). Two representative detector signals for the rear surface of the 50 vol% Cu/G300 composite are shown in Figure 4.10 for a through-plane and an in-plane measurement. The detector signals are amplified and corrected to obtain a flat baseline for the pre-shot signal ( $t < 0$ ). Next, the signal is fitted with regard to pulse

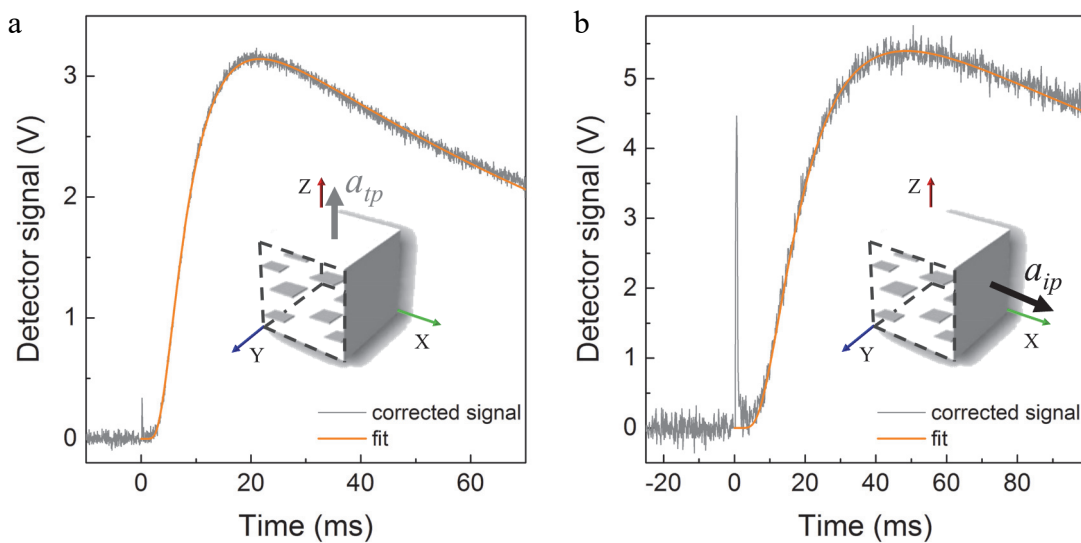


**Figure 4.10** Temperature profile of the rear surface of a Cu/G300 composite (50 vol%) measured by the IR-detector for (a) the through-plane and (b) the in-plane setup. The curves are corrected for possible temperature drift to obtain a flat baseline (i.e., for negative times). The schemes indicate the direction of the measurement with respect to the preferred platelet alignment.

correction and heat loss to extract the thermal diffusivity, as described in Section 2.3.1. The sharp peak at the time of the light pulse ( $t = 0$ ) is an electronic artifact from the power generator of the xenon flash lamp. By comparing the signal to noise ratio of the through-plane and in-plane measurements it becomes apparent that the noise is noticeably increased for the in-plane signal. This is a direct consequence of the much smaller surface area that is irradiated due to the mask between the flash lamp and the specimen (see also Figure 2.4).

### 4.3.1 Composites containing graphite nanoplatelets

The direction dependent thermal diffusivity is presented in Figure 4.11a. The measurements verified the anisotropic nature of the Cu/Gr composites. Over the entire concentration range the thermal diffusivity lies below the value of Cu ( $a_{\text{Cu}} = 105 \text{ mm}^2\text{s}^{-1}$ ). As expected, the through-plane diffusivity  $a_{\text{tp}}$  drops drastically with increasing graphite content, since graphite is not a good heat conductor perpendicular to the planes (see also Section 2.1.2). For all three GnP types the values are very similar. The in-plane thermal diffusivity  $a_{\text{ip}}$  decreases with increasing graphite concentration as well for M5 and M25 composites. However, the values remain well above the through-plane conductivity, a result of the high thermal conductivity of the platelets along the basal planes. In contrast,  $a_{\text{ip}}$  of the T80 composites remains constant at around  $97 \text{ mm}^2\text{s}^{-1}$  over the entire concentration range and lies just below pure copper. The anisotropy of the thermal diffusivity is the highest for Cu/T80 composites. Figure 4.11b shows the quasi linear dependence of that anisotropy defined as in-plane divided by through-plane thermal diffusivity ( $a_{\text{ip}} / a_{\text{tp}}$ ), which is equal to the anisotropy of the thermal conductivity. The linear dependence between graphite concentration and anisotropy is a direct result of the fact, that the alignment of the GnPs is independent of the concentration of the filler. The resulting thermal conductivity will be discussed in Section 4.3.3.

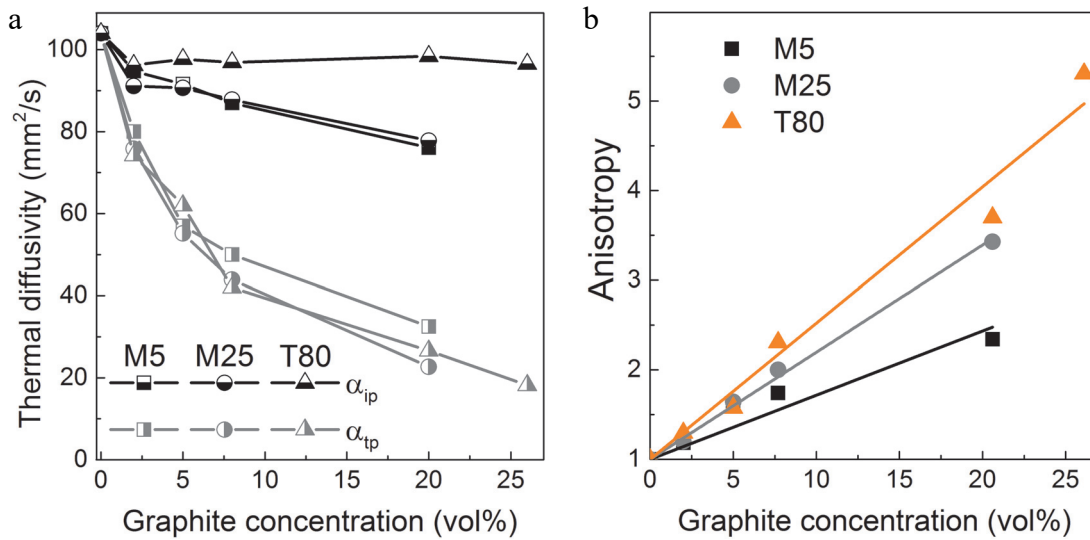


**Figure 4.11** (a) Thermal diffusivity of Cu/GnP composites in dependence of the graphite concentration for the in-plane as well as through-plane direction. The error of the measurement is smaller than the size of the symbols, i.e., below 5%. (b) Anisotropy of the thermal diffusivity for the Cu/GnP composites (symbols) with the corresponding linear fits (solid lines).

### 4.3.2 Composites containing graphite microplatelets

The composites containing G300 platelets are expected to have the highest anisotropy of thermal diffusivity since the platelets show the best alignment towards the in-plane direction. The measurements were carried out in similar fashion with the concentration dependent thermal diffusivities shown in Figure 4.12a for both respective directions. The through-plane diffusivity is lower than the diffusivity of copper. It decreases with increasing concentration, as observed for all Cu/Gr composites. The in-plane diffusivity follows a trend that was not observed before. For low graphite concentration  $a_{ip}$  still lies below the value of copper. However, with increasing G300 content the thermal diffusivity along the platelet alignment increases to a value that is twice as high as the thermal diffusivity of copper for 50 vol%. In contrast to the Cu/GnP composites, the concentration dependence of the anisotropy is not linear but follows a 2nd order polynomial, as shown in Figure 4.12b. This is a direct consequence of the concentration dependent platelet alignment described in Section 4.2. For a graphite concentration of 50 vol% the in-plane thermal diffusivity exceeds the through-plane value by a factor of 11, which makes the heat conduction perpendicular to the G300 alignment virtually negligible compared to the in-plane heat transport. In the following section the thermal conductivity as well as the influencing factors for the thermal conductivity enhancement will be discussed.

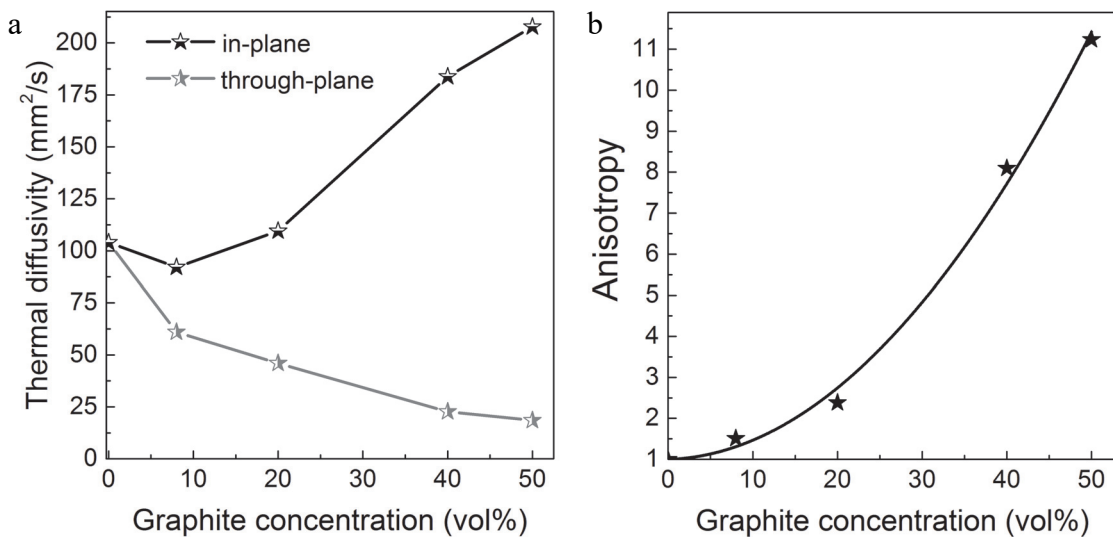


**Figure 4.12 (a)** Thermal diffusivity of Cu/300 composites in dependence of the graphite concentration for the in-plane as well as through-plane direction. The error of the measurement is smaller than the size of the symbols, i.e., below 5%. **(b)** Anisotropy of the thermal diffusivity for the Cu/G300 composites (symbols) fitted to a 2nd order polynomial (solid line).

The Cu/Gr composite materials have potential to be used as heat sinks for thermal management of electronic devices. The typical working temperature of such devices is from room temperature to approximately 150°C. The temperature dependence of the thermal diffusivity of the best performing Cu/G300 composite with 50 vol% graphite concentration was investigated, as shown in Figure 4.13. Within the studied temperature interval the thermal diffusivity decreases by about 25% for both, the through-plane and the in-plane direction. This trend is expected from the temperature dependence of the composite components. Namely, the thermal conductivity of graphite decreases from around 2000 Wm<sup>-1</sup>K<sup>-1</sup> at room temperature to around 1200 Wm<sup>-1</sup>K<sup>-1</sup> at 150°C [8]. The thermal conductivity of Cu decreases only by around 3% when the temperature is increased from room temperature to 150°C [8]. Nevertheless, with  $a_{ip}(140^\circ\text{C}) = 150 \text{ mm}^2\text{s}^{-1}$  the Cu/G300 composite is still outperforming pure copper by almost 50%.

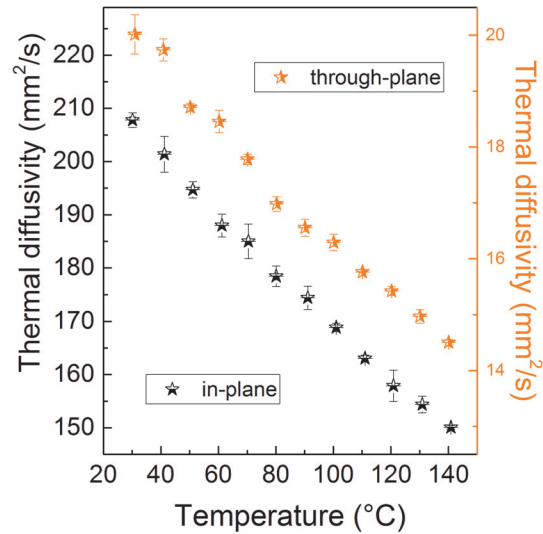


**Figure 4.13** Temperature dependence of the in-plane (black stars and black scale) and through-plane (orange stars and orange scale) thermal diffusivity of the 50 vol% Cu/G300 composite.

### 4.3.3 Effective medium approximation for copper/graphite composites

The thermal diffusivity of the Cu/Gr composites was used to calculate the thermal conductivity in the through-plane ( $k_{tp}$ ) and in-plane direction ( $k_{ip}$ ) following Equation 3.2. Since the measurement of the specific heat using the light flash method may only be applied to isotropic materials (see Section 2.3.1) the specific heat capacity of the Cu/Gr composites was obtained from ROM using the individual values for Cu [9] and Gr [10]. The density (see Figure 4.3) and the specific heat capacity are then multiplied with the thermal diffusivity. The symbols in Figure 4.14 show the values for the thermal conductivity in through-plane as well as in-plane direction for composites containing M5, M25, T80, and G300 in dependence of the graphite concentration. By adding graphite to the copper matrix the density decreased while the specific heat capacity increased. Therefore, the thermal conductivity is following the same trend as observed in Section 4.3 for the thermal diffusivity. For the Cu/GnP composites the thermal conductivity lies below the measured value of pure copper for the through-plane as well as the in-plane direction.

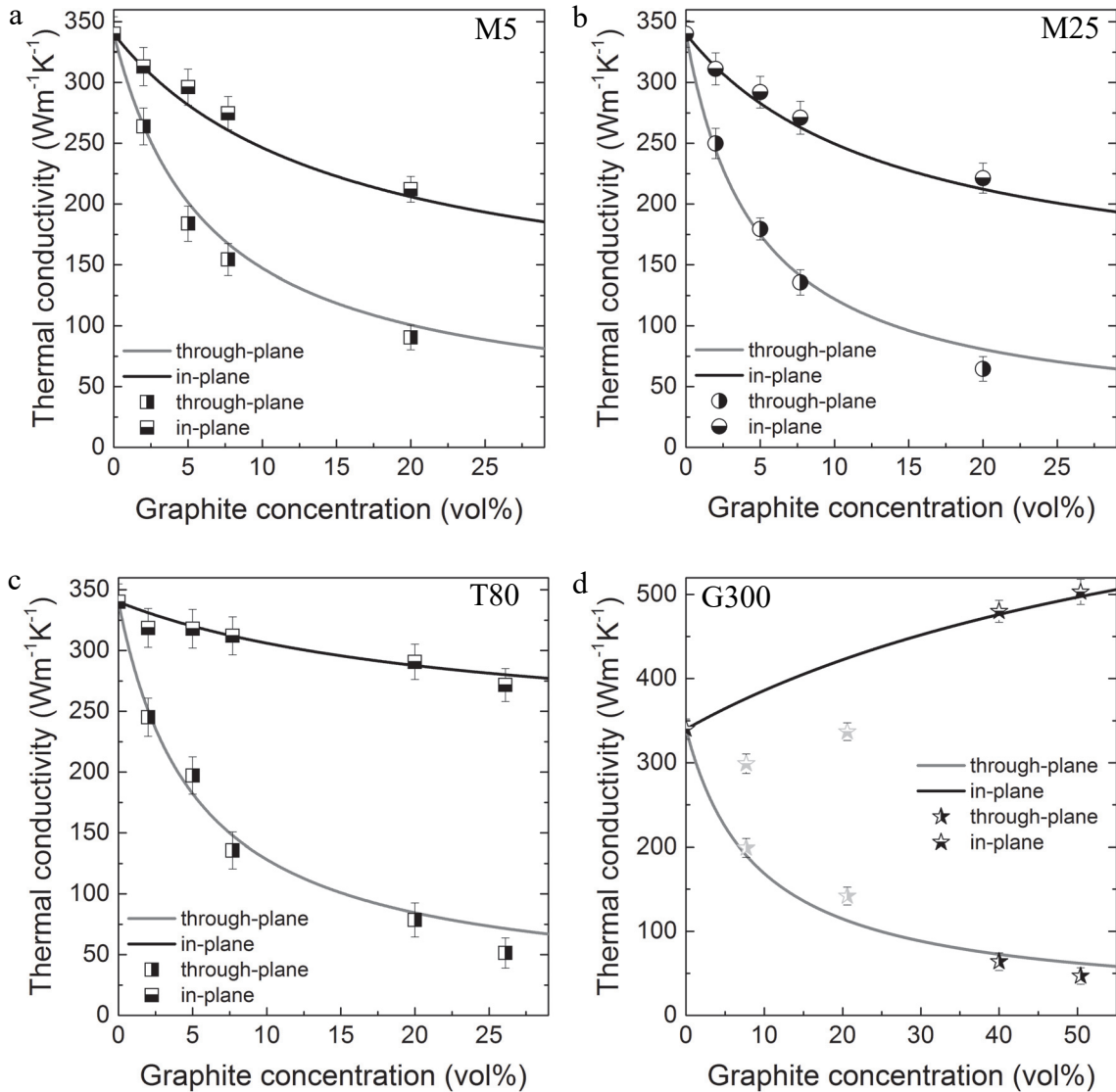


**Figure 4.14** In-plane and through-plane thermal conductivity in dependence of the graphite concentration for composites containing (a) M5, (b) M25, (c) T80, and (d) G300 platelets (symbols). The measured data are fitted to the EMA calculation using the Kapitza resistance as the fitting parameter (solid lines). The curves in (d) are calculated using the orientation factor for 40 and 50 vol%. Therefore, the values for 8 and 20 vol% are shaded in gray for clarity.

The in-plane thermal conductivity of the Cu/G300 composites is up to 50% higher than copper with a value of  $k_{ip}(50 \text{ vol}\%) = 503 \text{ Wm}^{-1}\text{K}^{-1}$ . Thus, heat transport is enhanced by reinforcing Cu with graphite microplatelets at high volume fractions. Alignment is obviously a major factor for the thermal conductivity enhancement (TCE). To confirm this assumption and investigate the importance and influence of additional factors such as geometry, interface resistance, etc., on the TCE the measured data are compared to EMA calculations following Nan *et al.* [11], as described in Section 2.2.

Besides the geometry, i.e., shape, lateral size, thickness, and the intrinsic thermal conductivities of the matrix and the platelets, the orientation of the platelets is used to

calculate the thermal conductivity of the composites in in-plane and through-plane direction according to Equations 2.14 and 2.15, with  $k_{11}=k_{22}=k_{ip}$  and  $k_{33}=k_{tp}$ . The orientation parameter  $\langle \cos^2\theta \rangle$  (see Equation 2.17) was calculated using the distribution of the orientation angle  $\sigma_G$  obtained by polarized Raman spectroscopy (see Section 4.2) following

$$\langle \cos^2\theta \rangle = \frac{\int \rho(\theta, \sigma_G) \cos^2\theta \sin\theta d\theta}{\int \rho(\theta, \sigma_G) \sin\theta d\theta}, \text{ with } \rho(\theta, \sigma_G) = \frac{1}{\sigma_G \sqrt{2\pi}} \exp\left(-\frac{\theta^2}{2\sigma_G^2}\right). \quad (\text{Eq. 4.7})$$

The corresponding values for  $\langle \cos^2\theta \rangle$  as well as the additional parameters used for the calculations are summarized in Table 4.1. The thermal conductivity along the basal planes of the platelets was chosen to  $1500 \text{ Wm}^{-1}\text{K}^{-1}$ , lower than the ideal value of graphite, as

**Table 4.1** Parameters for the thermal conductivity calculations.

Parameter	M5	M25	T80	G300
$\langle \cos^2\theta \rangle$	0.53	0.59	0.69	0.54 (8 vol%) 0.58 (20 vol%) 0.80 (40 & 50 vol%)
platelet thickness	20 nm	20 nm	50 nm	5 $\mu\text{m}$
platelet lateral size	5 $\mu\text{m}$	25 $\mu\text{m}$	80 $\mu\text{m}$	300 $\mu\text{m}$
platelet conductivities	1500 $\text{Wm}^{-1}\text{K}^{-1}$ (along basal planes) 15 $\text{Wm}^{-1}\text{K}^{-1}$ (perpendicular to basal planes)			
matrix conductivity	340 $\text{Wm}^{-1}\text{K}^{-1}$			
fitting parameter	Kapitza resistance $R_k$			
fitting result for $R_k$ [ $10^{-9} \text{ m}^2\text{KW}^{-1}$ ]	0.8	0.9	1.0	1.0

discussed by Lin *et al.* [12]. Accordingly, the thermal conductivity perpendicular to the planes was taken as  $15 \text{ Wm}^{-1}\text{K}^{-1}$ . For the Cu/Gr composite system there is only one parameter that remained unknown, i.e., thermal interface resistance or Kapitza resistance  $R_k$  between copper and graphite. The Kapitza resistance will be used as the fitting parameter in Equations 2.14 and 2.15 to match the experimental data with the EMA calculations. The results of these calculations are shown in Figure 4.14 for each composite material. It turns out that this model is very capable to predict the thermal conductivity in



copper-graphite composite systems, even for high filler concentrations, since the difference in thermal conductivity between matrix and filler is not too large ( $k_p/k_m \ll 100$ ) [17]. Moreover, the orientation parameters obtained independently by polarized Raman spectroscopy lead to excellent agreement between theoretical and experimental thermal conductivity for the different platelet reinforcements.

The Kapitza resistance obtained from fitting the calculations to the measurements was around  $R_k = 10^{-9} \text{ m}^2\text{KW}^{-1}$  for all four composites (see Table 4.1). There were only a few studies investigating the Kapitza resistance of the Cu/Gr interface. Jagannadham obtained  $R_k = 0.7 \times 10^{-9} \text{ m}^2\text{KW}^{-1}$  from acoustic and diffuse mismatch models [13] and  $R_k = 0.3 \times 10^{-9} \text{ m}^2\text{KW}^{-1}$  from studying in the thermal conductivity of copper/graphene composites [14]. Wejrzanowski *et al.* calculated the thermal interface resistance between copper and multilayer graphene to  $2.5 \times 10^{-9} \text{ m}^2\text{KW}^{-1}$  using Molecular Dynamics calculations [15]. These findings compare well to the Kapitza resistance obtained in this study. The combination of copper and graphite may result in composites with excellent heat transport capability. Especially when comparing the thermal resistance to other metal/graphite interfaces. Schmidt *et al.* [16] measured the thermal interface resistance between graphite and aluminum, gold, chromium, and titanium, and found values that are one order of magnitude higher compared to the Cu/Gr interface.

It is worth to mention that the calculations in Figure 4.14d were carried out for  $\langle \cos^2\theta \rangle$  of 40 and 50 vol% graphite concentration (black stars). In the case of 8 and 20 vol%, the predictions do not match the data points (gray stars). In Figure 4.15 the adjusted curves for the in-plane and through-plane thermal conductivity are presented using  $\langle \cos^2\theta \rangle = 0.54$  and  $\langle \cos^2\theta \rangle = 0.58$ , respectively (see Table 4.1). Once again, the EMA calculations excellently match the experimental data. The comparison between these curves to the plot in Figure 4.14d highlights the huge impact of the platelet alignment on the in-plane thermal conductivity. The anisotropy of the thermal conductivity increases strongly with increasing platelet orientation. Moreover, the investigations showed that these EMA calculations may be used to reliably predict the thermal conductivity of unknown metal/graphite composites. In addition, important characteristics of a composite were extracted, e.g., Kapitza resistance, orientation of the fillers, or intrinsic thermal conductivity of the components [17].

In the following, the EMA calculations will be used to further analyze the origin of the high thermal conductivity enhancement for the in-plane direction in the Cu/G300 composites as well potential for similar composite systems. As mentioned before, the orientation of the graphite platelets has a huge influence on the thermal transport properties, due to the intrinsic anisotropy of the thermal conductivity in graphite (factor 100). This becomes even more apparent when comparing the EMA calculations for the Cu/G300 composite with different platelet orientations, as presented in Figure 4.16a. The other parameters remained constant, i.e., Kapitza resistance, platelet dimensions, thermal conductivity of the composite components, and can be found in

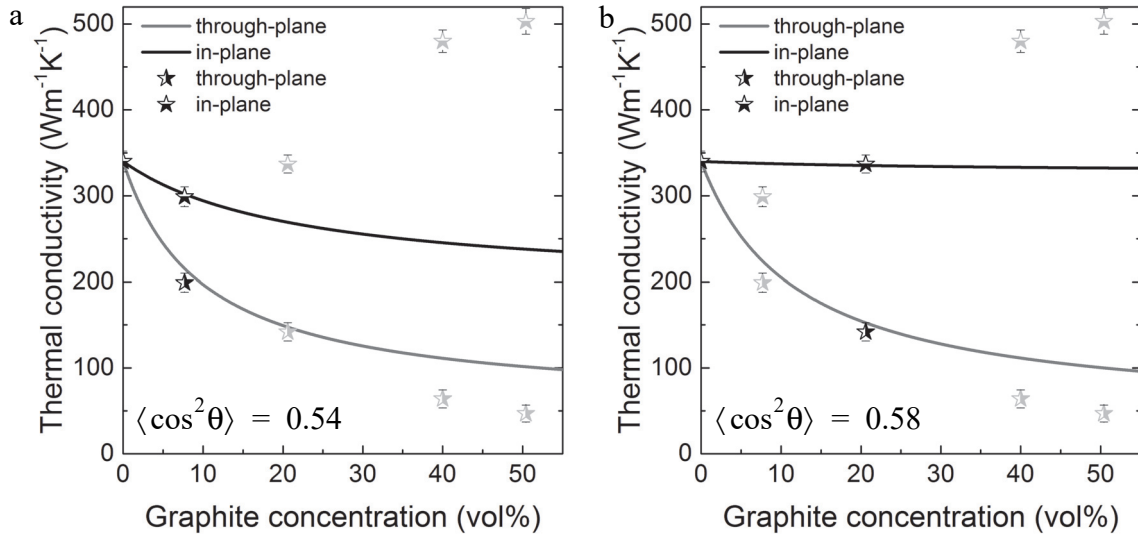


**Figure 4.15** In-plane and through-plane thermal conductivity of Cu/G300 composites calculated using the orientation parameter of the (a) 8 vol%, and (b) the 20 vol% composite (solid lines). The corresponding data have black symbols, the remaining data are shaded gray.

Table 4.1. For full alignment ( $\langle \cos^2 \theta \rangle = 1$ )  $k_{ip}$  strongly increased compared to the alignment present in Cu/G300 composites with high graphite concentration ( $\langle \cos^2 \theta \rangle = 0.8$ ). For a platelet concentration of 50 vol% the fully aligned composite is expected to have a thermal conductivity of around  $900 \text{ Wm}^{-1}\text{K}^{-1}$ , which is 2.5 times higher than the value measured for pure copper, promising outstanding heat transport capability. For a smaller degree of alignment (i.e.,  $\langle \cos^2 \theta \rangle = 0.5$ ) the in-plane thermal conductivity drops below the value of pure copper for the entire concentration range. If the platelets are randomly distributed the thermal conductivity, which is equal for the through-plane and in-plane direction, drops below the value of aluminum ( $\sim 230 \text{ Wm}^{-1}\text{K}^{-1}$ ) [8] for graphite concentrations above 30 vol%.

Another important aspect for the thermal transport is the Kapitza resistance at the Cu/Gr interface. Thus,  $k_{ip}$  was calculated for an increased Kapitza resistance by one as well as two orders of magnitude, as presented in the plot in Figure 4.16b. A ten times higher Kapitza resistance does not have a large influence on the in-plane conductivity, since it is reduced by less than 10%. Such Kapitza resistance is comparable to other metal/graphite interfaces [16]. Even with a Kapitza resistance of  $R_k = 10^{-7} \text{ m}^2\text{KW}^{-1}$  the thermal conductivity of the composite remains above the value of pure copper for all graphite concentrations. This is owed to the large lateral size of the platelets, that reduces the amount of Cu/Gr interfaces compared to smaller platelets and, thus, reduces the influence of the Kapitza resistance on the thermal transport properties. Moreover, the measured Kapitza resistance was small and not a limiting factor for the thermal conductivity enhancement, as pointed out before for copper/graphene films [14]. This is illustrated by considering the thermal conductivity of the graphite particle surrounded by an

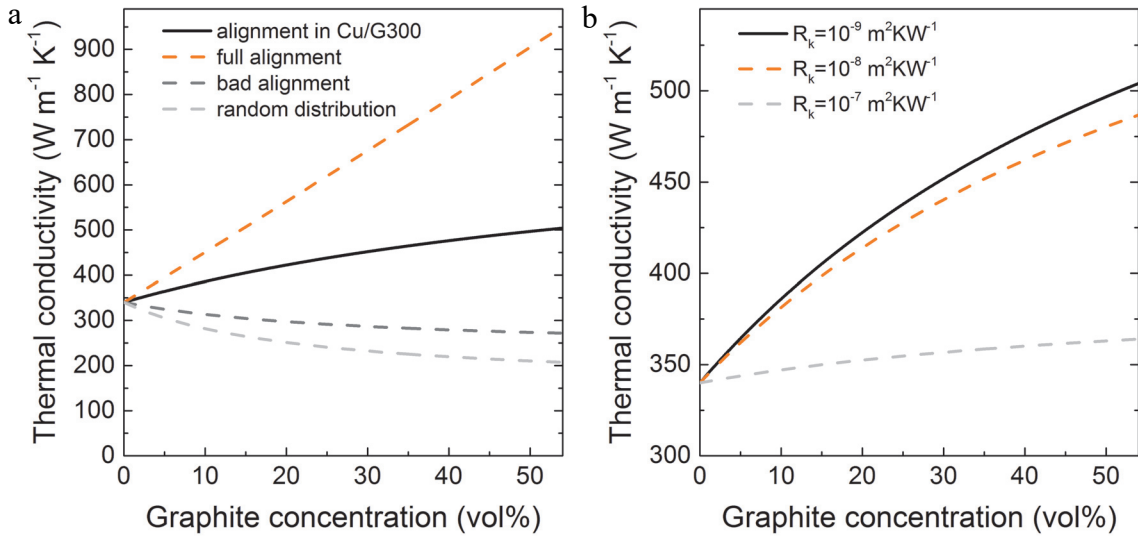


**Figure 4.16** Calculated in-plane thermal conductivity of the Cu/G300 composite (a) for different platelet orientations ( $\langle \cos^2 \theta \rangle = 0.8, 1, 0.5, 1/3$ ), and (b) for different interface resistances. The remaining parameters are listed in Table 4.1.

interface layer. The intrinsic conductivity of the platelet is  $1500 \text{ Wm}^{-1}\text{K}^{-1}$  along the basal planes and  $15 \text{ Wm}^{-1}\text{K}^{-1}$  perpendicular to the basal planes. If the particle is surrounded by a layer with thermal resistance of  $10^{-9} \text{ m}^2\text{KW}^{-1}$  the total thermal conductivity of the particle can be calculated following Equation 2.11. Compared to the intrinsic conductivity, the interface reduces the effective thermal conductivity of the particle by less than 1% to 1495 and  $14.95 \text{ Wm}^{-1}\text{K}^{-1}$ , respectively.

Another interesting question is the influence of the properties of the matrix material. Since aluminum (Al), next to copper, is a commonly used metal in thermal management devices, the EMA model is used to calculate the thermal conductivity of a Al/G300 composite, by replacing Cu with Al and leaving the other parameters unchanged, i.e., platelet orientation, geometry, and conductivity. However, the Kapitza resistance of the Al/Gr interface was determined to be  $R_k = 5 \times 10^{-8} \text{ m}^2\text{KW}^{-1}$  [16] and, therefore, has to be accounted for in the calculations. The comparison between composites with Cu and Al matrix is shown in Figure 4.17. The higher

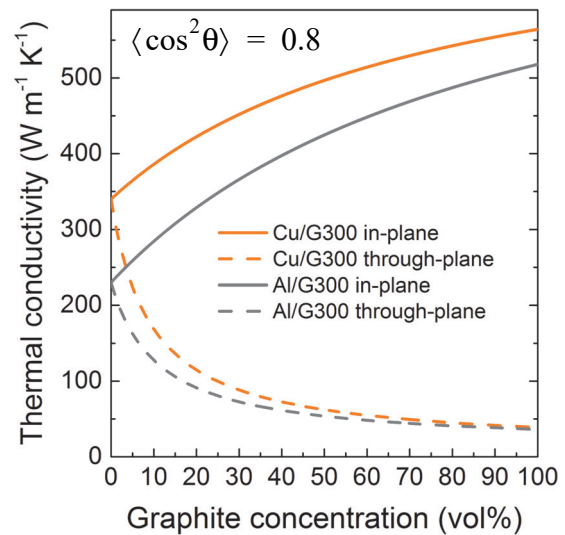


**Figure 4.17** Comparison between the theoretical thermal conductivity of G300 composites containing either Cu or Al as matrix material.

thermal conductivity and the lower Kapitza resistance of Cu lead to higher thermal conductivity of the Cu/G300 compared to the predicted Al/G300 composite, assuming similar platelet alignment. For a graphite concentration below 25 vol% the in-plane thermal conductivity of the Al/G300 composite lies below the value of Cu. These considerations indicate that Cu matrix composites promise to outperform Al matrix composites in terms of heat transport. Another advantage of Cu over Al is the lower thermal expansion, which is an important property for thermal management materials.

The highly anisotropic thermal transport in the Cu/Gr composites is optimal for applications where unidirectional heat transport is required. One important example are heat sinks for electronic devices, where heat is created locally and needs to be transported away from the source, as schematically displayed in Figure 4.18. Here the heat is generated in a silicon chip and is transported away by the highly conductive heat sink. Thus, the thermal conductivity of the heat sink material perpendicular to the direction of heat dissipation is not required to be high, as it is the case for Cu/G300 composites. Furthermore, a temperature increase causes all components to expand. Important for the heat sink in this configuration is a low thermal expansion perpendicular to the direction of heat dissipation. Particularly, the CTE of the heat sink should match the silicon expansion in this direction to reduce thermophysical stress, as indicated in Figure 4.18. In contrast, a CTE mismatch parallel to the direction of heat dissipation is not causing thermophysical stress. Therefore, an optimized heat sink material requires that the direction of high thermal conductivity and matching CTE are perpendicular to each other. The thermal expansion behavior of the Cu/Gr composites will be analyzed in the next section with respect to the described heat sink configuration.

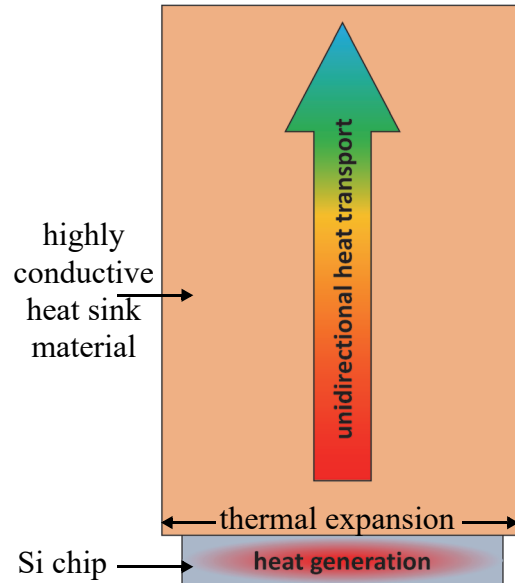


**Figure 4.18** Scheme of a common heat sink configuration, where the generated heat is transported unidirectionally by a material with high thermal conductivity

## 4.4 Thermal expansion of copper/graphite composites

The investigations of the thermal transport properties of the Cu/Gr composites in the previous sections revealed, that, as expected, the anisotropy of graphite was transferred to the composite material. Likewise, an anisotropy is expected for the thermal expansion of the composite. Considering the fact that the graphite platelets are aligned within the copper matrix, the expansion of the composite is expected to be anisotropic as well, since copper expands isotropically with a CTE of  $\alpha_{\text{Cu}} = 17.5 \text{ ppmK}^{-1}$ , but graphite expands with a negative CTE of  $\alpha_{\text{Gr,ab}} = -1.5 \text{ ppmK}^{-1}$  along the planes and a positive CTE of  $\alpha_{\text{Gr,c}} = 27.1 \text{ ppmK}^{-1}$  perpendicular to the planes. Therefore, the CTE of the composite is expected to be reduced along the alignment and increased perpendicular to this direction.

More specifically, this may be predicted theoretically using Shapery's model, introduced in Section 2.4.2. For simplicity, the calculations were carried out separately for the in-plane as well as the through-plane direction, with the assumption of perfectly aligned particles following Equation 2.43 including the elastic constants for the components listed in Table 4.2. In Figure 4.19 the calculated CTEs for the through-plane (black lines) and in-plane directions (gray lines) are presented. Additionally, the CTE was calculated following the rule of mixture (see Equation 2.42). The calculations predict that the CTE of the composite in the through-plane

direction is increasing with increasing graphite concentration and is expected to have a value of around  $22 \text{ ppmK}^{-1}$  for a graphite concentration of 50 vol%, i.e., the Cu/G300 composite with the highest in-plane thermal conductivity. Consequently, the in-plane CTE decreases with increasing graphite content towards the in-plane value of graphite with a value of around  $12 \text{ ppmK}^{-1}$  for a graphite concentration of 50 vol%. Unfortunately, this would not be beneficiary for the heat sink configuration described in the last section (compare Figure 4.18), because the thermal expansion mismatch increased at the interface between the Si chip and the heat sink.

The thermal expansion of the Cu/G300 composites as well as pure copper were measured with a horizontal dilatometer parallel and perpendicular to the platelet align-

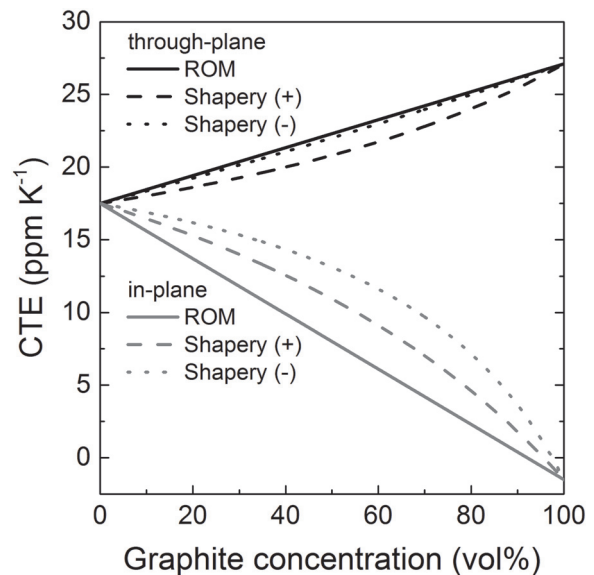


**Figure 4.19** Theoretical prediction for the coefficient of thermal expansion in Cu/Gr composite with fully aligned graphite platelets calculated for the through-plane (black lines) and the in-plane direction (gray line).

**Table 4.2** Parameters for the thermal expansion calculations with coefficient of thermal expansion, elastic modulus ( $E$ ), bulk modulus ( $B$ ), shear modulus ( $G$ ), and Poisson's ratio ( $\nu$ ).

Material	CTE [ppmK <sup>-1</sup> ]	E [GPa]	B [GPa]	G [GPa]	$\nu$	
copper	17.5 <sup>a</sup>	124 <sup>b</sup>	140 <sup>b</sup>	44 <sup>b</sup>	0.35 <sup>b</sup>	
graphite	$a$ - $b$ plane	-1.5 <sup>c</sup>	1109 <sup>d</sup>	36.4 <sup>d</sup>	485 <sup>d</sup>	0.12 <sup>d</sup>
	$c$ axis	28 <sup>c</sup>	38.7 <sup>d</sup>	5 <sup>d</sup>	5 <sup>d</sup>	0.01 <sup>d</sup>

a. measured in this study

b. Reference [18]

c. Reference [19]

d. Calculated from the stiffness constants of Reference [20] using Equations 4.8 and 4.11

ment on samples with a typical size of  $5 \times 5 \times 5$  mm. To account for the expansion of the different parts in the dilatometer, e.g., quartz piston, sample holder (see also inset in Figure 3.5), the measured displacement curves were calibrated with a correction measurement obtained by an empty dilatometer measurement. Figure 4.20a shows a typical measurement of the temperature dependence of the length change for a pure copper sample. The temperature was changed with a heating rate of  $2 \text{ Kmin}^{-1}$ , as shown by the dotted line in Figure 4.20a. In addition to the heating phase the length change was also recorded after the heating was switched off. The hysteresis at the turning point of the

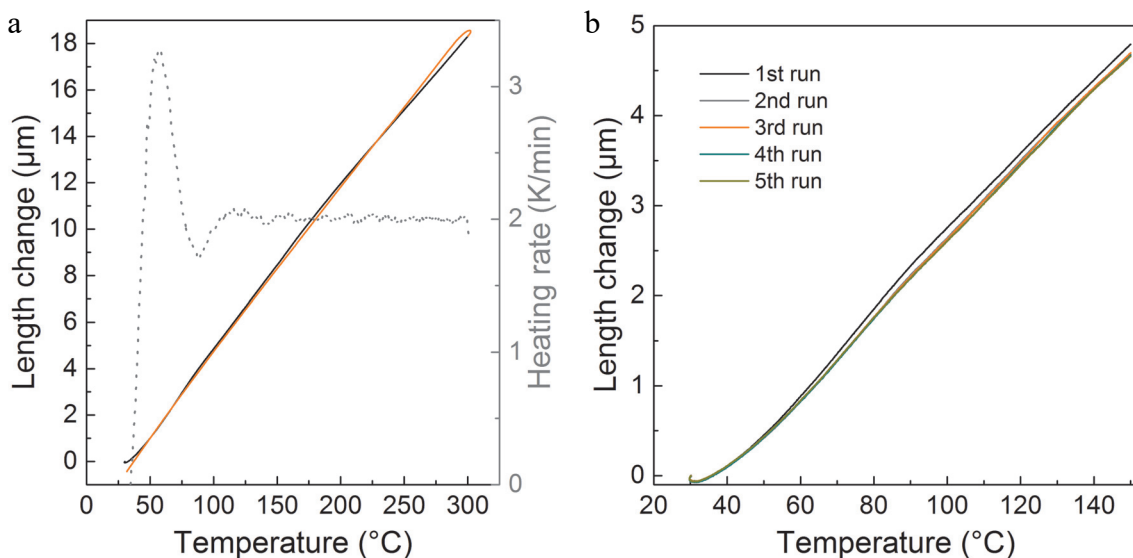


**Figure 4.20** (a) Length change in dependence of the temperature of a pure copper sample (left axis). The black/orange curve represents the heating/cooling phase. The dotted line shows the heating rate measured at the thermocouple (right axis). (b) Length change of a 50vol% Cu/G300 sample where the temperature was cycled 5 times between 30 and 150°C with a heating rate of 2 K/min.

temperature is negligible. Over the entire temperature range the length change follows the same temperature dependence for the heating and the cooling phase. However, at the lowest temperatures there is a noticeable difference between heating and cooling. This is due to the slow reaction of the furnace when the heating is started, i.e., when the heating rate changes from zero to  $2 \text{ Kmin}^{-1}$  (see dotted line in Figure 4.20a). Moreover, the temperature is measured by a thermocouple, which is close to the specimen but not in direct contact with it. That is the reason why there is a difference between the measured temperature and the actual temperature of the specimen. However, this is only influencing the measurement if the heating/cooling rate varies, because then the temperature difference changes as well. Therefore, the first data points are neglected in the evaluation of the CTE. A second important aspect for dilatometer measurements is the repeatability when the temperature is cycled multiple times. Especially for composites that consist of materials with a large CTE mismatch plastic deformations might occur that manifests in an altered length change. Figure 4.20b shows the length change for a 50 vol% Cu/G300 sample, where the temperature was cycled 5 times without removing the specimen from the sample holder. Typically, the first run differs from the following measurements for such dilatometer experiment. This is due to the fact that during the first run the quartz piston, that is pushing with a constant force on the specimen, is adjusting and improving the contact to the specimen. The subsequent runs show very similar length change trends. We conclude that the used measurement technique produces very repeatable and reliable results. Irreversible structural changes such as plastic deformation during the temperature cycling can be excluded.

As discussed before the thermal expansion was measured for pure copper as well as the Cu/G300 composites for the different graphite concentrations five times in a temperature range from 30 to  $150^\circ\text{C}$ . Temperatures beyond this range were avoided to prevent oxidation of the specimen, since the measurements are carried out under ambient conditions. The resulting displacement curves were calibrated and evaluated for a temperature range from 40 to  $150^\circ\text{C}$  for reasons discussed in the previous paragraph. The relative length change for the in-plane direction (following Equation 2.40) is presented in Figure 4.21a. With increasing graphite concentration the length change gets successively smaller. This was expected from the theoretical predictions shown in Figure 4.19. For the relative length change in the through-plane direction the 8 and 20 vol% Cu/G300 composites show very similar expansion behavior as pure copper, as presented in Figure 4.21b. Considering the high thermal expansion of graphite along the  $c$  axis an increase of the thermal expansion was expected. However, the model assumed fully aligned graphite platelets, which is not the case for the composites with low graphite concentration (see also Section 4.2).

The most surprising observation in Figure 4.21b is the dramatically lowered expansion for 40 and 50 vol% graphite concentration. The relative length change was transferred to the CTE following Equation 2.39 and plotted in Figure 4.21c and d for the in-plane ( $\alpha_{ip}$ )

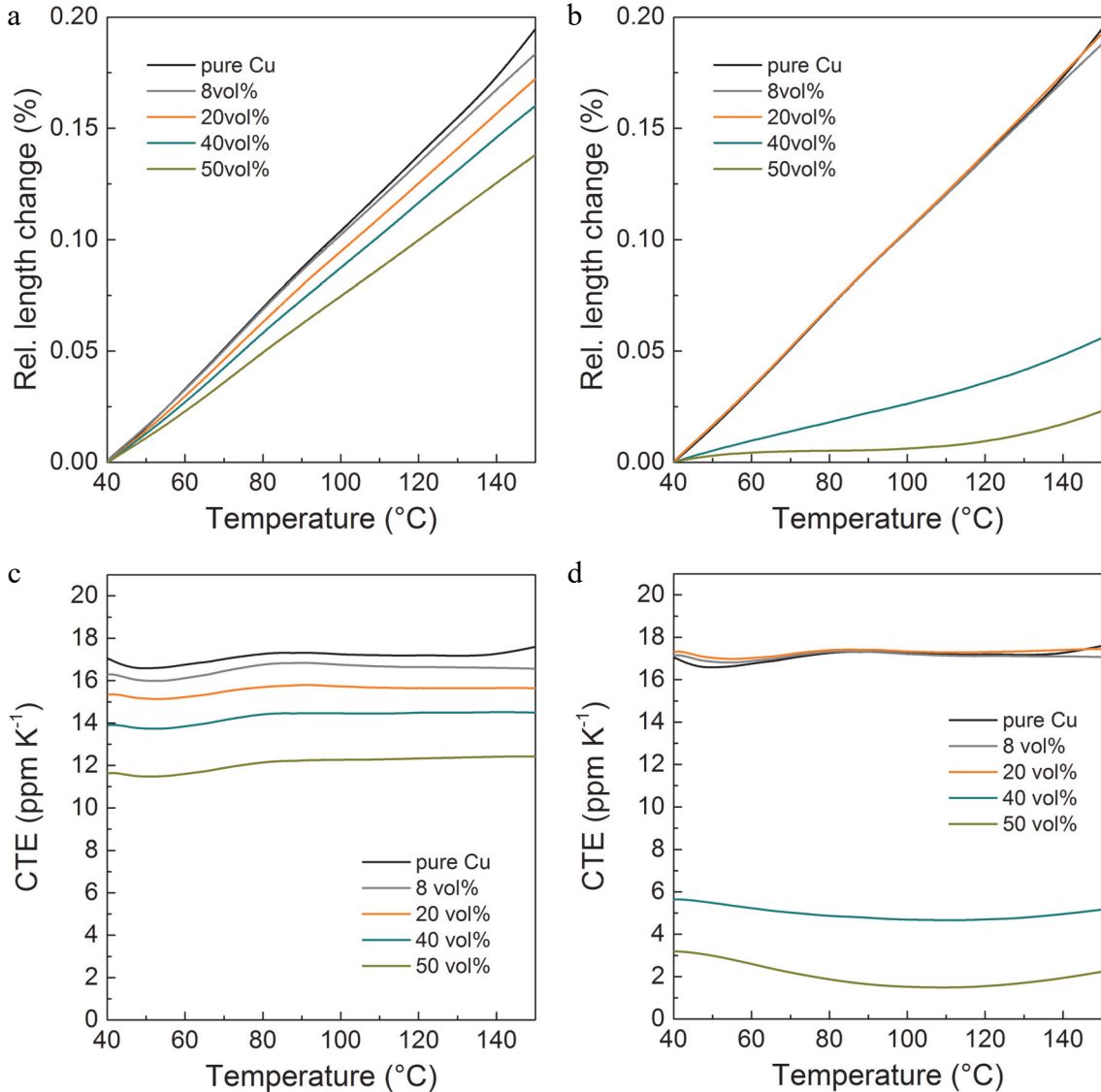


**Figure 4.21** Relative length change of pure copper and Cu/G300 composites measured in (a) in-plane and (b) through-plane direction. Coefficient of thermal expansion for the (c) in-plane and (d) through-plane direction.

and through-plane direction ( $\alpha_{tp}$ ), respectively. For the in-plane direction the CTE lies below Cu and decreased to a value around 12 ppmK<sup>-1</sup> for a graphite concentration of 50 vol%. In general, the CTE was constant over the observed temperature range showing only a small dip at low temperatures, which was due to the changing heating rate at the beginning of the measurements (compare Figure 4.20a). The magnitude of the CTE decrease compared well to the predictions made by Shapery's model (see Figure 4.19). For the 8 and 20 vol% composites the CTE in the through-plane direction was very similar to pure Cu, in line with the relative length change, as displayed in Figure 4.21d. However, it dropped dramatically to values around 5 and 2 ppmK<sup>-1</sup> for a graphite concentrations of 40 and 50 vol%, respectively. Thus, the expansion is similar to semiconductors and up to a factor nine smaller than the CTE of Cu. This is a totally counterintuitive behavior



compared to the modeled through-plane CTE shown in Figure 4.19. To exclude the influence of sample oxidation and to expand the temperature range, the thermal expansion measurements were repeated by an external institution (Netzsch, Dil 402 C) under nitrogen atmosphere from -50 to 200°C. The measurements confirmed the extremely low CTE values for the Cu/G300 composites with high platelet concentration. Oxidation of the specimen could be excluded as influence on the thermal expansion. These observations indicate that embedding graphite platelets into a copper matrix alternates the intrinsic thermal expansion behavior of the components. To explain this phenomenon further investigations are necessary and will be discussed within the framework of elasticity theory in the next section. The combination of superior thermal conductivity in the in-plane direction ( $k_{ip} = 503 \text{ Wm}^{-1}\text{K}^{-1}$ ) and low thermal expansion in the perpendicular direction ( $\alpha_{tp} = 2 \text{ ppmK}^{-1}$ ) in the Cu/G300 composite with 50 vol% graphite concentration meets all the requirements for an excellent heat sink material, as discussed in the previous section (see also Figure 4.18). Thus, this composite will be named SuCoLEx (Superior Conductivity Low Expansion) in the following.

#### 4.4.1 Elasticity theory for CTE of graphite under strain

We now derive how the presence of thermally induced stress alters the thermal expansion of the embedded graphite platelets and, thus, of SuCoLEx. Strain and stress are connected via Hooke's law, which may be written in two different forms [21]

$$\boldsymbol{\varepsilon} = \boldsymbol{S} \cdot \boldsymbol{\sigma} \quad \text{and} \quad \boldsymbol{\sigma} = \boldsymbol{C} \cdot \boldsymbol{\varepsilon} \quad \text{with} \quad \boldsymbol{C}^{-1} = \boldsymbol{S}, \quad (\text{Eq. 4.8})$$

where  $\boldsymbol{\varepsilon}$  and  $\boldsymbol{\sigma}$  are the strain and stress tensor and  $\boldsymbol{S}$  and  $\boldsymbol{C}$  are the compliance and stiffness tensor, respectively. In the so-called Voigt notation strain and stress tensors are written as six dimensional vectors

$$\boldsymbol{\varepsilon} = \begin{bmatrix} \varepsilon_{11} \\ \varepsilon_{22} \\ \varepsilon_{33} \\ \varepsilon_{44} \\ \varepsilon_{55} \\ \varepsilon_{66} \end{bmatrix} \quad \text{and} \quad \boldsymbol{\sigma} = \begin{bmatrix} \sigma_{11} \\ \sigma_{22} \\ \sigma_{33} \\ \sigma_{44} \\ \sigma_{55} \\ \sigma_{66} \end{bmatrix}. \quad (\text{Eq. 4.9})$$

Since graphite is a transversely isotropic material the stiffness and compliance tensors are expressed as [21]

$$\mathbf{C} = \begin{bmatrix} C_{11} & C_{12} & C_{13} & 0 & 0 & 0 \\ C_{12} & C_{11} & C_{13} & 0 & 0 & 0 \\ C_{13} & C_{13} & C_{33} & 0 & 0 & 0 \\ 0 & 0 & 0 & C_{44} & 0 & 0 \\ 0 & 0 & 0 & 0 & C_{44} & 0 \\ 0 & 0 & 0 & 0 & 0 & C_{66} \end{bmatrix} \quad \text{and} \quad \mathbf{S} = \begin{bmatrix} S_{11} & S_{12} & S_{13} & 0 & 0 & 0 \\ S_{12} & S_{11} & S_{13} & 0 & 0 & 0 \\ S_{13} & S_{13} & S_{33} & 0 & 0 & 0 \\ 0 & 0 & 0 & S_{44} & 0 & 0 \\ 0 & 0 & 0 & 0 & S_{44} & 0 \\ 0 & 0 & 0 & 0 & 0 & S_{66} \end{bmatrix}. \quad (\text{Eq. 4.10})$$

The engineering notation is useful to calculate the Young's and shear modulus as well as the Poisson's ratio for the corresponding directions and is given by [21]

$$\mathbf{S} = \mathbf{C}^{-1} = \begin{bmatrix} 1/E_x & -\nu_{yx}/E_x & -\nu_{zx}/E_z & 0 & 0 & 0 \\ -\nu_{xy}/E_x & 1/E_x & -\nu_{zx}/E_z & 0 & 0 & 0 \\ -\nu_{xz}/E_x & -\nu_{xz}/E_x & 1/E_z & 0 & 0 & 0 \\ 0 & 0 & 0 & 1/G_{yz} & 0 & 0 \\ 0 & 0 & 0 & 0 & 1/G_{yz} & 0 \\ 0 & 0 & 0 & 0 & 0 & 2(1-\nu_{xy})/E_x \end{bmatrix}. \quad (\text{Eq. 4.11})$$

To understand the change of the intrinsic thermal expansion of graphite when embedded in copper one has to consider the presence of internal stress. The assumption of internal stress is reasonable, since the composite is consolidated at elevated temperatures (see also Section 3.2). When cooled down to room temperature the two components shrink at different rates, which yields the thermal strain  $m$  at ambient conditions under zero external stress. Following Hooke's law (see Equation 4.8) the equation of state is then given by [22]

$$\boldsymbol{\varepsilon} = \mathbf{S} \cdot \boldsymbol{\sigma} + m. \quad (\text{Eq. 4.12})$$

With a good interface between the two components, the graphite platelets follow the thermal expansion of the composite along the in-plane direction. In SuCoLEx the difference between the intrinsic CTE of graphite and the CTE of the composite in the in-plane direction is  $\Delta\alpha_{ip} = \alpha_{ip} - \alpha_{Gr, ab} = 13.5 \text{ ppmK}^{-1}$ , which causes a strain  $\varepsilon_{11} = \varepsilon_{22}$  in the  $a$ - $b$  plane of graphite. The temperature derivative of the strain is connected to the CTE difference as

$$\frac{d\varepsilon_{11}}{dT} = \frac{d\varepsilon_{22}}{dT} = \Delta\alpha_{ip}. \quad (\text{Eq. 4.13})$$

Moreover, the biaxial stress  $\sigma_{11} = \sigma_{22} = \sigma$  is connected to the strain following Equation 4.8

$$\varepsilon_{11} = \varepsilon_{22} = (S_{11} + S_{12})\sigma, \quad (\text{Eq. 4.14})$$

where  $S_{ii}$  are the components of the compliance tensor of graphite. With elasticity theory the strain along the  $c$  axis of a hexagonal crystal is obtained [23,24]

$$\varepsilon_{33} = 2S_{13}\sigma = \frac{2S_{13}}{S_{11} + S_{12}}\varepsilon_{11} = -\frac{2C_{13}}{C_{33}}\varepsilon_{11}, \quad (\text{Eq. 4.15})$$

with  $C_{ii}$  being the components of the stiffness tensor of graphite. For the  $c$  direction Equation 4.12 may be rewritten as

$$\varepsilon_{33}(T) = -\frac{2C_{13}}{C_{33}}\varepsilon_{11}(T) + m_{33}(T), \quad (\text{Eq. 4.16})$$

by inserting Equation 4.15. Here  $m_{33}(T)$  is the thermal strain under ambient conditions along the  $c$  axis and its temperature derivative is the CTE of graphite along the same axis. The temperature derivative of Equation 4.16 yields the CTE of graphite along the  $c$  axis

$$\alpha_{33} = \frac{d\varepsilon_{33}}{dT} = \nu_{2D}\Delta\alpha_{ip} + \frac{d\nu_{2D}}{dT}\varepsilon_{11}^0 + \alpha_{Gr,c} = -27 \text{ ppmK}^{-1}, \quad (\text{Eq. 4.17})$$

with

$$\nu_{2D} = -\frac{2C_{13}}{C_{33}} = -0.83 \quad (\text{Eq. 4.18})$$

and

$$\frac{d\nu_{2D}}{dT} = -2\frac{\frac{dC_{13}}{dT}C_{33} - C_{11}\frac{dC_{33}}{dT}}{C_{33}^2} = 4.3 \times 10^{-2} \text{ K}^{-1} \quad (\text{Eq. 4.19})$$

being the two-dimensional equivalent of Poisson's ratio and its temperature derivative, respectively. The elastic constants and their temperature derivatives are  $C_{13} = 15$  GPa,  $C_{33} = 36$  GPa,  $dC_{13}/dT = -0.8$  GPaK<sup>-1</sup>, and  $dC_{33}/dT = -0.05$  GPaK<sup>-1</sup> [25]. The residual in-plane strain after SPS was estimated from the effective sintering temperature of a copper matrix (i.e., 400°C) [26] to  $\varepsilon_{11}^0 = \alpha\Delta T \approx -10^{-3}$ . This leads to a thermal expansion of graphite along the  $c$  axis of  $\alpha_{33} = -27$  ppmK<sup>-1</sup> when embedded in copper. Thus, the thermal expansion behavior of graphite along the  $c$  axis was reversed from expanding stronger than copper to shrinking stronger than graphite along the  $a$ - $b$  plane. This effect is a direct result of the strong temperature-dependence of the elastic constants in this mate-

rial and the temperature dependent in-plane strain in graphite, which is introduced during the consolidation process. In the following section, these results will be used to compare the theoretical modulation of the thermal expansion to the experimental findings for the Cu/G300 composites.

#### 4.4.2 Theoretic predictions for the thermal expansion

The findings in the last section open the possibility to modulate the thermal expansion of such composite by replacing  $\alpha_{Gr,c} = 27.1 \text{ ppmK}^{-1}$  with  $\alpha_{33} = -27 \text{ ppmK}^{-1}$ . For composites containing aligned particles one may calculate the CTE using Shapery's model for longitudinal as well as transversal expansion (see Equations 2.46 and 2.47), with the parameters summarized in Table 4.2 and the assumption of fully aligned particles. The expansion coefficients of the Cu/G300 composites are summarized in Figure 4.22. Moreover, the modulated CTE for the in-plane as well as through-plane direction are plotted together with the measured data. As can be seen, for both directions the measured CTE is in very good agreement with Shapery's model for anisotropic two-phase composites, if one uses the derived negative CTE for graphite along the  $c$  axis. This unexpected expansion behavior could not be explained with the intrinsic CTE of the components (see also Figure 4.19).

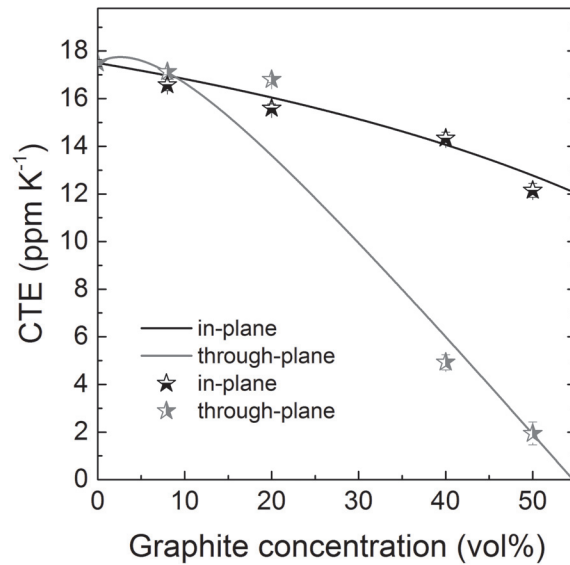


**Figure 4.22** Measured coefficient of thermal expansion (symbols) as well as modulated CTE (solid lines) for the in-plane (black) and through-plane (gray) direction of Cu/G300 composites in dependence of the platelet concentration.

## 4.5 Strain induced in silicon in different heat sink assemblies

SuCoLEx is expanding with  $12 \text{ ppmK}^{-1}$  in the in-plane and  $2 \text{ ppmK}^{-1}$  in the through-plane direction. The latter matches the thermal expansion of silicon [27]. Thus, a reduction of thermal stress induced in silicon is expected when attached to a SuCoLEx heat sink compared to metal heat sinks with higher CTE. As introduced in Section 2.5.3, the Raman spectrum of Si is sensitive to temperature changes and external stress. To investigate the reaction of Si to temperature change and thermal stress small pieces of Si (001) were glued on heat sinks made of Al, Cu and SuCoLEx. Figure 4.23 shows a scheme of the measurement setup. The silicon-heat sink assembly was repeatedly cooled down to 83 K and then heated up to room temperature, while the Raman spectra of Si were taken every 5 K.

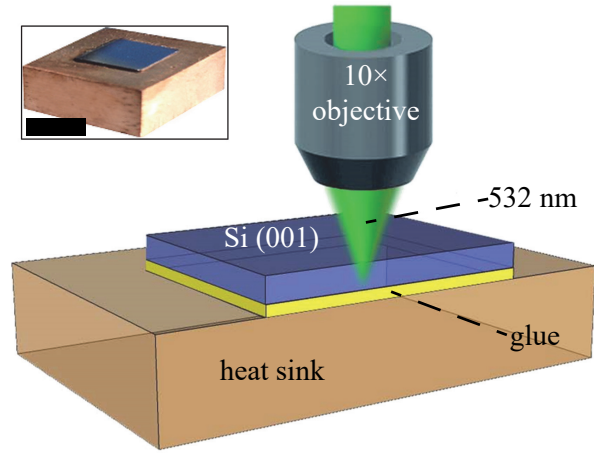


**Figure 4.23** Cross-section of the setup for the temperature dependent Raman spectroscopy of Si attached to different heat sinks. The inset shows a photograph of Si glued to Cu (scale bar 5 mm).

### 4.5.1 Free standing silicon

Obviously, free standing Si is not subjected to thermal strain and has a Raman peak around  $520 \text{ cm}^{-1}$  with a linewidth of  $4 \text{ cm}^{-1}$  corresponding to the optical phonon for zero wave vector [28,29]. Thus, comparing the peak position of free standing Si to Si attached to the different heat sinks allows to extract the peak shift caused by thermal strain, which is induced by the thermal expansion mismatch at the interface. The temperature dependent Raman spectra for Si are presented in Figure 4.24a. The peak position shifts from  $520 \text{ cm}^{-1}$  for room temperature to around  $523 \text{ cm}^{-1}$  at 80 K due to anharmonic effects [28]. Following Balkanski *et al.*, the phonon frequency as a function of the temperature were fitted to the following expression [28]

$$\omega_0(T) = \Omega + C \left[ 1 + \frac{2}{\exp(\hbar\Omega/2k_B T) - 1} \right] + D \left[ 1 + \frac{3}{\exp(\hbar\Omega/3k_B T) - 1} + \frac{3}{(\exp(\hbar\Omega/3k_B T) - 1)^2} \right], \quad (\text{Eq. 4.20})$$

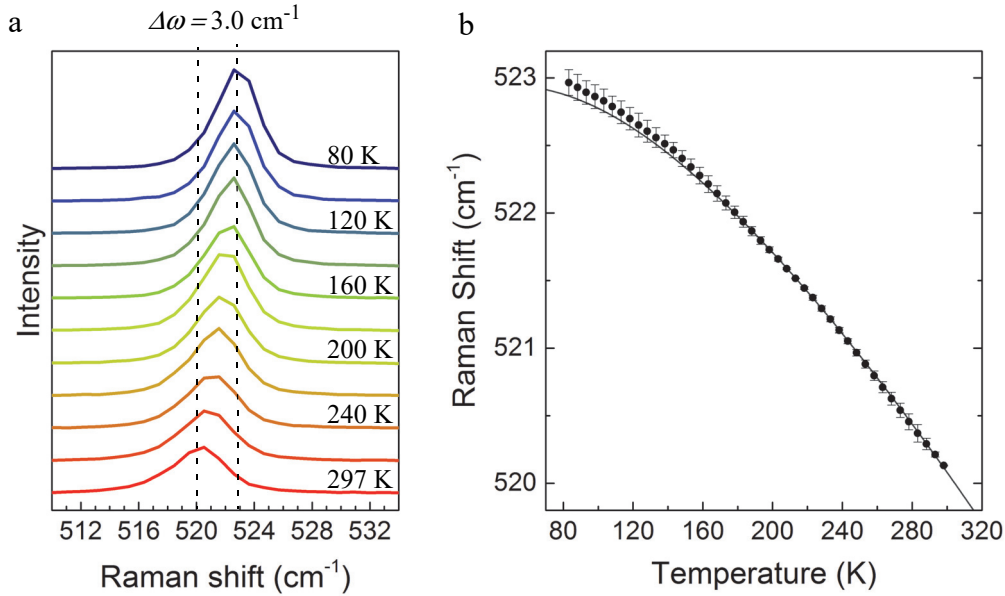


**Figure 4.24** (a) Raman spectra of Si for different temperatures and (b) average peak position of the Raman mode in dependence of the temperature (black symbols). The error bars represent the standard deviation of the single measurements. The measured data are fitted to Equation 4.20 (black line).

where  $\Omega$ ,  $C$ , and  $D$  are the fitting parameters. The peak position fitted to Equation 4.20 resulted in  $\Omega = 528.6 \text{ cm}^{-1}$ ,  $C = -3.64 \text{ cm}^{-1}$ , and  $D = -0.016 \text{ cm}^{-1}$ , as presented in Figure 4.24b.

## 4.5.2 Silicon attached to aluminum, copper, and SuCoLEx

The same Raman spectra were taken for Si attached to Al, Cu, and SuCoLEx heat sinks. The peak shifts are shown in Figure 4.25. Compared to free standing Si the shift of the phonon frequency with decreasing temperature was stronger. At 80 K the frequency difference reached values of  $2.0 \text{ cm}^{-1}$  for Al,  $1.3 \text{ cm}^{-1}$  for Cu, and  $0.6 \text{ cm}^{-1}$  for SuCoLEx. The additional shift originated from the thermal strain of the attached Cu and Al heat sink is more than 2 and 3 times higher compared to Si attached to SuCoLEx. This difference is in line with the CTE mismatch between Si and the corresponding heat sink. How the magnitude of the shift and the CTE mismatch are correlated will be derived in the next paragraph.

When Si is in contact with the different heat sinks there will be stress induced in the in-plane direction resulting in an in-plane strain. The temperature derivative of this strain is the difference in thermal expansion between Si and heat sink. Cu and Al cause biaxial strain ( $\epsilon_{11} = \epsilon_{22} = \epsilon$ ), since their expansion is isotropic. The expansion of SuCoLEx in

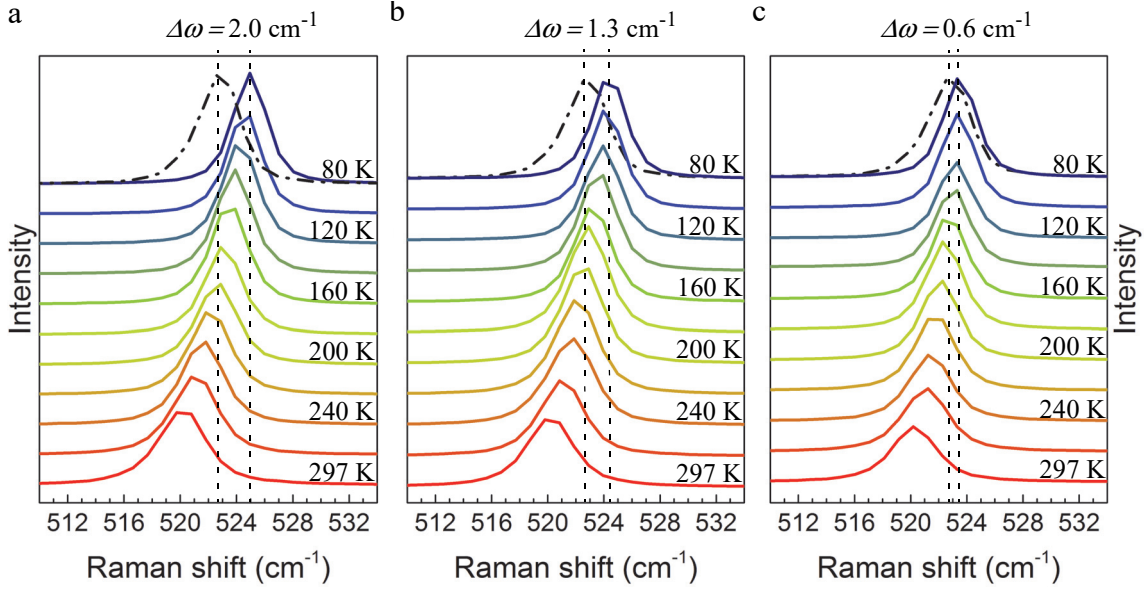


**Figure 4.25** Raman spectra of silicon attached to (a) Al, (b) Cu, and (c) SuCoLEx heat sinks for different temperatures (colored lines). The black dashed-dotted line shows the peak of free standing Si at 80 K.

through-plane direction is close to the expansion in Si. Therefore, the induced strain is uniaxial ( $\epsilon_{11} = 0$ ,  $\epsilon_{22} = \epsilon$ ), caused by the difference between the in-plane CTE of SuCoLEx and the CTE of Si. The induced strain along the  $z$  axis is given by

$$\epsilon_{33} = -\frac{C_{12}}{C_{11}}(\epsilon_{11} + \epsilon_{12}). \quad (\text{Eq. 4.21})$$

Following Equation 2.61 the frequency shift of the phonon, which is polarized along the  $z$  axis, is given by

$$\Delta\omega_3 = \frac{1}{2} \left[ \frac{p}{\omega_0^2} \epsilon_{33} + \frac{q}{\omega_0^2} (\epsilon_{11} + \epsilon_{22}) \right] \omega_0 = F \left[ \frac{q}{\omega_0^2} - \frac{C_{12} p}{C_{11} \omega_0^2} \right] \epsilon \omega_0, \quad (\text{Eq. 4.22})$$

where the factor  $F = 1/2$  for SuCoLEx and  $F = 1$  for Cu and Al, accounting for uniaxial and biaxial strain, respectively. Assuming that the elastic constants and the phonon deformation potentials are temperature independent one may write down the Raman frequency in dependence of the temperature including the shift caused by strain as

$$\frac{d\omega_3}{dT} = \left[ 1 + F \left( \frac{q}{\omega_0^2} - \frac{C_{12} p}{C_{11} \omega_0^2} \right) (\alpha_{Si} - \alpha_x) \right] \omega_0(T), \quad (\text{Eq. 4.23})$$

with  $q/\omega_0^2 = -2.31$ ,  $p/\omega_0^2 = -1.85$  [30],  $C_{11} = 165.7$  GPa, and  $C_{12} = 63.9$  GPa [31].

$\omega_0(T)$  is given by Equation 4.20 and  $\alpha_x$  is the CTE of Cu, Al or the in-plane direction of SuCoLEx.

The phonon frequency shift predicted by Equation 4.23 is  $-1.7 \times 10^{-2} \text{ cm}^{-1}\text{K}^{-1}$ ,  $-1.2 \times 10^{-2} \text{ cm}^{-1}\text{K}^{-1}$ , and  $-4.0 \times 10^{-3} \text{ cm}^{-1}\text{K}^{-1}$  for the Si/Al, the Si/Cu, and the Si/SuCoLEx interface, respectively. The experimental values are obtained by fitting the measured peak positions to Equation 4.23. Figure 4.26a summarizes the measured average peak shifts for Si attached to different heat sinks in comparison to free standing Si obtained by cycling the temperature multiple times. The repeatability of the measurement is represented by error bars. Moreover, the experimental data were fitted to Equation 4.23, which yielded a phonon frequency shift by strain of  $-1.05 \times 10^{-2} \text{ cm}^{-1}\text{K}^{-1}$ ,  $-0.87 \times 10^{-2} \text{ cm}^{-1}\text{K}^{-1}$ , and  $-0.27 \times 10^{-2} \text{ cm}^{-1}\text{K}^{-1}$  for the Si/Al, the Si/Cu, and the Si/SuCoLEx interface, respectively. These values are lower than the predictions made with the phonon deformation potentials and the elastic constants and may be attributed to the slipping at the interface due to the epoxy glue. The difference between predicted and observed frequency shift is highest for the Al heat sink, since the thermal strain is higher than for the Cu and the SuCoLEx interface.

From the measured phonon frequency shift the average thermal stress was calculated following Equations 2.62 and 2.64 to  $d\sigma/dT = 2.3$ , 1.9, and 1.1  $\text{MPaK}^{-1}$  for the Al, Cu, and SuCoLEx interface, respectively. Typically Si dies break, if the stress exceeds 200 - 400 MPa (depending on the processing conditions) [32]. For an operating tempera-

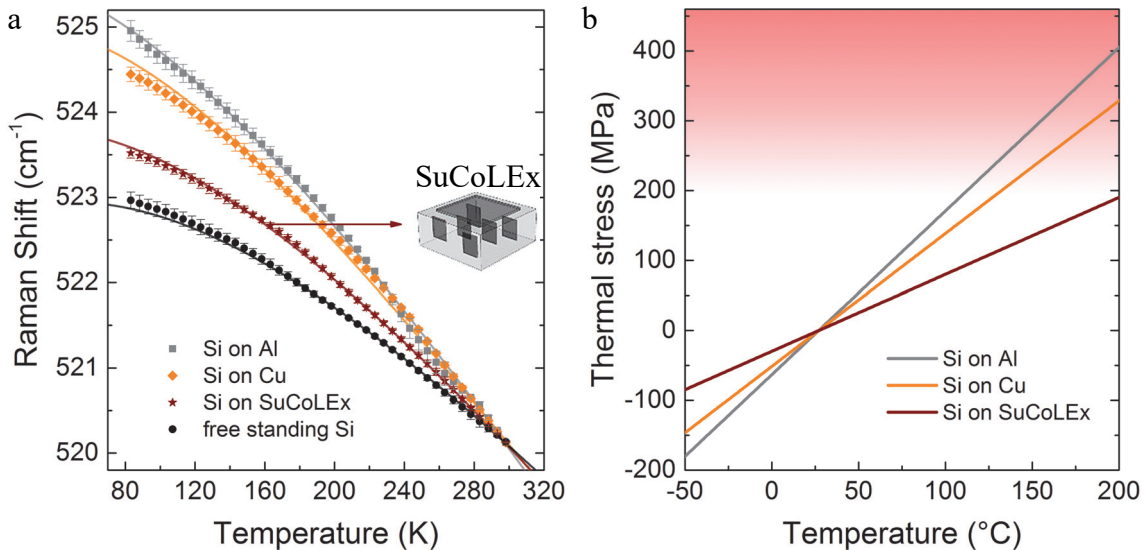


**Figure 4.26 (a)** Average frequency shift of the Si Raman peak in dependence of the temperature for free standing Si, Si attached to Al, Si attached to Cu, and Si attached to SuCoLEx (symbols). The error bars correspond to the standard deviation of the measurements. The data are fitted to Equation 4.23 (solid lines). The scheme shows how Si is attached to SuCoLEx with respect to the platelet alignment. **(b)** Thermal stress calculated from the Raman shift for Si attached to Al, Cu and SuCoLEx. The red area marks the region where the thermal stress exceeds the fracture strength of Si.



ture range of  $-50$  to  $200^{\circ}\text{C}$  the resulting thermal stress is shown in Figure 4.26b. Within this range the thermal stress induced by the SuCoLEx heat sink does not exceed  $200\text{ MPa}$  and stays below the fracture strength of Si dies. However, the thermal stress induced by Al and Cu reaches critical values when the temperature increases above  $100^{\circ}\text{C}$ . Thus, the larger expansion mismatch could lead to failures in such Si/metal assemblies. These findings underline the advantage of the low expansion in SuCoLEx.

## 4.6 SuCoLEx as heat sink for high power LEDs

The final test for SuCoLEx is the operation as a heat sink in a every day application in comparison to a copper heat sink. One area where the importance of thermal management increased over the past years is the lighting industry. As the luminous efficacy of light emitting diodes (LED) is vastly increasing, conventional incandescent light bulbs are replaced by LEDs in many areas, e.g. displays, households, and cars [33]. Still the operation of LEDs generates a large amount of heat. In contrast to incandescent light bulbs the majority of the heat is not lost by radiation (mostly infrared) but has to be removed by thermal conduction [34]. Mainly because the LED operating temperature ( $\sim 100^{\circ}\text{C}$ ) is much lower than the temperature of the filament in a light bulb. Implementing conduction-based heat transfer is one of the key challenges in the design of LED based lighting systems [34]. Clearly, advanced heat conducting materials are an important aspect in this context.

To compare the cooling performance of SuCoLEx to a conventional heat sink made of Cu two high-power LEDs were attached to equally sized heat sinks ( $5\times 5\times 20\text{ mm}$ ) made of SuCoLEx and Cu, as show in Figure 4.27a. The LED-heat sink assemblies were attached to an aluminum block. Since the thermal conductivity of SuCoLEx is around

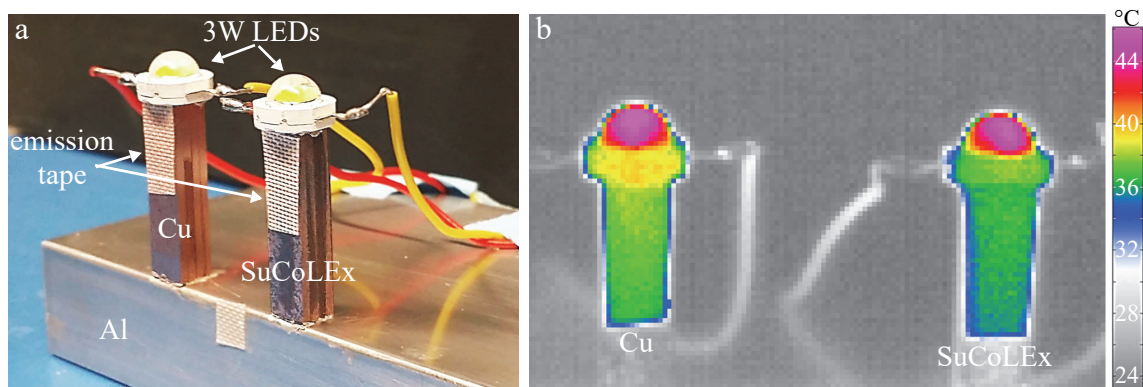


**Figure 4.27** (a) Photograph of the LED heat sink setup. The LEDs are attached to a Cu and a SuCoLEx heat sink. Emission tape (emission factor 0.95) is attached to the heat sinks to so all components have the same emission factor. (b) Thermographic image of the LED-heat sink assemblies under operation (5 min after LEDs were switched on).

50% higher than in Cu the SuCoLEx heat sink is expected to outperform the Cu heat sink. The temperature development of the two LEDs was observed with an infrared camera. Figure 4.27b shows a thermographic image of the temperature distribution on the LEDs and the heat sinks. The SuCoLEx heat sink reduces the temperature of the LED more efficiently. In particular, the temperature of the LED base plate is significantly reduced thanks to the higher thermal conductivity of SuCoLEx. The overall temperature on the surfaces of the heat sinks is lower for SuCoLEx compared to Cu underlining the superior ability to transfer heat. Reducing the operating temperature of LEDs is of significant importance. Studies showed that too high temperatures reduce the light output and the lifetime of LEDs significantly [35-38]. SuCoLEx can help increasing the light output and the lifetime of LEDs and gives more freedom to the design of the conduction-based cooling of the LED packaging.

## References

- [1] Boden A, Boerner B, Kusch P, Firkowska I, Reich S. Nanoplatelet Size to Control the Alignment and Thermal Conductivity in Copper–Graphite Composites. *Nano Letters* 2014, **14**(6): 3640-3644.
- [2] Firkowska I, Boden A, Boerner B, Reich S. The Origin of High Thermal Conductivity and Ultralow Thermal Expansion in Copper–Graphite Composites. *Nano Letters* 2015, **15**(7): 4745-4751.
- [3] Tuinstra F, Koenig JL. Raman Spectrum of Graphite. *The Journal of Chemical Physics* 1970, **53**(3): 1126-1130.
- [4] Ferrari AC. Raman spectroscopy of graphene and graphite: Disorder, electron–phonon coupling, doping and nonadiabatic effects. *Solid State Communications* 2007, **143**(1–2): 47-57.
- [5] Pimenta MA, Dresselhaus G, Dresselhaus MS, Cancado LG, Jorio A, Saito R. Studying disorder in graphite-based systems by Raman spectroscopy. *Physical Chemistry Chemical Physics* 2007, **9**(11): 1276-1290.
- [6] Ganesh VV, Chawla N. Effect of particle orientation anisotropy on the tensile behavior of metal matrix composites: experiments and microstructure-based simulation. *Materials Science and Engineering: A* 2005, **391**(1–2): 342-353.
- [7] Gorsse S, Miracle DB. Mechanical properties of Ti-6Al-4V/TiB composites with randomly oriented and aligned TiB reinforcements. *Acta Materialia* 2003, **51**(9): 2427-2442.
- [8] Ho CY, Powell RW, Liley PE. *Thermal conductivity of the elements: a comprehensive review*. Published by the American Chemical Society, for the National Bureau of Standards, 1974.
- [9] White GK, Collocott SJ. Heat Capacity of Reference Materials: Cu and W. *Journal of Physical and Chemical Reference Data* 1984, **13**(4): 1251-1257.
- [10] DeSorbo W, Tyler WW. The Specific Heat of Graphite from 13° to 300°K. *The Journal of Chemical Physics* 1953, **21**(10): 1660-1663.
- [11] Nan C-W, Birringer R, Clarke DR, Gleiter H. Effective thermal conductivity of particulate composites with interfacial thermal resistance. *Journal of Applied Physics* 1997, **81**(10).
- [12] Lin W, Zhang R, Wong CP. Modeling of Thermal Conductivity of Graphite Nanosheet Composites. *Journal of Electronic Materials* 2010, **39**(3): 268-272.
- [13] Jagannadham K. Thermal Conductivity of Copper-Graphene Composite Films Synthesized by Electrochemical Deposition with Exfoliated Graphene Platelets. *Metallurgical and Materials Transactions B* 2011, **43**(2): 316-324.
- [14] Jagannadham K. Orientation dependence of thermal conductivity in copper-graphene composites. *Journal of Applied Physics* 2011, **110**(7).
- [15] Wejrzanowski T, Grybczuk M, Wasiluk M, Kurzydowski KJ. Heat transfer through metal-graphene interfaces. *AIP Advances* 2015, **5**(7): 077142.
- [16] Schmidt AJ, Collins KC, Minnich AJ, Chen G. Thermal conductance and phonon transmissivity of metal–graphite interfaces. *Journal of Applied Physics* 2010, **107**(10).
- [17] Nan C-W, Li X-P, Birringer R. Inverse Problem for Composites with Imperfect Interface: Determination of Interfacial Thermal Resistance, Thermal Conductivity of Constituents, and Microstructural Parameters. *Journal of the American Ceramic Society* 2000, **83**(4): 848-854.
- [18] Ledbetter HM, Naimon ER. Elastic Properties of Metals and Alloys. II. Copper.

- Journal of Physical and Chemical Reference Data* 1974, **3**(4): 897-935.
- [19] Nelson JB, Riley DP. The thermal expansion of graphite from 15°C. to 800°C.: part I. Experimental. *Proc Phys Soc* 1945, **57**(6).
- [20] Bosak A, Krisch M, Mohr M, Maultzsch J, Thomsen C. Elasticity of single-crystal-line graphite: Inelastic x-ray scattering study. *Physical Review B* 2007, **75**(15): 153408.
- [21] Boresi AP, Schmidt RJ. *Advanced Mechanics of Materials*. John Wiley & Sons, 2003.
- [22] Boussaa D. On thermodynamic potentials in thermoelasticity under small strain and finite thermal perturbation assumptions. *International Journal of Solids and Structures* 2014, **51**(1): 26-34.
- [23] Blakslee OL, Proctor DG, Seldin EJ, Spence GB, Weng T. Elastic Constants of Compression-Annealed Pyrolytic Graphite. *Journal of Applied Physics* 1970, **41**(8): 3373-3382.
- [24] Hearmon RFS. *An Introduction to Applied Anisotropic Elasticity*. Oxford University Press, 1961.
- [25] Gauster WB, Fritz IJ. Pressure and temperature dependences of the elastic constants of compression-annealed pyrolytic graphite. *Journal of Applied Physics* 1974, **45**(8): 3309-3314.
- [26] Agrawal P, Conlon K, Bowman KJ, Sun CT, Cichocki Jr FR, Trumble KP. Thermal residual stresses in co-continuous composites. *Acta Materialia* 2003, **51**(4): 1143-1156.
- [27] White GK. Thermal expansion of reference materials: copper, silica and silicon. *Journal of Physics D: Applied Physics* 1973, **6**(17).
- [28] Balkanski M, Wallis RF, Haro E. Anharmonic effects in light scattering due to optical phonons in silicon. *Physical Review B* 1983, **28**(4): 1928-1934.
- [29] Hart TR, Aggarwal RL, Lax B. Temperature Dependence of Raman Scattering in Silicon. *Physical Review B* 1970, **1**(2): 638-642.
- [30] Anastassakis E, Cantarero A, Cardona M. Piezo-Raman measurements and anharmonic parameters in silicon and diamond. *Physical Review B* 1990, **41**(11): 7529-7535.
- [31] Anastassakis E, Siakavellas M. Elastic properties of textured diamond and silicon. *Journal of Applied Physics* 2001, **90**(1): 144-152.
- [32] Wu JD, Huang CY, Liao CC. Fracture strength characterization and failure analysis of silicon dies. *Microelectronics Reliability* 2003, **43**(2): 269-277.
- [33] Steele RV. The story of a new light source. *Nat Photon* 2007, **1**(1): 25-26.
- [34] James P. Thermal Challenges In LED Cooling. *Electronics Cooling Magazine*; 2006.
- [35] Christensen A, Graham S. Thermal effects in packaging high power light emitting diode arrays. *Applied Thermal Engineering* 2009, **29**(2-3): 364-371.
- [36] Narendran N, Gu Y. Life of LED-Based White Light Sources. *J Display Technol* 2005, **1**(1): 167.
- [37] Weng C-J. Advanced thermal enhancement and management of LED packages. *International Communications in Heat and Mass Transfer* 2009, **36**(3): 245-248.
- [38] Understanding Power LED Lifetime Analysis | LED Journal. <http://www.ledjournal.com/main/white/understanding-power-led-lifetime-analysis/>



theoretical model based on effective medium approximation. This underlined the importance of the platelet orientation on the thermal conductivity enhancement. In addition, the thermal interface resistance between copper and graphite could be derived from the EMA calculation and was found to be around  $10^{-9} \text{ m}^2\text{KW}^{-1}$ . The excellent applicability of the EMA was used to predict the additional potential of copper/graphite composites and similar systems (e.g., MMCs with different metal matrix).

The thermal expansion investigation revealed a surprising behavior of SuCoLEx. As expected, the CTE of the composite parallel to the direction of alignment was decreased to a value of  $12 \text{ ppmK}^{-1}$ , very much in line with the predictions from theoretical models. The negative expansion of graphite along the basal planes was transferred to the composite material. Since the CTE of graphite along the  $c$  axis is higher than the value for copper the composite was expected to have an increased CTE perpendicular to the platelet alignment. Remarkably, measurements showed that the CTE in that direction was significantly decreased to  $2 \text{ ppmK}^{-1}$  for 50 vol% graphite concentration. It could be shown that residual as well as thermal strain reversed the intrinsic thermal expansion behavior of graphite along the  $c$  axis to a negative CTE when embedded in a copper matrix. These results showed that by engineering strain in such composite system the thermal expansion can be tailored.

The major aim of this work was to develop a new generation heat sink material with improved thermal transport properties and a tailored thermal expansion to minimize thermal stress in the device. The thermal stress reduction of SuCoLEx was demonstrated by attaching the composite material to a Si wafer. The induced thermal stress was measured by temperature-dependent Raman spectroscopy and compared to the thermal stress induced by conventional heat sink materials, i.e., copper and aluminum. The thermal stress was strongly reduced by using SuCoLEx as the heat sink material. Within the typical operating temperature range of electronic devices the thermal stress induced by SuCoLEx remains below the fracture strength of silicon (i.e., 200 MPa). For the same temperature range heat sinks made of copper and aluminum induced stress as high as 400 MPa. The improved cooling capability of a SuCoLEx heat sink was convincingly demonstrated on high power LEDs. Compared to an identically constructed copper heat sink the operating temperature of the LED was reduced, which is crucial for extending its lifetime.

SuCoLEx fills a gap for thermal management materials. As can be seen from the Ashby plot in Figure 5.1, conventional heat sink materials usually combine high thermal conductivity with high thermal expansion. There are very few materials with low CTE and decent thermal transport capability. This correlation is disrupted in SuCoLEx. Highly conductive semiconductors, such as diamond and boron nitride, are the materials that can compete with the heat sink performance of SuCoLEx. These materials, however, are very expensive and difficult to process and manufacture in bulk quantities. The starting materials of SuCoLEx, on the other hand, are commercially available in huge quantities and are

comparably inexpensive. In addition, the fabrication process is well established and can be conducted at an industrial scale.

Another key advantage of SuCoLEx over traditional thermal management materials is its low density - a desirable feature in weight-critical applications. Along with the high thermal conductivity, the SuCoLEx material possesses high specific thermal conductivity, which is defined as the ratio between thermal conductivity and density. In fact, compared to copper, the specific thermal conductivity of SuCoLEx is more than two times higher. With the value of  $930 \text{ Wcm}^{-2}\text{K}^{-1}\text{kg}^{-1}$ , SuCoLEx exceeds even aluminum ( $850 \text{ Wcm}^{-2}\text{K}^{-1}\text{kg}^{-1}$ ), which is the major heat sink material of choice for lightweight devices.

The results presented in this thesis demonstrate the advantage of using anisotropic fillers, like graphite, to create superior materials for thermal management with strongly reduced weight and enhanced cost effectiveness. We believe that the knowledge gained from our SuCoLEx composite material may significantly change the design of thermal packaging. With the silicon-like expansion, which keeps the strain below the fracture strength of the semiconductor chip, one could directly attach the SuCoLEx heat sink to the CPU without the risk of malfunctions or defects. This eliminates the biggest weak spot in a thermal management package, i.e., the number of interfaces between the single components, which as a consequence would reduce the thermal resistance of the cooling system.

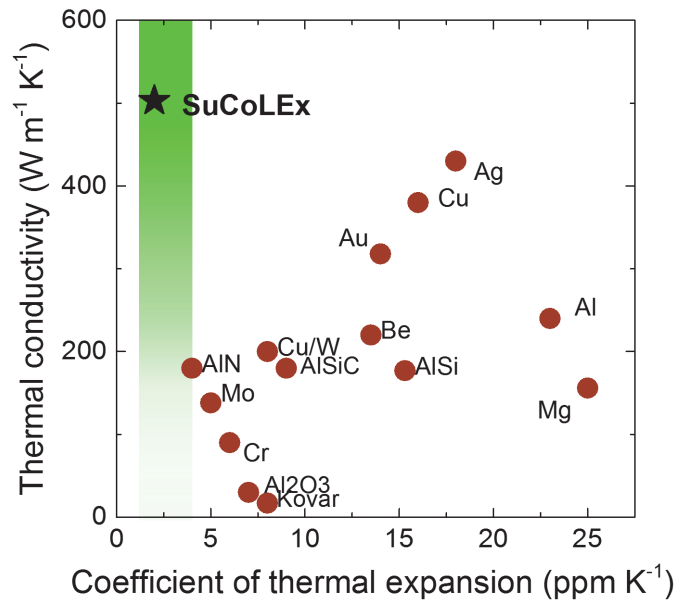


**Figure 5.1** Ashby plot of key thermal management materials. The desired region for heat sink materials used for cooling of semiconductor devices is marked in green (the darker the better).





## *List of Publications*

---

Datsyuk V, Firkowska I, Gharagozloo-Hubmann K, Lisunova M, Vogt A, Boden A, Kasimir M, Trotsenko S, Czempiel G, Reich S. Carbon nanotubes based engineering materials for thermal management applications. 2011 27th Annual IEEE Semiconductor Thermal Measurement and Management Symposium (SEMI-THERM) 2011: 325-332.

Firkowska I, Boden A, Vogt A-M, Reich S. Tailoring the contact thermal resistance at metal-carbon nanotube interface. *physica status solidi (b)* 2011, **248**(11): 2520-2523.

Firkowska I, Boden A, Vogt A-M, Reich S. Effect of carbon nanotube surface modification on thermal properties of copper–CNT composites. *Journal of Materials Chemistry* 2011, **21**(43).

Gharagozloo-Hubmann K, Boden A, Czempiel GJF, Firkowska I, Reich S. Filler geometry and interface resistance of carbon nanofibres: Key parameters in thermally conductive polymer composites. *Applied Physics Letters* 2013, **102**(21).

Boden A, Boerner B, Kusch P, Firkowska I, Reich S. Nanoplatelet Size to Control the Alignment and Thermal Conductivity in Copper–Graphite Composites. *Nano Letters* 2014, **14**(6): 3640-3644.

Firkowska I, Boden A, Boerner B, Reich S. The Origin of High Thermal Conductivity and Ultralow Thermal Expansion in Copper–Graphite Composites. *Nano Letters* 2015, **15**(7): 4745-4751.



## *Acknowledgments*

---

It was quite a long journey for me at Freie Universität Berlin during which I met many interesting and inspiring people. Quite a few of them helped, supported or assisted me during my studies, my work as a diploma student, and especially during the time I worked on this thesis. Before this journey comes to an end I would like to thank these people.

First and foremost my supervisor, Stephanie Reich, for letting me join her group almost six years ago despite me being a scientific rookie. Not only did she introduce me to the field of material science, to carbon materials, and everything that goes along with that, but she also let me broaden my (not only scientific) horizon by allowing me to travel around the world. In deepest gratitude I will always remember the outstanding time I had in your group.

Izabela Firkowska-Boden for changing my life the day I met you as the head of the Metal Composite Group (MC Group). Soon you became much more than that. Thanks for everything you taught me, for motivating and pushing me when it was necessary, for all your ideas, for lifting me up when I was down...

...You are the love of my life and made me what I am today more than anybody else!

The members of the “MC Group”, especially Benji Börner for all the work in the lab way beyond what he was obligated to, Katharina Goltsche for her work in the chemistry lab, and all the former bachelor students and interns for their contributions to our research.

The members and former members of AG Reich for the good times I had working or hanging out with you, in particular Anna-Maria Vogt, Kati Gharagozloo-Hubmann, Vitaliy Datsyuk, Patryk Kusch, Benjamin Hatting, Sebastian Heeg, Heiko Dumlich,

Pascal Blümmel, Mareen Gläske, Antonio Setaro, Julio Chacon Torres, Christian Roth and Gudrun May-Nasseri.

Eric Anglaret for being my second supervisor. I really appreciate that you accepted to sacrifice some of your precious time.

Meinen Eltern, dafür dass sie mir nie vorgeschrieben haben, was ich mit meinem Leben anfangen soll. Ihr habt mir immer die Freiheit gegeben, der Schlaumeier zu werden, der ich jetzt bin. Das habt ihr nun davon!

## *Selbstständigkeitserklärung*

---

Hiermit versichere ich, dass ich die vorliegende Dissertation mit dem Titel

“Copper Graphite Composite Materials - A Novel Way to Engineer Thermal Conductivity and Expansion”

selbstständig und ausschließlich mit unter der Zuhilfenahme der angegebenen Hilfsmittel und Hilfen angefertigt habe. Ich versichere des Weiteren, dass die Arbeit in keinem früheren Promotionsverfahren angenommen oder als ungenügend beurteilt wurde.

Berlin, im September 2015

André Boden

